QATAR UNIVERSITY

COLLEGE OF ARTS AND SCIENCE

# NEW FLEXIBLE POLYVINYLIDENE FLUORIDE NANOCOMPOSITES FOR FUTURE APPLICATIONS

BY

AISHA AL-SAYGH

A Thesis Submitted to the Faculty of

College of Arts and Sciences

In Partial Fulfillment

of the Requirements

for the Degree of

Master of Science in

Materials Science and Technology

Jan 2017

COMMITITEE PAGE

The members of the committee approve the thesis of Aisha Al-Saygh defended on 28th of Dec, 2016.

_____
Mariam Al-Maadeed
Thesis/Dissertation Supervisor

_____
Talal Altahtamouni
Committee Member

_____
Yousef Hijji
Committee Member

_____
Ahmed Ayesh
Committee Member

Approved:

_____
Rashid Alkuwari, Dean, College of Arts and Sciences

ABSTRACT

In this work, we report novel flexible polyvinylidene fluoride (PVDF) hybrid pressure sensors with good mechanical properties. Hybrid combinations of reduced graphene oxide (rGO) with different nano metal oxides -titanium nanolayer (TNL), iron oxide (FeO), and zinc oxide (ZnO)- in PVDF matrix were prepared by solution casting method. In addition to the pressure sensing and vapor sensing properties, the thermal, mechanical, electrical, and dielectric characteristics of the materials are studied.

PVDF/rGO (2.5 wt.%)-TNL (2.5 wt.%) hybrid composite showed 2 and 3.6 times enhancement, respectively in tensile strength and Young's modulus compared to the neat PVDF. The dielectric constant for PVDF/rGO-TNL at 100 Hz was 3.6 times higher than neat PVDF. In pressure sensing, the additives in the matrix increased the sensitivity by 333.46% at 5 kPa and 200.7% at 10.7 kPa and 246.7% at 17.6 kPa compared to PVDF/TNL (5 wt.%). The hybrid composite also exhibited good sensing ability towards the vapors of acetone, tetrahydrofuran (THF), and dimethylformamide (DMF) respectively 1.8, 2.5 and 2 times higher than PVDF/TNL.

PVDF/rGO (2.5 wt.%)-FeO (2.5 wt.%) hybrid composite showed 1.3 and 13.8 times enhancement in tensile strength and Young's modulus respectively, compared to neat PVDF. The dielectric constant at 100 Hz was 1.87 times higher than the pure polymer. In pressure sensing, the sensitivity increased by 41% at 5 kPa, 24.8% at 10.7 kPa and 30.3% at 17.6 kPa compared to PVDF/FeO (5 wt.%). PVDF/rGO-FeO also exhibited good vapor sensing towards acetone, THF, and DMF respectively 1.2, 1.24 and 1.4 times higher than the PVDF/FeO.

For PVDF/rGO (2.5 wt.%)-ZnO (2.5 wt.%) hybrid composite, the enhancement in tensile strength and Young's modulus was 1.98 and 14 times respectively higher than the PVDF. Its dielectric constant at 100 Hz was 1.6 times higher compared to PVDF. In pressure sensing, the sensitivity increased by 167.6% at 5 kPa, 657% at 10.7 kPa and 1066.6% at 17.6 kPa compared to PVDF/ZnO (5 wt.%). PVDF/rGO-ZnO also exhibited good vapor sensing towards acetone, THF, and DMF respectively 1.76, 2.6 and 1.89 times higher than PVDF/ZnO.

It was found that PVDF/rGO-FeO possesses the best performance to detect Acetone asn PVDF/rGO-ZnO to detect THF. PVDF/rGO-ZnO and PVDF/rGO-FeO showed the same performance to detect DMF, thus suggesting the future fabrication of electronic nose or e-nose to distinguish polar and non-polar solvents with these polymer nanocomposites.

TABLE OF CONTENTS

LIST OF TABLES

LIST OF FIGURES

ACKNOWLEDGEMENT

First of all, praise is due to almighty ALLAH with His compassion and mercifulness to allow me finalizing this project. I would like to express my sincere and deepest appreciation to my supervisor Prof. Mariam Al Ali Al- Maadeed for her guidance and support over this project. Her assistance and suggestions were invaluable towards the completion of this work. I am extremely thankful to my committee members Dr. Yousef Hijji, Dr. Ahmed Ayesh and Dr. Talal Altahtamouni for providing me with the reflection of good academic background. Special Thanks to Dr. Deepalekshmi Ponnamma for her patience, she was a constant inspiration and perfect guide to me in the lab work. Many thanks for Dr. Mohammed Hassan for his support and cooperation.

I would like to thank the faculty members of Material Science and Technology program at Qatar University as well as the staff of Center for Advanced Materials for their co-operation throughout this period. I would like to thank Prof. Karim Alamgir from Akron University for giving me a chance to visit their labs and to do some analyses.

Mr. Abdulaziz Al-Rumaihi, the assistant manager, Mr. Ali Al-Awadhi, the head of quality laboratories, and Eng. Eiman Al-khalaf, at Qatar Petroleum-Refining Operations, my gratefulness to you for your support and encouragement which helped me to complete this study.

Many thanks to QNRF for providing some financial support through the research grant NPRP 6-282-2-119.

Lastly, my sincere thanks to all those who have directly or indirectly helped for the work reported herein.

# DEDICATION

I would like to dedicate this work to my family. To my parents, who have always encouraged me to pursue my goals, never admit to defeat and always motivate to succeed. From them I have learned to be the best. Thank you for being a part of my life.

# CHAPTER 1 - INTRODUCTION

Polymer nanocomposites (PNC) have drawn increased attention due to their unique properties such as electrical conductivity, chemical resistance, mechanical strength, thermal stability, and solvent resistance [1]. These properties make this class of materials a favorable choice for various applications such as electronics, industrial [1], biomedical [2], and food packaging [3]. In order to improve the properties of polymers, nanomaterials are incorporated within the polymer matrix so that new physical properties with novel behavior different from that of the original material is obtained. Based on the dimensions of the nanomaterials (nano scale $=10^{-9}$ m), they can be of three types: nanotubes, nanoparticles and nanolayers [4], [5]. Examples of these nanomaterials include metal oxides (e.g. $Fe_2O_3$, $Al_2O_3$, FeO, ZnO, etc.), carbon black, quantum dots (eg. CdS, PbS) (as nanoparticles), carbon nanotubes, halloysite nanotubes (as nanotubes), layered silicates (e. g. Montmorillonite), graphite and graphene (as nanolayers), etc.

Out of the various classes of polymers, polyvinylidene fluoride (PVDF) stands as one of the best polymers for electronics [6], [7]. It is a semi crystalline thermoplastic polymer which possesses excellent physical, piezoelectric, pyroelectric, ferroelectric and dielectric properties. Several fabrication routes were developed based on this particular polymer for devices such as piezoelectric sensors, capacitors, and pyroelectric detectors [8], [9]. The most common crystalline structures observed in PVDF are α-phase (non-polar) and β-phase (polar). The presence of β phase is responsible to make the PVDF a good piezoelectric and ferroelectric polymer that can convert the mechanical energy into electrical energy. The reason behind this effect, is that the hydrogen and fluorine atoms produce a dipole moment while compressing the polymer backbone [10]. However, β phase cannot form naturally in

PVDF and moreover the dielectric constant of PVDF is 12 and needs to be improved for selected applications. Large number of PVDF composites were developed due to their electrical, dielectric and thermal properties. This is usually done by reinforcing the insulating PVDF with conducting nanoparticles.

In this thesis we report the significance of few nanofillers and their hybrid combinations in developing PVDF nanocomposite sensors. The reduced graphene oxide (rGO of 1.5 nm thickness) and metal oxide nanoparticles (titanium nanolayers (TNL of 20-30 nm thickness)), zinc oxide (ZnO of 100 nm diameter) and iron oxide (FeO of 30 nm diameter) were used as nanofillers. The composites were fabricated by simple solution casting.

The fabrication of free standing graphene based hybrid composites with functional features and high flexibility is still a challenge [11]. Graphene is important due to its excellent electrical conductivity, specific surface area, mobility of charge carriers, and high mechanical properties. Graphene is added to PVDF matrix as a filler to enhance thermal, electrical, and mechanical properties [12]. TNL ($TiO_2$ in the form of nanolayer), is of low cost, low toxicity, and have good antibacterial property and structural stability [13], [14] which make it attractive in designing electronic devices [15], [16]. In recent reports, a variety of metal oxides can act as reliable sensing materials even at room temperature with high sensitivity and faster response [17], [18], [19].

In order to get sensing property, it is important to synthesize a conducting polymer nanocomposite (CPC) which can exhibit good electrical resistance variation [20], [21]. For this, the conducting filler concentration should be at or above percolation level. The percolation threshold is the minimum concentration of the filler that causes fast change in the electrical properties of the composite. A concentration of 2.5 wt.% was selected as the individual concentration of the metal nanoparticles as well as rGO [22], [23]. We expected

that this concentration of nanomaterials is enough to get good resistance response, and higher dielectric properties for the hybrid composites better than individual filler concentration of 5 wt.% that can show higher aggregation and less dielectric properties. This is explained by Justin and Chen et al. [24] by adding different weight of graphene oxide (GO) content to chitosan (CS) matrix and they observed that mechanical properties of the composite decreased at 5 wt.% due to aggregation of particles.

We have successfully produced rGO through improved graphene oxide synthesis and the hybrid graphene-metal oxide combinations are made by simple solvent mixing (ultrasonication). Solution mixing was adopted for the fabrication of PVDF nanocomposites. The produced material exhibited good compatibility between metal oxides and rGO which enhanced the mechanical strength, dielectric properties, and sensing responses by decreasing the aggregation of individual nanoparticles within the PVDF matrix. Thus we report various promising hybrid graphene-metal nanocomposite combinations that have not been reported before. The new tailored nanocomposites exhibited variation in relative resistance upon applied pressure. Moreover, they were found to be capable of detecting the presence of solvent vapors, and enable distinguishing the non-polar solvents from polar ones; thereby making them viable candidates for application in pressure and electronic nose (e-nose) sensors.

# CHAPTER 2 - LITERATURE REVIEW

## 2.1. Polymers and Polymer Nanocomposites

Polymers are macromolecules that contain repeating subunits known as monomers. Polymers can be natural such as protein and DNA or synthetic such as PVDF and polystyrene. Polymers are the choice among materials due to their useful properties such as corrosion resistivity, good mechanical properties, light weight, low cost, and possibility of production with many colors and easy fabrication [25], [26]. Pure polymers have relatively poor thermal, electrical and mechanical properties. To further enhance their properties and expand their applications, various nano fillers are added to polymers to obtain superior polymer nanocomposites (PNCs). These fillers can be particles, fibers, platelets or whiskers of various dimensions. Usually the size of the nano fillers vary from 1 to 100 nm [27]. The combination of the polymer matrix, filler and how they mutually interact determine the properties of the resulting nanocomposites [28]. By using this concept, the thermal conductivity [29], mechanical strength [30], electrical conductivity, impact strength [31], and flame retardancy [32] properties of polymers can be improved while maintaining their ductility and light weight. PNCs are widely used in different applications including construction, pipelines, aerospace, biology, offshore, and electronics [33], [34].

Various PNCs have been synthesized and studied to analyze the effects of filler addition. For example, carbon black/ nylon-12 nanocomposite was prepared for electronics; the electrical conductivity of the composite was five times higher than that of pure nylon [35]. Graphene oxide/Poly(vinyl alcohol) nanocomposites showed an enhancement in ductility and improvement in tensile strength compared to pure Poly(vinyl alcohol) [36]. Another example, the nanocomposite of Polythiophene and nickel (Ni) nanoparticles which was prepared using electrochemical oxidative polymerization showed good electrical conductivity response and the electrical conductivity increased as the amount of Ni nanoparticles

increased [37]. Table 2.1 shows examples of recent publications of PNCs and their applications.

Recently the researchers are focusing on manufacturing electronic gadgets based on polymeric materials to meet customer demands [38], [39]. Conducting Polymer nanocomposites (CPC) were used for sensing applications mainly as signal transducers. CPCs have been widely used to build various sensing devices due to their unique physical properties, high surface area, and small dimensions [40], [41]. Piezoelectric polymer matrix such as PVDF and its copolymers are mostly used for energy harvesting, touch sensing, and artificial skin applications [42].

Table 2. 1. Examples of recent publications of PNCs and their applications.

| Matrix/Reinforcement | Preparation method | Improved Properties | Application | Ref. |
|---|---|---|---|---|
| Polyamide 6/clay | Solution blending | Higher meting (40%) and crystallinity index (75%) than PA 6. | Selective laser sintering (SLS) 3D printing. | [43] |
| Dopamine/Ag | Simple immersion and coating | Good microorganism inhibition and antifouling potency | Antimicrobial platform | [44] |
| Polystyrene/MMT | In-situ polymerization | Superior anticorrosion and good thermal stability | Corrosion resistance coating material for aluminum | [45] |
| PDMS/titania | Sol-gel PNCs | Higher interfacial fraction | Design of materials and devices | [46] |
| Unsaturated Polyester/Organoclay | Melt intercalation method | Enhanced tensile modulus, tensile strength, elongation at break flexural strength by order of 2.4, 2.6, 2.4 and 2. | Industrial Applications | [47] |

## 2.2. Polyvinylidene Fluoride (PVDF)

### 2.2.1. PVDF Background

PVDF is a fluoropolymer and is semi-crystalline in nature (50% crystallinity). It is also known as poly(1,1-difluoroethylene). It is a thermoplastic, tough and hard material. It is prepared by polymerization process initiated by free radicals. The starting material is vinylidene fluoride monomer (VDF). Currently the price of PVDF is around 6.5$ per pound [48]. The description of general properties of PVDF is shown in Table 2.2 [48].

In 1960's, PVDF was successfully commercialized due to its excellent properties: long stability, chemical resistance, and high temperature that can be used in various applications such as plenum wire and architectural coatings. In 1969, Kawai discovered the piezoelectric properties in poled and stretched films of PVDF [49]. Then, Bergman et al. followed this discovery by finding the pyroelectricity and non-linear optical behavior [50].

Table 2. 2. Description of PVDF properties.

| **Property** | **Note** |
|---|---|
| Thermal | Has lower melting point among fluropolymers $M_p$= 150 °C |
| Mechanical | Has toughness along with resistance to creep, and fatigue. |
| Optical | It does not absorb visible light |
| Environmental | Has excellent resistance to harsh environments |

It is widely used in industries such as manufacturing wires, pipelines, tanks, and valves, because of its inert nature to chemical reactions and high mechanical strength. Furthermore, it has high dielectric constant and dielectric loss in the range for electrical applications [48]. It is used as a base resin for coating on steel, aluminum, plastics and wood.

In addition, the piezoelectric properties of PVDF has opened a lot of new applications with high significance [51]–[55].

The piezoelectricity of PVDF is related to its β phase, a type of chain conformation in PVDF. The presence of this phase can impart a strong piezoelectricity and it can be improved by different methods such as blending with nanofillers, stretching, polarizing in high electric field, etc. [56], [57]. The use of certain fillers can increase the piezoelectricity of a polymer. Jaitanong et al. [58] prepared a piezoelectric nanocomposite material of cement/PVDF/lead zirconate titanate (PZT) for actuator application. It was shown that the addition of PVDF at 5% volume enhances piezoelectric properties by increasing piezoelectric voltage coefficient ($g_{33}$) and piezoelectric charge coefficient ($d_{33}$) to 25.7x$10^{-3}$ Vm/N and 24 Pc/N respectively.

Pi et al. [59] synthesized a flexible piezoelectric nanogenerator thin film of (polyvinylidene fluoride -co-tri fluoroethylene) by spin coating. The flexible film was able to convert the mechanical force to electrical energy. The electrical output was obtained by applying a mechanical load and it was demonstrated to fabricate a high performance generator. The fabricated nanogenerator exhibited a short circuit current of 58 nA and open circuit voltage up to 7 V with the current density of 0.56 μA/$cm^2$.

Duan et al. [60] designed and fabricated a sound absorber based on flexible piezoelectric PVDF film that used in noise control field. It was found that PVDF-micro perforated panel (MPP) has a good absorption performance at low frequencies compared with rigid MPP absorber. Another study, by Huang et al. [61] prepared a novel PVDF/ Perfluorooctyltriethoxysilane (PFOES)-rGO piezoelectric film by solution mixing to be used as a modifying agent. It showed that the PVDF/PFOES-rGO composite has better properties compared to neat PVDF. The piezoelectric and dielectric constants of the composite were improved by 80.9% and 379% compared to neat PVDF. Furthermore, a highly piezoelectric porous PVDF membrane was prepared for self-charging power cell (SCPC) by Kim et al.

[62]. This membrane was fabricated using a β form PVDF with addition of ZnO particles. The results confirmed that the charge/discharge performance of the SCPC was improved compared to less porous or highly stretched PVDF membrane.

### 2.2.2. Structure of PVDF

PVDF is a translucent solid polymer with linear hydrocarbon consisting of repeating units of $CH_2$-$CF_2$ as shown in figure 2.1 (molecular weight > 10,000). All crystal phases have same crystalline structure- non-centrosymmetric and base centered orthorhombic [63]. Its polarity is associated with negative charge of fluorine and positive charge of hydrogen atoms that form a dipole along the polymer chain [63]. The vander Waals radius of fluorine is (1.35 Å) higher than that of hydrogen (1.2 Å), which can form highly polar bond with carbon (dipole moment (μ) = 6.4 x $10^{-30}$ C.m) [64]. The most common configuration for polymer chain is head to tail, but when a defect occurs, the configuration changes to tail to tail or head to head. The presence of these defects reduces the internal stress of polymer matrix [65]. These defects also can reduce the average dipole moment to 6-10% [64].

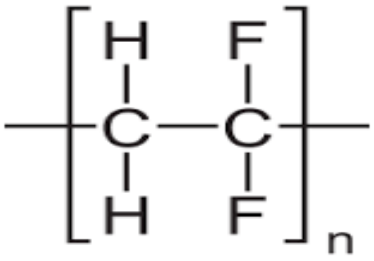


Figure 2. 1. Chemical structure of PVDF

### 2.2.3. Phase /Conformations of PVDF

The packaging and conformation of molecules control the orientation of dipoles and the dipoles are related to carbon chain orientation. Thus the conformation is related to the geometric arrangement of the chains. The conformation with a minimum potential energy during crystallization is the most desirable structure for the polymer. The organization of the bonds occurs when substituents at ± 60 gives G ± (gauche) and when substituents at ± 180 gives T ± (trans). The different phases of PVDF structure are alpha (TGTG'), beta (TTTT) and gamma (TTTGTTTG') conformations [66]. Alpha and beta are the most common phases that occur in PVDF. The most stable phase is alpha phase that has trans-gauche conformation (TGTG'), because within PVDF film the anti-parallel arrangement of chains leads the cancellation of the dipole moment [64], [67]. So this phase is not a piezoelectric phase because the alignment of the dipoles are opposite to each other in the unit cell. Beta (TTTT) conformation is the most polar one responsible for the high piezoelectric property. This is because the dipoles are oriented in the same direction and perpendicular to the molecular chain as shown in Figure 2.2 [68]. Gamma phase (TTTGTTTG') conformation has piezoelectric properties and formed from solution crystallization and can be changed to beta phase by mechanical distortion. The beta phase is desired because it enhances the piezoelectric and ferroelectric properties which makes the material better for sensing applications as well.

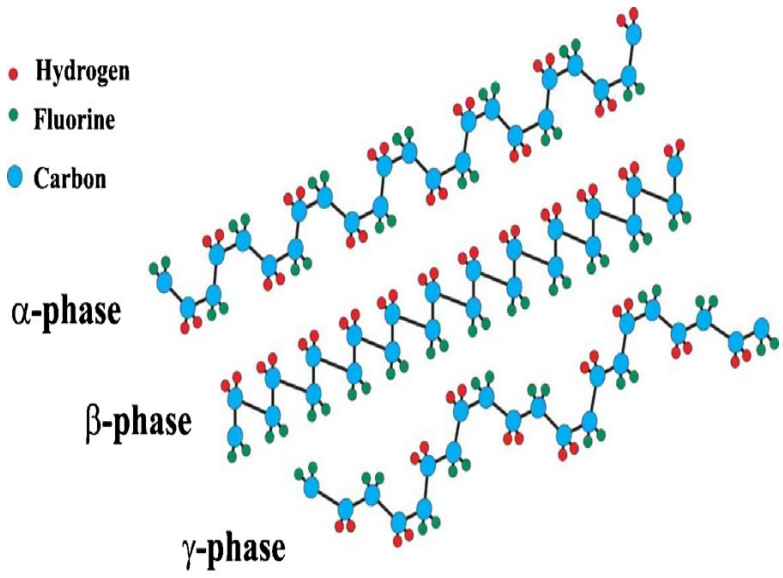


Figure 2. 2. Schematic representation of the PVDF phases: α, β and $\gamma$ phase

There are many techniques to increase the β phase in PVDF, one of them is the addition of nanofillers. This can lead to increase in the piezoelectric property. In previous works, GO was prepared as a filler for PVDF, and it was found that the addition of 0.1 wt.% to PVDF matrix results in purely β formation [69]. In another study, multiwalled carbon nanotubes (MWCNTs) were added to PVDF. It was found that the β phase content was increased which lead to the improvement in the piezoelectric property [70]. The reason behind that is the attachment of the filler to a group from PVDF (such as epoxy, hydroxyl and carbonyl), the β phase formed. An example is if the nanofiller possesses a carbonyl group, the hydrogen atom in PVDF can react with this carbonyl group. This can result in a chemical bond that causes the molecular chain of PVDF to align along the nanofiller surface and restrict fluorine atoms distributed outward. The whole process results in the transformation from α phase to β phase [67].

## 2.3. PVDF nanocomposites

### 2.3.1. Preparation/ Synthesis

The different preparation techniques of PVDF nanocomposites depend on the type of nanofillers and the required properties of nanocomposite. It can be prepared by using in-situ polymerization, solution blending, or melt intercalation method. The blending can be done in solution with an appropriate solvent or by melting above melting temperature. In order to make homogenous PNC, a good compatibility between the ingredients is mandatory. The compatibility can be improved by choosing a suitable blending condition such as chemical treatment of the polymer or the filler, mixing speed or by adjusting the temperature [71].

In in-situ polymerization method, the polymer formation occurs when nanofillers are swollen within the liquid monomer solution. This process can be initiated by the initiator, incorporation of curing agent or by increasing the temperature. The solution blending method depends on the solvent system in which polymer is soluble and nanofillers are swellable. When the polymer and nanofiller are mixed together, intercalation of polymer chain occurs which displaces the solvent within the interlayers of the nanofiller. Then the solvent is removed to produce the nanocomposite with the remaining intercalated structure. In melt intercalation method, the modified nanofiller and polymer mixture are blended under shear [71].

Solution blending is the mostly preferred and commonly used method. This type of manufacturing is prevalent because it is simple and doesn't need conventional injection or extrusion. The important notable advantage of this manufacturing technique is that its cost is less than conventional technologies. Researchers faced some difficulties in nanocomposites preparation mainly during dispersion. Dispersion can be done by several physical methods such as ball milling, ultrasonication, high speed shearing, and grinding. The dispersion of the

filler within the polymer matrix can be achieved by: complete removal of water and air bubbles, and by using mechanical and chemical forces to make de-agglomeration. The optimal performance of polymer composite can be achieved when the nanofillers are uniformly dispersed.

### 2.3.2. Nanofillers

Different fillers can be added to PVDF matrix to tailor new nanocomposite materials. Nanofillers have at least one nanometer scale dimension and can exist in tube, spherical, and platelets shapes [72]. For instance, the carbon nanotubes (CNTs) addition even in small weight percentage can enhance the mechanical strength of the polymer [73].

Layered silicates include natural and synthetic clays such as magadite, mica, bentonite, etc. It is a two dimensional nanofiller with around 1 nm thickness. The addition of clay improves mechanical properties such as strength, stiffness and barrier properties [74]–[76]. The spherical particles include metal oxides (ZnO, $TiO_2$, $CaCO_3$, $ZnFe_2O_4$) which are inorganic nanofillers [71].

In general, the purpose of dispersion of these fillers is to enhance the properties and create new functionalities of composites such as surface modification, mechanical properties, electrical conductivity, low cost, and high performance. Graphene oxide (GO), titanium nanolayer (TNL), Zinc oxide (ZnO), and iron oxide (FeO) are examples of fillers that will be explained.

GO fillers have stimulated much research interest as filler in PVDF composites due to their excellent mechanical properties, high surface area, and oxygen-containing functional groups such as carboxyl, carbonyl, epoxide and hydroxyl groups. Incorporation of GO in polymer matrix improves the characteristics of material, especially the mechanical strength

[12]. Furthermore, it has superior electrical and thermal properties. GO and rGO have a potential for modification of polymer matrices and widely used for sensor fabrication [77], [78]. Graphene can serve as a nucleating agent for generating polar β phase in PVDF. This is due to the specific interaction between $\pi$ bonds in the graphene and higher electron dense fluorine in PVDF. Moreover, the incorporation of graphene in PVDF increases the dielectric constant of neat PVDF. Usually the graphene is difficult to disperse in polymer matrix and it forms agglomeration, this is due to the strong vander Waals bonds between its individual sheets [61].

Recently $TiO_2$ emerged as another attracting polymer additive that is used for manufacturing electronic devices due to its low cost, abundance, environmentally benign nature, and stability [13]. ZnO is another inorganic filler that can be used to improve the properties of polymer system. In a previous study, ZnO was used as a filler in PVDF matrix for capacitor applications of ZnO/PVDF composites. ZnO/PVDF composite has a higher dielectric constant with 8.6 wt.% of filler addition [79]. Nano FeO also has an impact on the matrix when it is added to it. FeO/polyester nanocomposite was prepared, the results indicated that the addition of FeO filler changes the phase of the material from brittle to ductile. FeO nanoparticle composites can be used for high-density information storage, tissue- specific releasing of therapeutic agents, magnetic resonance imaging (MRI) and biomechanical applications. The inorganic filler addition plays a role in improving curing thermal stability characteristics [80].

### 2.4. Hybrid PVDF nanocomposites

Hybrid nanocomposites consist of two fillers in nanometer dimensions. Usually, one filler is organic and the other one is inorganic in nature. The combination of different reinforcements can produce new composite materials with novel properties by combining

excellent properties of these fillers [81]–[83]. Here in this project we fabricated novel hybrid composites: PVDF/rGO-TNL, PVDF/rGO-ZnO, and PVDF/rGO-FeO. It consists of PVDF polymer matrix to maintain flexibility, rGO to improve the strength and dielectric properties, and the inorganic nanoparticles enhances the dispersion of rGO within polymer matrix as well as the sensing ability.

we believe that the $TiO_2$ in the form of nanolayers will make a network together with rGO layers and will disperse well within the matrix. In order to compare the combination of various metal oxide with rGO, we have selected ZnO and FeO in the form of particles. Transition metal oxides and rGO layers have free electrons, which facilitate charge transportation and makes them good candidates for sensing applications.

**2.5. Sensing Application**

Sensing is a property that provides detection of any change in environment by a specific response. Sensors can be found in nature such as biological sensors in living organisms and artificial ones used in cars, automobiles, and biotechnology. Sensor technology is one of the widely used technologies for many applications from oil and gas to medicine. It is used to measure the pressure, temperature, quality, amount of energy, and monitor health care. Sensing mechanism depends on the relative resistance change (resistive sensing) or relative capacitance change (capacitive sensing). The resistive sensing is related to the change in electrical resistance of the composites and is practiced in the current work. The variation in the electrical resistance upon introducing the stimulus can be given by equation (2.1)[84]:

$$A_R = \frac{R - R_0}{R_0} \times 100 \qquad (2.1)$$

where ($A_R$) is the relative resistance, (R) is the final resistance and ($R_0$) the initial resistance. The capacitive sensing can be detected by the change in capacitance due to the influence of external stimulus. In this case the material need not to be conducting or to be a dielectric

material. High performance electrochemical devices such as sensors require good semiconductor properties, light weight, and enhanced energy storing capabilities. Various types of sensors have been fabricated from polymer matrices such as pressure [84], thermal/infrared [85], vapor [55], humidity [55], gas [86], [87], electrical [88], and temperature/thermal sensor [89], [90]. The most important parameters in sensor technology are response time, and sensitivity [91].

A piezoelectric material such as PVDF is important for developing pressure sensors because it can transfer the mechanical loads into electrical signals. The crystalline phase of PVDF [92] can be effectively utilized for pressure sensing applications due to the presence of β phase responsible for piezoelectric property [68]. In recent studies, Buchberger et al. prepared a PVDF sensor, which was highly flexible and used for light point localization with low cost and light weight [93]. Another work by Spanu et al. [94] prepared a high sensitivity tracile sensor based on piezoelectric PVDF. The sensor has the ability to detect pressure as low as 300 Pa with good reliability. In another study, z- directional strength measured on paper in hand sheet industries using PVDF microforce film sensor was fabricated to read the measurments, up to 10 mN [95]. Kuna et al. fabricated a PVDF sensor to measure the stress during mechanical fatigue [96]. The experiment was performed on a tensile specimen made of Al alloy and a PVDF sensor was attached with 49 electrodes. When the mechanical loading was applied, a strain and deformation to attached PVDF piezoelectric film was observed, the charges are generated on the surface and measured using the electrodes. Shin et al. prepared a hybrid composite from $TiO_2$ with rGO in PVDF matrix. It was used as a wireless pressure sensor for heart rate monitoring. The results demostrated that it can receive the signal without time delay within a distance of 8 m [97].

# CHAPTER 3 - EXPERIMENTAL WORK

## 3.1. Materials

PVDF with molecular weight ($M_W$) of 180,000 was purchased from Sigma Aldrich (USA). The chemicals used for the preparation of GO and TNL: $H_2SO_4$, $H_3PO_4$, graphite, $KMnO_4$, $H_2O_2$, NaOH, and HCl were also obtained from Sigma Aldrich. The solvents used were acetone, Dimethylformamide, ethanol and ether purchased from BDH chemicals (USA). The $TiO_2$ (anatase) nanopowder with a particle size of 15 nm was supplied by Nanostructured & Amorphous Materials, Inc (USA). Iron oxide (II, III) magnetic nanopowder, FeO of 30 nm diameter, and zinc oxide nano powder <100 nm particle size were purchased from Sigma Aldrich (USA). All chemicals were utilized without any further purification.

## 3.2. Synthesis of nanofillers and polymer nanocomposites

### 3.2.1. Preparation of nanofillers

The nanofillers, rGO and Titanium Nanolayers were synthesized in the laboratory by the following procedures:

#### 3.2.1.1. Preparation of reduced Graphene Oxide

GO was prepared from the graphite precursor following the method of improved graphene oxide synthesis [98]. In this process, we mixed $H_2SO_4$ and $H_3PO_4$ the following ratio of 9: 1 with a graphite (3.0 g, 1 wt equiv.)/$KMnO_4$ (6 wt equiv.) mixture. After that we stir the mixture for 12 h and heat it to 50 °C. 400 mL of ice was then added to reduce the temperature. 30% $H_2O_2$ (3 mL) was added after that. Filtration was arranged to remove remaining graphite. The final solid material was washed with water, followed by 30% hydrogen chloride, ethanol and ether. The prepared GO was thermally treated in oven at 50 °C for 5 h to get rGO. The dried rGO powder was analyzed for its sheet like morphology as shown by the respective SEM and TEM images in Figure 3.1a and b. The thickness of rGO

was around 1.5 nm.

### 3.2.1.2. Preparation of Titanium Nanolayers (TNL)

TNL was synthesized from $TiO_2$ precursor by hydrothermal method [99]. About 1.2 g of $TiO_2$ nanopowder was treated with 20 ml of NaOH solution in a Teflon beaker and stirred vigorously for 15 min. The mixture was then transferred to a Teflon lined autoclave and heated in a preheated oven at 130 ℃ for 10 h. The obtained precipitate was washed with deionized water. The washed precipitate was dipped in 0.1M HCl for 30 min and washed again with HCl and distilled water until the pH of the solution became neutral (pH = 7). Finally, the synthesized powder was dried in the oven and morphology was tested. The sheet like structure obtained for the nanomaterial is shown in the SEM and TEM images in Figure 3.1c and 1d respectively. The size of the TNL was around 2 nm.

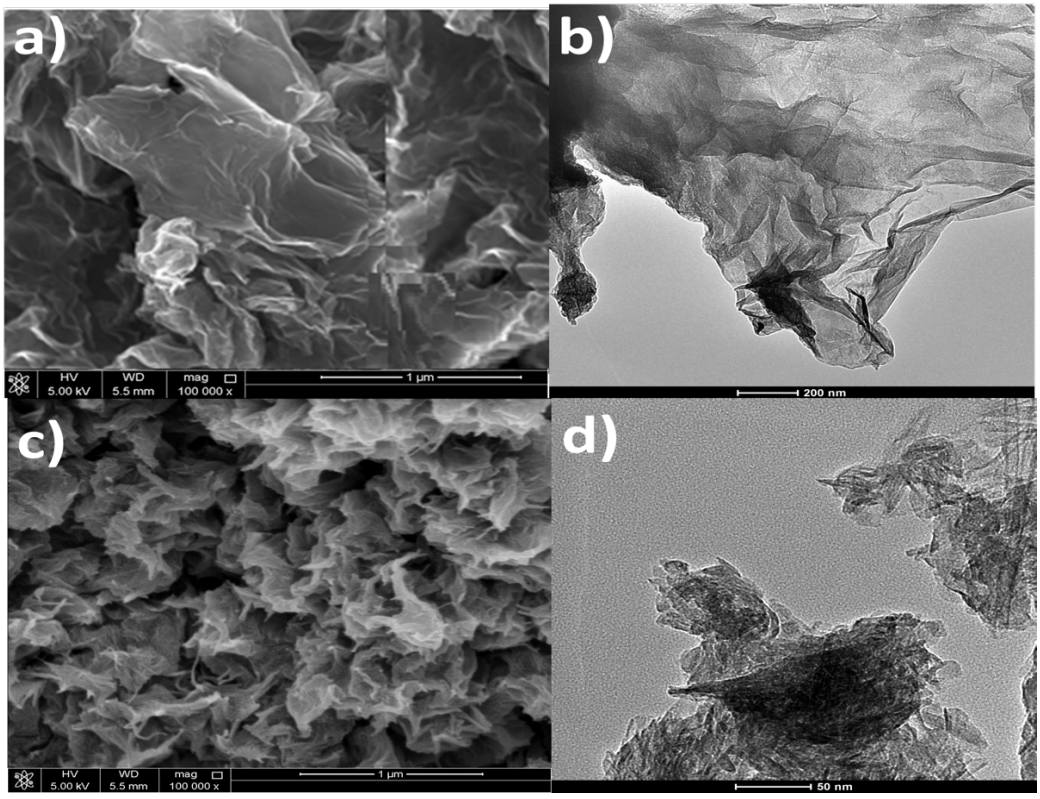


Figure 3. 1. rGO images by a) SEM, b) TEM. TNL images by c) SEM, d) TEM

### 3.2.2. Preparation of PVDF and Nanocomposites

#### 3.2.2.1. Preparation of PVDF solution

About 3 g of PVDF was dissolved in a 1:1 mixture of DMF and acetone (30 ml) to obtain 10% by weight of PVDF solution. The mixture was magnetically stirred at 70 °C for 3 h (500 rpm) to obtain a clear solution.

#### 3.2.2.2. Preparation of PVDF nanocomposites

PVDF was dissolved in a DMF/Acetone mixture to make the 10 wt.% solution. rGO, TNL, ZnO and FeO fillers in different percentages were also mixed in the DMF/acetone mixture separately by bath sonication for 2 h followed by magnetic stirring for 12 h at 500 rpm. This ensured maximum level of filler dispersion in the solvent mixture. After that the filler dispersions at 5 wt. % concentrations were mixed with the PVDF solution and the whole mixture was magnetically stirred 12 h at 500 rpm. The compositions for all PVDF composites prepared are given in Table 3.1. After the required mixing, the solutions were casted on glass plates and kept in the oven for 5 h at 70° C to make uniform composite sheets. The films were made homogeneous by hot pressing at 170°C for 4 minutes as shown in Figure 3.2.

Table 3. 1. PVDF composites with 5wt.% filler loading

| Samples | Concentration of Filler (wt. %) |
|---|---|
| PVDF | - |
| PVDF/rGO | 5 |
| PVDF/TNL | 5 |
| PVDF/ZnO | 5 |
| PVDF/FeO | 5 |

### 3.2.2.3. Preparation of hybrid nanocomposites by solvent casting

The fillers were combined together in 2.5 wt. % so that the final filler composition in the PVDF will become 5 wt.%. Composites were fabricated with the same procedure explained in section 3.2.2.2. The hybrid combinations of the prepared composites are given in Table 3.2.

Table 3. 2. Hybrid PVDF composites.

| Samples | Concentration of Filler (wt. %) |
|---|---|
| PVDF/rGO-FeO | rGO (2.5 wt.%)-FeO (2.5 wt.%) |
| PVDF/rGO-ZnO | rGO (2.5 wt.%)-ZnO (2.5 wt.%) |
| PVDF/rGO-TNL | rGO (2.5 wt.%)-TNL (2.5 wt.%) |

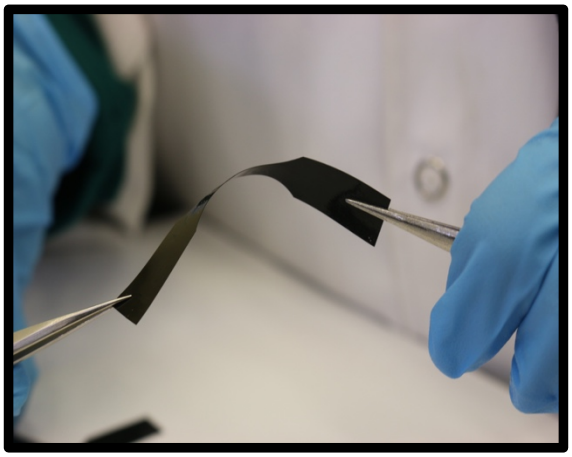

Figure 3. 2. Flexible hybrid PVDF/rGO-TNL film

### 3.3. Characterization Methods:

#### 3.3.1. Morphology and structure

##### 3.3.1.1. Scanning Electron Microscopy (SEM)

The morphology of the PVDF and its nanocomposites was analyzed using SEM. The samples were cooled by liquid nitrogen and cut after cooling. The SEM images (NOVA NANOSEM 450, FEI) shown in Figure 3.3, was used to analyze the cross-sectional area of cryocut samples. The study of mechanical fracture surface after applied tensile test was carried using SEM (JCM 6000, JEOL) shown in Figure 3.4.

SEM equipment consists of lens system, electron collector, electron gum, visual and recording cathode ray tubes. In this technique, the beam of electrons is focused on the sample. The atoms in the sample interact with electron beam and produce signals that provide details about sample composition and surface topography [100].


Figure 3. 3. Scanning Electron Microscopy.


Figure 3. 4. Scanning Electron Microscopy.

### 3.3.1.2. Transmission Electron Microscope (TEM)

The study of sample morphology was carried out using TEM (TECNAI, FEI) shown in Figure 3.5. Sample preparation was started with dissolving sample in DMF solvent. Sonication was applied for 30 min using L&R Quantrex 140 Ultrasonic Cleaning System to make the solution homogeneous. A drop of sample was placed on coated fonmvar/carbon 200 mech Cu (50) grid. TEM is a microscopy technique that is capable of imaging with high resolution around 0.2 nm.

TEM consists of different parts: electron source, electromagnetic lens system, sample holder, and imaging system. First the ultrathin specimen is introduced. The filament heats up and starts to release electrons. The electrons pass from electron beam through vacuum tubes that contain magnetic lenses. Due to opposite charges between electron (-) and lens (+), the magnetic field generated helps electrons to achieve high speed in vacuum and hits the sample specimen. So the beam of electrons that partially transmits through the ultrathin specimen

carries information about the structure of the sample. The signal passes through the projection lens to see the image of structure in output screen [101].


Figure 3. 5.Transmission Electron Microscope

### 3.3.1.3. Atomic Force Microscopy (AFM)

AFM study was carried out using MFP-3D AFM, Asylum Research. It is used to obtain information about surface roughness and surface topography. The principle is that AFM image is comprised of signals representing Z distance of cantilever motion per x, y point on the scan raster. These signals collected to form many measurement points and are typically read as voltage in the MFP-3D system.

### 3.3.1.4. Fourier Transformation Infrared Spectroscopy (FTIR)

Figure 3.6 shows PerkinElmer Spectrum 400 spectrophotometer which was used to record the Fourier transformation infrared spectra (FTIR) of the samples in the range 400-4000 $cm^{-1}$ with a resolution of 2 $cm^{-1}$.

It consists of a source of infrared energy, interferometer where spectral encoding takes place, detector to measure the interferogram signal and computer for final outputs.

The idea of this techniques is that the infrared radiation passes through the sample. The sample absorbs some of the radiation and transmits the rest. The output gives the molecular finger print of the sample. FTIR can provide different information about the sample such as the amount of components in a mixture, identify unknown materials, detect the chemical bonds, and can determine the quality or consistency of a sample.

Figure 3. 6. Fourier Transform Infrared Spectroscope (FTIR)

### 3.3.1.5. X-ray Diffraction (XRD)

X-ray test was performed using X-ray Diffractometer (Empyrean, Panalytical, UK) shown in Figure 3.7. The test for all samples was carried from the range 10° to 90°. It is a

new standard for a multipurpose diffractometer. It can be used for analysis of thin films, nanomaterials, powder and solid objects.

Figure 3. 7. X-ray Diffractometer (XRD)

### 3.3.1.6. Contact Angle Measurements

The water contact angles were checked with optical contact angle (OCA 35, dataphysics, Germany) goniometer following the sessile drop principle shown in Figure 3.8. The instrument was connected with automatic image acquisition and computation software to calculate the corresponding contact angles. The contact angles were measured at five different positions on each sample.

This technique is often used to evaluate liquid and solid surface cleanliness and surface modification. In addition, it is useful to evaluate surface macroscopic properties such as wettability [102] and surface energy [103]. When drop of pure liquid is placed on the solid

surface, two types of forces can act: adhesive forces and cohesive forces. Adhesive forces forming between the solid surface and liquid that favor spreading whereas the cohesive force within the liquid that counteract the spreading [104]. The contact angle θ is the balance between these forces and it is determined using Young's equation [105]:

$$\gamma^{SV}-\gamma^{SL} = \gamma^{LV}\cos\theta \quad (3.1)$$

Equation (3.1) describes the contact angle related to surface free energies of a system containing liquid (L), solid (S), and vapor (V) phases, where $\gamma^{LV}$ indicates liquid surface free energy or surface tension, $\gamma^{SV}$ indicates solid surface free energy, and $\gamma^{SL}$ indicates solid/liquid interfacial free energy. When the surface energy of solid surface is higher than surface energy of liquid, the drop will spread with contact angle is 0. This can occur with the addition of water drop on solid surface that has higher surface energy compared to water, surface energy of water is > 72.8 $mNm^{-1}$. When the material has high surface energy but lower than the liquid's surface tension, the liquid will wet the solid sample so that contact angle is $0° < \theta < 90°$. When the surface energy of the solid surface is lower than that of the liquid, it will result in large contact angle >90° so it is considered as hydrophobic [104].

Figure 3. 8. Optical Contact Angle

### 3.3.2. Mechanical Properties

#### 3.3.2.1. Tensile Test

The mechanical test was carried out using universal testing machine (LF PLUS, LLOYD, UK) as shown in Figure 3.9 with speed rate of 5 mm/min. The dimensions of specimen were prepared according to standard test method for tensile properties of thin plastic sheets (ASTM D882-10) [106]. Three specimen were prepared for each sample to calculate the average.

The sample was clamped using its upper and lower sides. In this test the specimen was subjected to tensile force and the resulting extension was determined using extensometer. Stress – strain curves were resulted by using equations 3.2 for strain and 3.3 for tensile stress [107].

$$\varepsilon = \frac{l - l_0}{l_0} \tag{3.2}$$

Where ε *is* the strain, $l_0$ is the initial length, and $l$ is the length after the application of force.

Tensile stress T is defined as:

$$T = \frac{F}{A_\circ} \tag{3.3}$$

Where F is tensile force and $A_0$ is cross sectional area of the unstressed specimen. The properties that are measured by tensile test are maximum elongation, ultimate tensile strength, strain hardening, Young's modulus, yield strength and Poisson's ratio. The results of this test are used to predict how a material will react under other types of forces and for quality control.


Figure 3. 9. Tensile Test Machine.

### 3.3.2.2. Dynamic Mechanical Analysis (DMA)

The dynamic mechanical behavior of the PVDF nanocomposites was studied using the dynamic mechanical analyzer (RSA-G2, TA, US) as shown in Figure 3.10. The frequency was varied from 1-100 Hz at room temperature. The samples were cut into small rectangular pieces and mounted between grips to hold.

In this technique, a small deformation (vibration) is applied to the sample with changing frequency. It measures the storage modulus, which is considered as the capability of the sample to store energy. The advantages of using DMA are: small sample size, cost competitive, and availability [108].

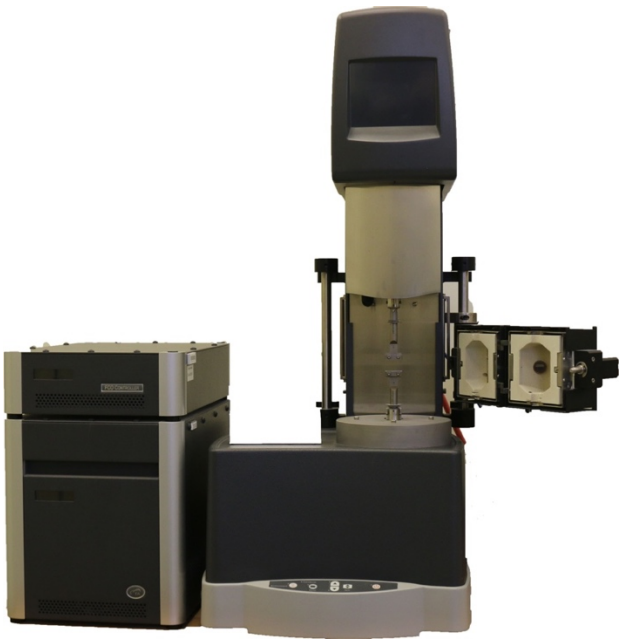

Figure 3. 10. Dynamic Mechanical Analysis (DMA)

## 3.3.3. Thermal Properties

### 3.3.3.1. Differential Scanning Calorimetry (DSC)

The differential scanning calorimetric measurements were done using Differential scanning calorimeter (DSC 8500, PerkinElmer, US) shown in Figure 3.12 in the range of 20-200 °C at a rate of 10 °C/min. The samples were hold for 5 minutes at 200 °C before commencing the cooling test. The DSC results were calculated using longitudinal method from the machine.

DSC measures the heat flow and temperature associated with transition in materials as a function of temperature and time in controlled atmosphere. The major components of DSC are furnace, temperature controller, gas control device, differential detector, signal amplifier, and data acquisition device. DSC can measure glass transition, purity, percentage crystallinity, reaction kinetics, and melting and boiling point.


Figure 3. 11. Differential Scanning Calorimeter (DSC)

### 3.3.4. Dielectric Relaxation Spectroscopy

Dielectric testing was carried out by Novocontrol GmbH Concept 40 Broadband Dielectric Spectrometer (Novocontrol Technologies, Germany) shown in Figure 3.13 at room temperature and over a broad range of frequency from 0.1 to $10^6$ Hz. 2 cm diameter sample was sandwiched between two copper electrodes of 2 cm diameter.

Dielectric spectroscopy is one of the methods that addresses electrical polarizability and molecular dynamics in polymers and nanomaterials [109]. Under applied electric field, the polarizable elements or material dipoles interact and oscillates at different frequencies ($f$) and certain temperatures. The response of the material to the applied electric field is usually expressed in terms of the complex dielectric permittivity [110] as shown in equation (3.4):

$$\varepsilon^*(\omega) = \varepsilon'(\omega) - i\varepsilon''(\omega) \quad (3.4)$$

Where $\varepsilon'$ is the real permittivity which shows the polarizability. Polarization can occur due to different factors such as deformation of delocalized electron distributions, interfacial polarization (internal or sample/electrode) or dipole reorientation. $\varepsilon''$ is loss permittivity and is related to the energy dissipated per cycle during any of the above mentioned processes. $\omega$ is the angular frequency = $2\pi f$ and $i = \sqrt{-1}$. Broadband dielectric spectroscopy is considered to be a powerful tool to understand dynamics of polymer chains as important information regarding these processes can be deduced over wide frequency (milli to mega) Hertz and temperature regions [109].


Figure 3. 12. Broadband Dielectric Spectrometer.

### 3.4. Sensing Experiments

The sensing experiments were done by measuring the electrical resistance variation of the composites using a Keithley 2400 Series Source Meter (Tektronix, USA). The measurements were performed at room temperature 25-27 °C and under 40-60% RH. Each sample was coated on the electrode (20.4 μl) in two layers. The sample layer was dried using a dryer. The electrode was connected with the equipment in a closed area as shown in Figure 3.14.

Pressure sensing experiment was done by applying different pressures (5 kPa, 10.7 kPa and 17.6 kPa) on samples at every 10 seconds under constant conditions. The current was measured at constant voltage. Vapor sensing experiment was performed for samples using different organic volatile liquids (DMF, Toluene, Benzene, THF, Acetone, and Xylene). The samples were exposed to vapor inside the flask at every 300 sec under constant conditions.

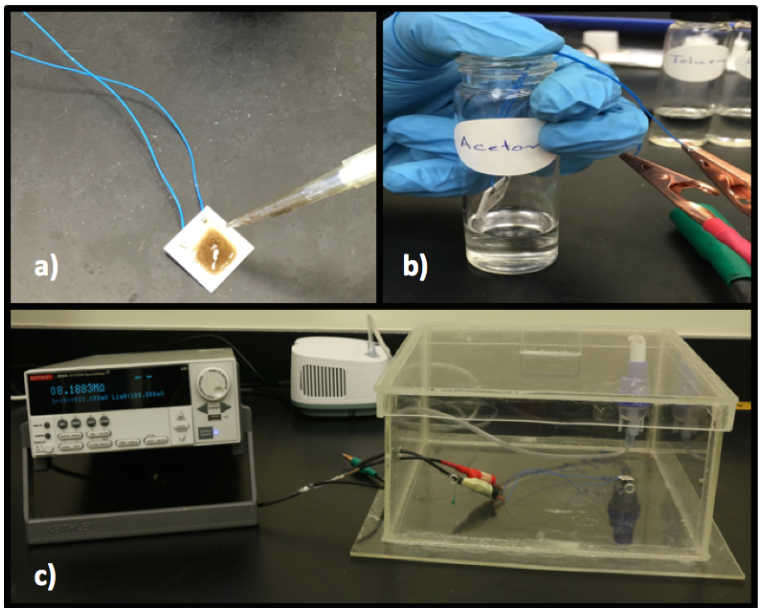


Figure 3. 13. Sensing experimental set up: a) sample dispersed on electrode. b) vapor sensing

(c) the electrode under control conditions

# CHAPTER 4 - RESULTS AND DISCUSSION

## 4.1. Results and Discussion for PVDF/rGO-TNL Composite System

### 4.1.1. Structure & Morphology

#### 4.1.1.1. Scanning Electron Microscopy

Figure 4.1 shows the morphology of the PVDF and its nanocomposites as observed by the SEM. The cryocut samples in liquid nitrogen were used for this analysis and the cross-sectional area is observed through the microscope. Neat PVDF shows a plain type morphology (absence of fillers) as shown in Figure 4.1a. The rGO and TNL are visible as nanolayers in the cross sectional area of the samples as shown in Figure 4.1b and 4.1c respectively. For the hybrid PVDF/rGO-TNL, the nanolayers are homogeneously distributed due to the functional group interaction between both nanomaterials (Figure 4.1d) as will be confirmed by other techniques later on. The oxygen content in the functional groups that present on the surface of rGO can interact with the TNL by hydrogen bonding as well as Vander Waals interactions and this result in good dispersion of the fillers inside the PVDF medium. Similar interaction was reported by Xu et al. [111] for GO nanosheets with starch granules. In their work starch surfaces were covered by the large surface of the GO nanosheets which have high surface energy. The additives in this case with enhanced interfacial interactions had uniform dispersion in the polymer matrix.

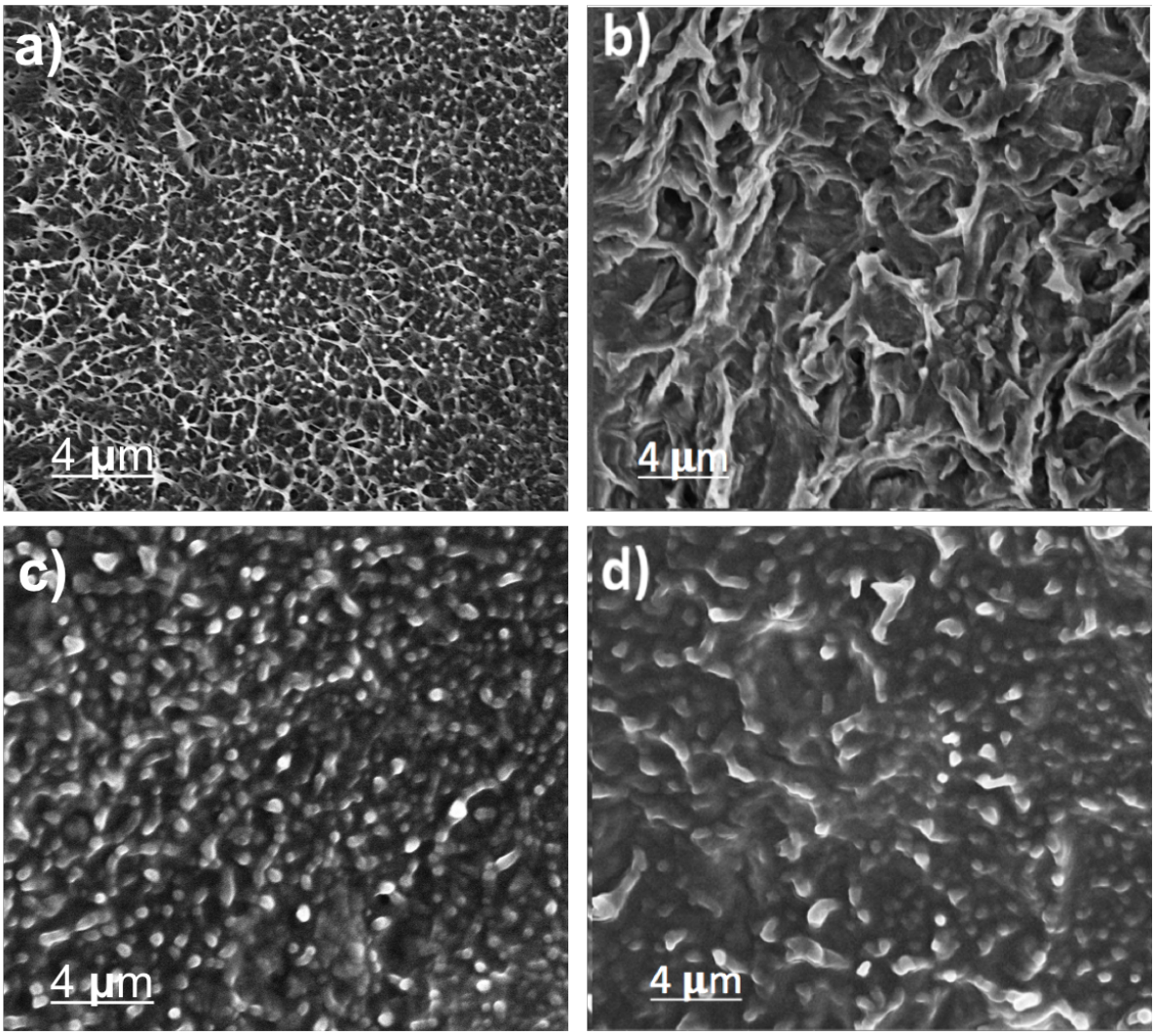


Figure 4. 1. SEM images of a) PVDF b) PVDF/rGO c) PVDF/TNL and d) PVDF/rGO-TNL

#### 4.1.1.2. Transmission Electron Microscopy

Figure 4.2 shows the TEM images of the surface of PVDF, PVDF/TNL, PVDF/rGO, and PVDF/rGO-TNL. These images display a homogenous surface of hybrid composite (Figure 4.2d), compared with PVDF/TNL (Figure 4.2b) and PVDF/rGO (Figure 4.2c) showing some agglomeration and clusters. Agglomeration occurring in PVDF/rGO and PVDF/TNL are represented as focused high resolution images as well. Such homogenous image in PVDF/rGO-TNL indicates that rGO sheets and TNL were fully dispersed in PVDF matrix.

The good dispersion is due to the vander Waals interaction between rGO and TNL sheets [111].

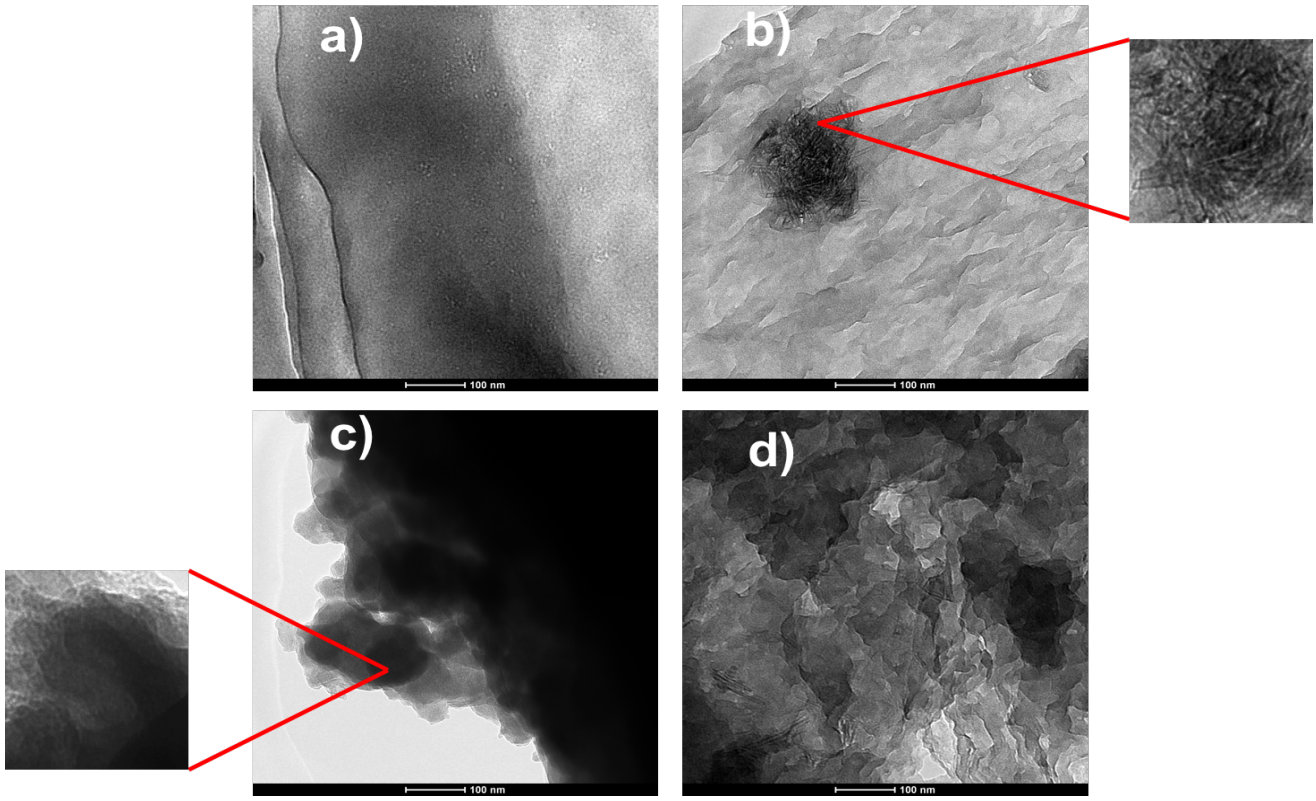


Figure 4. 2. TEM images of surface of a) PVDF b) PVDF/TNL c) PVDF/rGO and d) PVDF/rGO-TNL

#### 4.1.1.3. Atomic Force Microscopy

Figure 4.3 illustrates the AFM images of PVDF, PVDF/TNL, PVDF/rGO and PVDF/rGO-TNL. The average roughness of PVDF is 5.773 nm. With the addition of rGO and TNL the average roughness increased to 6.185 nm (Figure 4.3b) and 6.405 nm (Figure 4.3c) respectively. The average roughness decreased to 3.45 nm in the hybrid composite which indicate smoother surface as seen from Figure 4.3d. This smooth surface reflects the

homogeneous distribution of the fillers. This could be also due to the fusion of TNL on rGO. Similar improvement of the smoothness was reported by Dai et al. [112] for the $Al_2O_3$ with polyurethane and PVDF. One important advantage of such reduction in roughness is its critical applicability in improving the anti-fouling properties of this composite. The smother the surface, the less ability to form fouling [113].

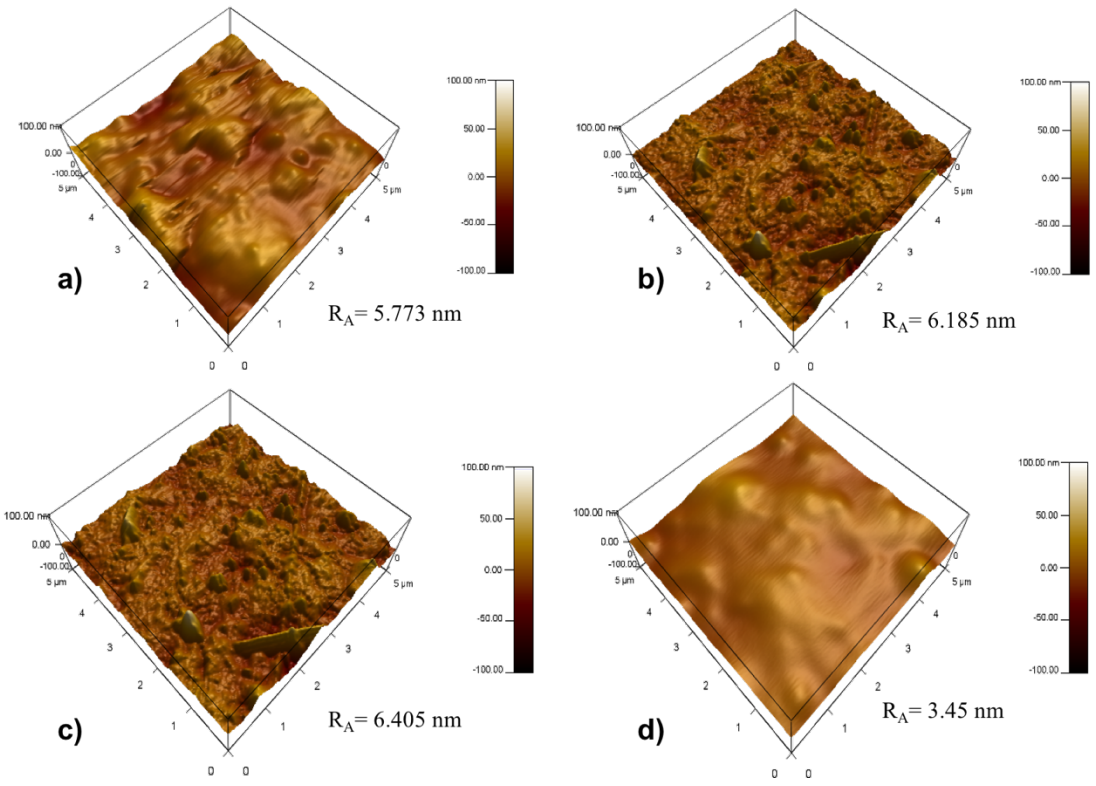


Figure 4. 3. AFM images of surface of a) PVDF b) PVDF/rGO c) PVDF/TNL and d) PVDF/rGO-TNL

Based on different microscopic investigation, it is clear that the nanolayers of rGO and TNL creates a well distributed path within the PVDF in the hybrid PVDF/rGO-TNL composite. Moreover, the individual nanomaterials at 5 wt.% cause agglomeration in the PVDF/rGO and PVDF/TNL composites. This mode of dispersion is represented in Figure 4.4.

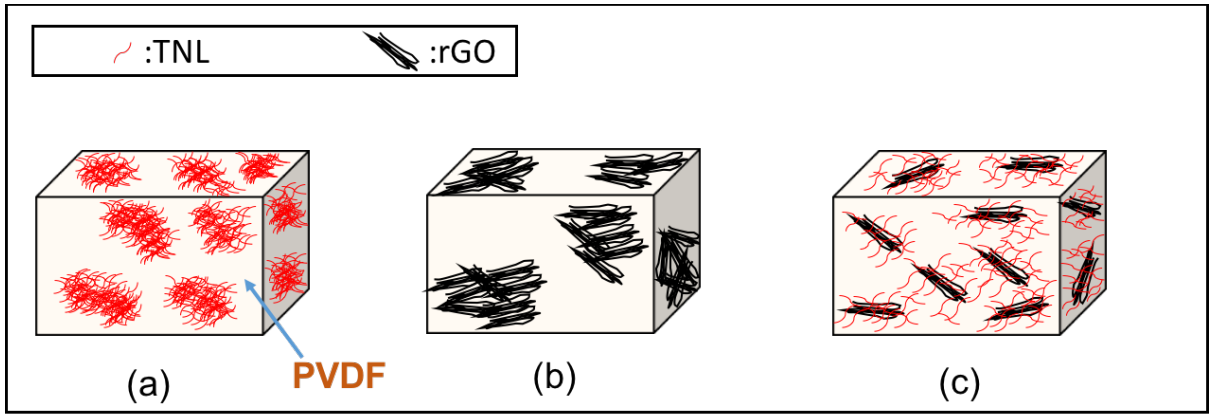


Figure 4. 4. Schematic representation of the dispersion of nanoparticles in (a) PVDF/TNL, (b) PVDF/rGO, and (c) PVDF/rGO-TNL.

#### 4.1.1.4. Fourier Transformation Infrared Spectroscopy

In order to check the structural properties especially the functional groups presented in the material and the chemical modifications, FTIR spectroscopy of the samples were used. Figure 4.5 shows the FTIR spectra for the neat PVDF and PVDF composites.

All the peaks observed in the graph come from the C=C stretching, bending and C-H bending vibrations. The dipole-dipole interaction in PVDF/rGO-TNL is also possible according to the FTIR spectrum. This indicates that there is no chemical bond formation between the filler and polymer, but just physical interaction exists. An interesting factor in the FTIR spectrum is the absence of the characteristic peaks for the C=O, -OH, -COOH etc. functional groups usually associated with the rGO. Following solution mixing, the samples were made homogeneous by hot pressing at 170°C and this might have again reduced the functional groups presented in rGO. All samples show peaks related to PVDF at around 1000 $cm^{-1}$ representing -$CH_2$ rocking and at 800 $cm^{-1}$ representing -$CF_2$ asymmetric stretching [114] vibrations. The FTIR data indicated peak for β phase at 840 $cm^{-1}$ and alpha phase at 764 $cm^{-1}$ [115]. FTIR is

commonly used to identify the β crystalline phases in a polymer by the following equation [92]:

$$F(\beta) = \frac{X_\beta}{X_\alpha + X_\beta} = \frac{A_\beta}{(K_\beta / K_\alpha) A_\alpha + A_\beta} \quad (4.1)$$

where $K_\alpha$ and $K_\beta$ are the absorption coefficients at the particular wave number. $K_\alpha$ is $6.1 \times 10^4$ $cm^2/mol$ and $K_\beta$ is $7.7 \times 10^4$ $cm^2/mol$. $X_\alpha$ and $X_\beta$ are mass fraction of α and β crystalline phases. $A_\alpha$ and $A_\beta$ are the area of absorption bands at 764 and 840 $cm^{-1}$. The relative fraction for β phase using the equation (4.1) are 70.37%, 72.73%, 73.5% and 75.68% for PVDF, PVDF/rGO, PVDF/TNL, and PVDF/rGO-TNL respectively. The results indicate that β phase increased with hybrid PVDF/rGO-TNL additives compared to neat PVDF. The improvement in the β phase (more chains are rearranged at the same side of the fluorine atoms), is due to the good interaction of the hybrid additives with the fluorines in the polymer matrix. Similar improvement was reported for rod like cellulose in a PVDF matrix due to the presence of -OH groups [116].

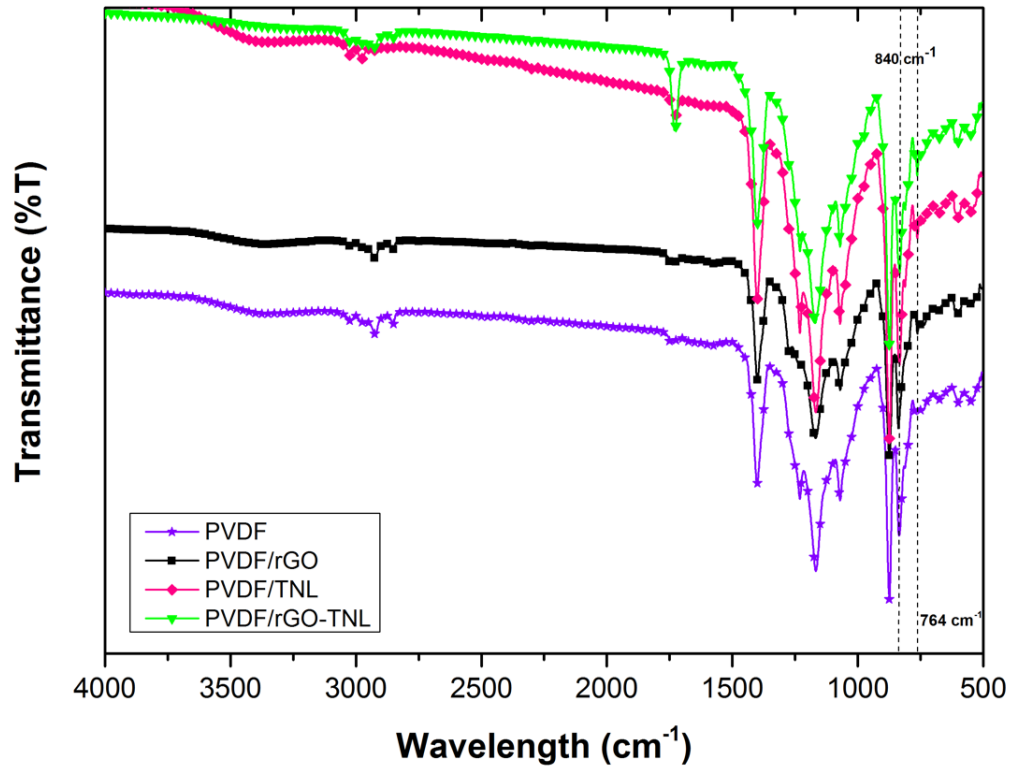


Figure 4. 5. FTIR spectra of PVDF, PVDF/rGO, PVDF/TNL, and PVDF/rGO-TNL.

#### 4.1.1.5. X-Ray Diffraction Studies

X-ray diffractograms for all the composites PVDF, PVDF/rGO, PVDF/TNL and PVDF/rGO-TNL are shown in Figure 4.6. When an X-ray is allowed to fall on a crystalline material, the incident beam interacts with the aligned atoms and thus diffraction occurs. Intensity of diffracted radiations change due to the coherent interference of the individual atoms. The diffraction data in terms of peak position and intensity yields the information on the overall chemistry of the samples. Here all samples show similar peak appearances due to the presence of semi crystalline PVDF in all of them. Eggedi et al. reported that the peaks associated with α phase of PVDF are at 2θ, 18.6°, 20.3° and 27°, whereas β phase found as sharp peak at 20.6° [117]. In our results it can be observed that α peaks are at 18.4°, 19.9°

and 26.6° and the β phase being hidden inside the α peak at 19.9°. It has been observed that the areas of all α peaks were reduced or vanished in the hybrid composite as shown in Table 4.1. The influence of nanoparticles on the XRD patterns depend on the nature of the particles [118], the hybrid additives approximately erased the α peaks, and caused the β peak to be broadened. This indicates that the nanoadditives may interrupt the packing, which will be seen also in DSC results.

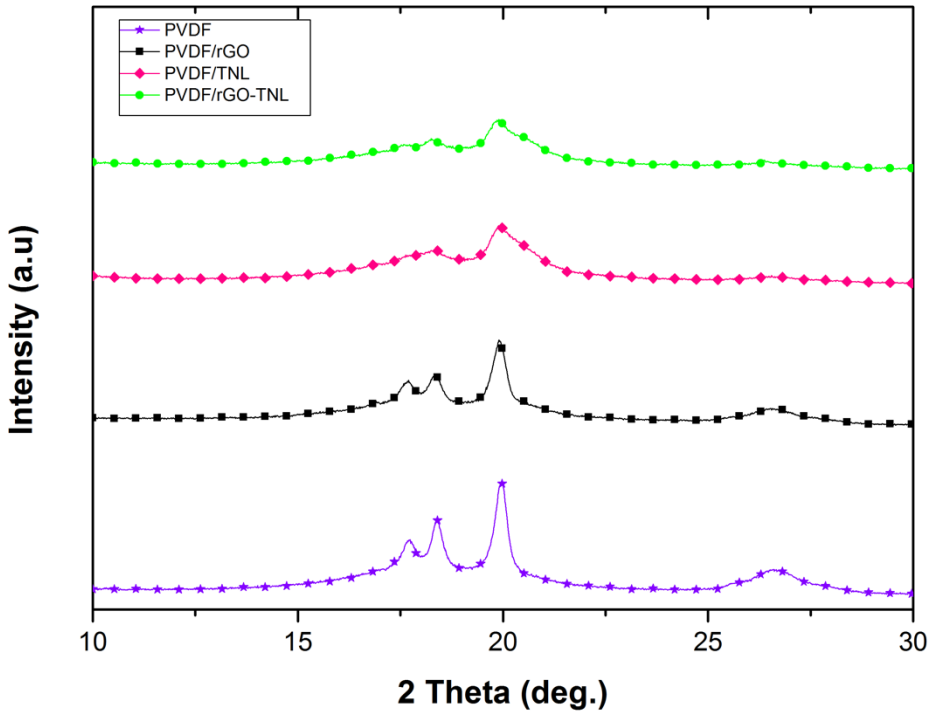


Figure 4. 6. X-ray diffraction pattern of PVDF, PVDF/rGO, PVDF/TNL, and PVDF/rGO-TNL.

Table 4. 1. Details of XRD peaks and areas.

| | α (deg.) | Area | α (deg.) | Area | α (deg.) | Area |
|---|---|---|---|---|---|---|
| **PVDF** | 18.4 | 3276 | 19.9 | 3144 | 26.6 | 2756.5 |
| **PVDF/TNL** | 18.3 | 1290 | 19.94 | 2944 | 26.5 | 621.8 |
| **PVDF/rGO** | 19.34 | 2426 | 19.92 | 2676.3 | 26.5 | 1660 |
| **PVDF/rGO-TNL** | 18.8 | 917 | 19.88 | 2470 | 26.3 | 626.2 |

#### 4.1.1.6. Contact Angle Measurements

The dependence of the water contact angle on the surface of the nanocomposite is calculated and tabulated in Table 4.2. For the neat PVDF, the contact angle is 99.7°, which is also reported elsewhere [119]. The water contact angle decreased for PVDF/rGO to 95.5° due to the partial hydrophilicity of the rGO platelets because of the presence of -OH group on its surface. For the PVDF/TNL, the contact angle has the approximate same value of the neat PVDF. For the PVDF/rGO-TNL, an increase in the contact angle to 114.5° is observed. This can be attributed to the synergistic effect of the fillers producing a network like structure within the composite and the surface as confirmed by TEM and AFM results, and such concentrated filler networks can make the surface more hydrophobic. The contact angle is also related to the interaction parameter; the higher the interaction occurring within the system, the more resistant it will be towards the liquid contacting the surface [120].

Table 4. 2. Contact Angle Measurements of PVDF/rGO-TNL

| Samples | Concentration of rGO (wt. %) | Concentration of TNL (wt. %) | Water Contact Angles (°) |
|---|---|---|---|
| PVDF | - | - | 99.7±4.2 |
| PVDF/rGO | 5 | - | 95.5±3.2 |
| PVDF/TNL | - | 5 | 98.1±3.1 |
| PVDF/rGO-TNL | 2.5 | 2.5 | 114.5±3.5 |

### 4.1.2. Mechanical and Dynamic Mechanical Properties

#### 4.1.2.1. Tensile Properties

The tensile test was performed to examine the mechanical properties of the samples. The obtained values for tensile strength, Young's modulus and elongation at break are shown in Table 4.3.

Table 4. 3. Tensile Test Results of PVDF, PVD-rGO, PVDF-TNL and PVDF/rGO-TNL.

| Samples | Tensile strength (MPa) | Young's Modulus (MPa) | Elongation at Break (%) |
|---|---|---|---|
| PVDF | 21.825±1.93 | 1365.50±101.23 | 16.22±1.45 |
| PVDF/rGO | 22.927±1.197 | 2969±380.6 | 7.352±0.66 |
| PVDF/TNL | 41.53±1.58 | 3112.7±173.60 | 5.40±0.56 |
| PVDF/rGO-TNL | 46.91±0.99 | 5010.65±243.35 | 4.01±0.49 |

The nanoadditives increased the tensile strength and Young's modulus. Among the composites, tensile strength and Young's modulus for the hybrid composite PVDF/rGO-TNL

was 2 and 3.6 times respectively higher than the neat PVDF. The elongation at break was reduced with the addition of the filler and reached its minimum value of 4% for the hybrid composite compared to 16% for the neat PVDF sample. This indicate the brittle behavior of the hybrid composite. The improvement in the mechanical properties can be attributed to the increase in the β crystallites in the matrix (confirmed by FTIR measurements). AlMaadeed et al. [121] reported the effect of the increase in crystallinity on modification of the tensile strength in a polyethylene polymer with addition of date palm wood flour/glass fiber. Also Issa et al. [92] fabricated electrospun PVDF/cellulose nanocomposite and they mentioned that the increase in crystallinity and crystal orientation can increase the tensile strength of the PVDF.

The enhanced mechanical properties of PVDF/rGO-TNL hybrid nanocomposite can be correlated with two factors; (1) the interfacial interactions existing between the rGO and TNL as well as the fillers and the PVDF, (2) the synergistic effect of the fillers. It is well established that the synergistic effect can enhance the mechanical properties of the sample [22]. The filler content in the PVDF/TNL and PVDF/rGO (5 wt.%) is considered high and possibility of agglomeration and clusters formation in the matrix lead to less interfacial interactions and decreases the mechanical properties.

The images of the fractured surfaces after mechanical deformation by tensile test are shown in Figure 4.7. It clearly shows a ductile fracture for PVDF as the fractured surfaces of the tensile test specimens cut showed deep cavities (Figure 4.7a). The fractured surface of PVDF/rGO shows a microcrack as indicated in Figure 4.7b. Figure 4.7c shows fewer cavities in the fracture surface. The ductility is reduced in Figure 4.7d. These results are also confirmed by the tensile test values from Table 4.2.

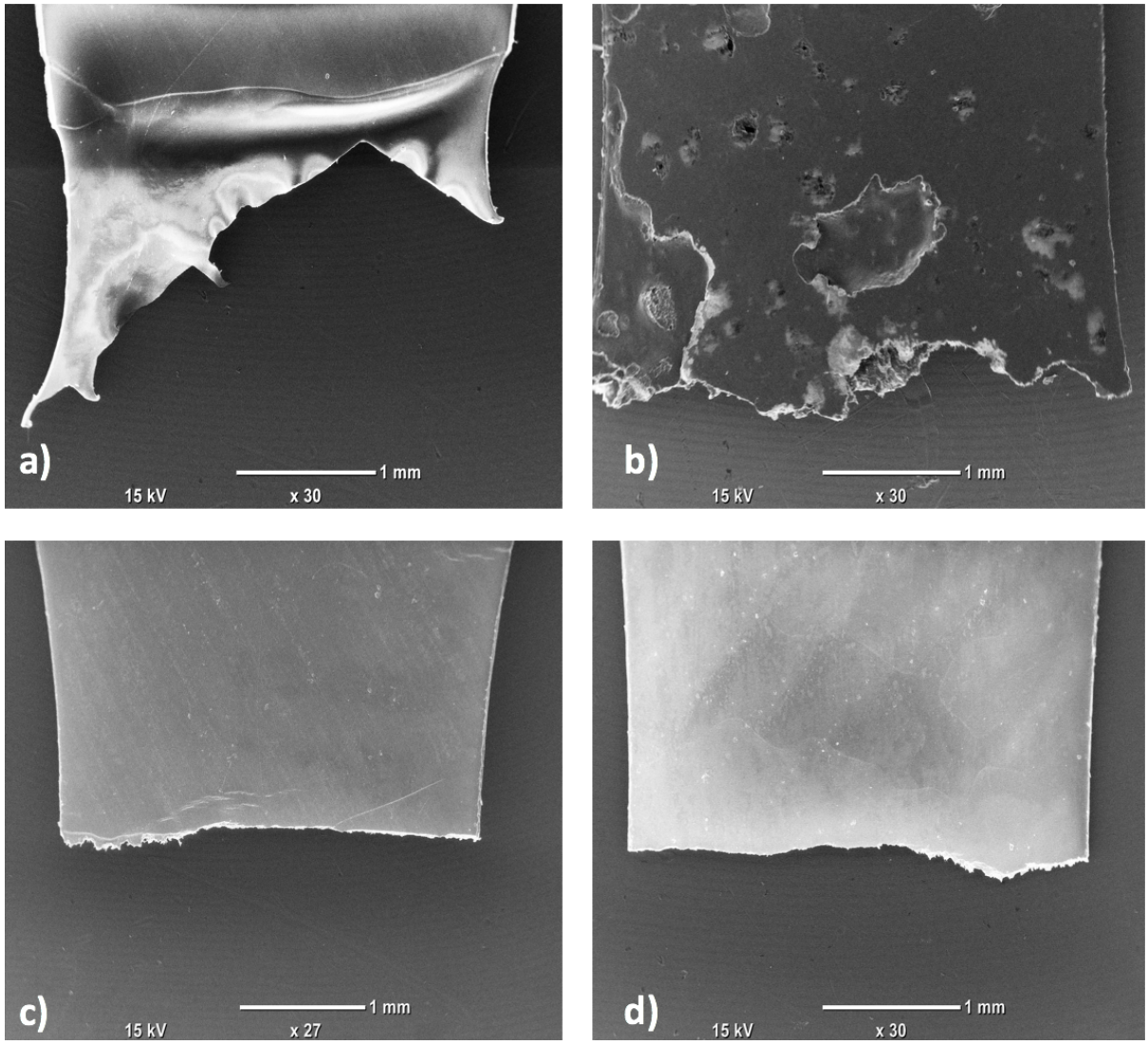


Figure 4. 7. SEM images of surface of tensile test specimen cut a) PVDF b) PVDF/rGO c) PVDF/TNL and d) PVDF/rGO-TNL.

#### 4.1.2.2. Dynamic Mechanical Analysis

Figure 4.8 shows the variation in storage modulus of the samples as a function of frequency. The hybrid composite, PVDF/rGO-TNL has higher storage modulus compared to other samples. This indicates that this composite has good property in storing energy for piezoelectric applications [22]. The improvement in the storage modulus can be attributed to the improvement in the $\beta$ crystal formation [122], or the better interaction between the matrix

and the filler. It is also important to note that the high rigidity of the additives contributes to this improvement which was also reported elsewhere [92].

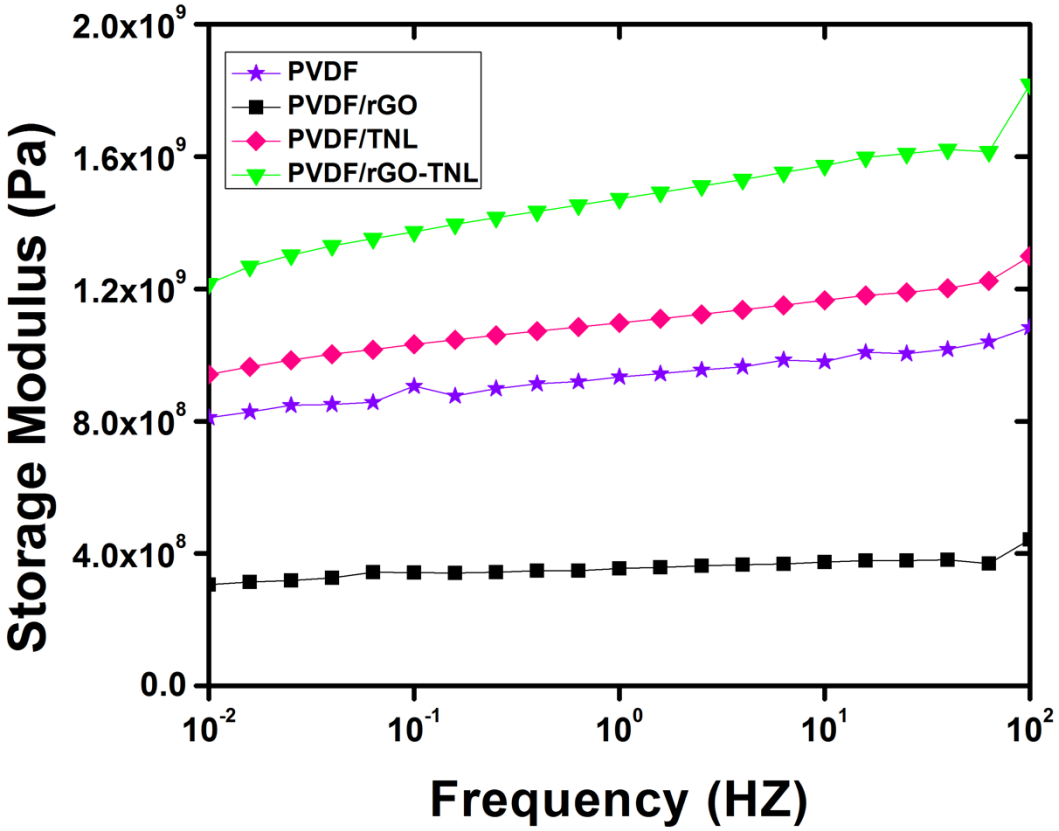


Figure 4. 8. Variation of storage modulus with frequency for PVDF, PVDF/rGO, PVDF/TNL, PVDF/rGO-TNL.

### 4.1.3. Thermal Properties

#### 4.1.3.1. Differential Scanning Calorimetry

DSC was performed to study the changes in melting enthalpy ($\Delta H_m$), melting temperature ($T_m$), and degree of crystallinity ($X_c$) as shown in Table 4.4. The degree of crystallinity ($X_C$ ) of the polymer was calculated using the following equation (4.2):

$$X_c = \Delta H_m / \Delta H^\circ_m \quad (4.2)$$

Where $\Delta H_m$ is the melting enthalpy of the polymer and $\Delta H^\circ_m$ is melting enthalpy of pure polymer. The melting enthalpy for pure PVDF is 105 $Jg^{-1}$ [123]. Figure 4.9a shows the melting peak of PVDF has two shoulders, indicating two types of crystallites [124] with two different lamellae thicknesses [125]. This peak is shifted to a higher temperature with the addition of the fillers. The melting point is increased from 167.3 °C for pure PVDF to 169.2 °C for PVDF/rGO. PVDF/TNL and PVDF/rGO-TNL have similar high melting point around 170 °C.

Table 4. 4. DSC data of PVDF/rGO-TNL, PVDF/rGO, PVDF/TNL, and PVDF.

| **Sample** | **Crystallization Temperature (°C)** | **Melting Temperature (°C)** | **$\Delta H_m$ (J/g)** | **Degree of Crystallinity ($X_c$)** |
|---|---|---|---|---|
| PVDF | 137.16 | 167.33 | 48.5392 | 46.227 |
| PVDF/rGO | 140.91 | 169.19 | 47.4923 | 45.23 |
| PVDF/TNL | 143.49 | 170.27 | 43.0843 | 41.03 |
| PVDF/rGO-TNL | 142.1 | 170.63 | 40.2879 | 38.36 |

The cooling peaks in figure 4.9b are also affected by the additives. The crystallization temperature increased by 5 °C for rGO addition and around 7 °C for TNL addition. The hybrid additives increased the crystallization temperature by 6 °C. This increase in temperature indicates the easiness of the crystallization with the addition of these fillers. These additives act as nucleating agents that encourage the formation and growth of the crystallites in the polymer [126]. Table 4.4 shows the decrease in crystallinity for PVDF/rGO-TNL compared to PVDF. The increase in the melting points indicates that the increase in lamellae does not guarantee the increase in the crystallinity percentage in the polymer. The crystallinity percentage depends on other factors such as length, distribution and curvature as well [127]. According to XRD results, there is a reduction (erase) in the α phase and change in the β phase peak. Dai et al. [112] reported that additives that were distributed uniformly in the matrix interrupted the packing of chains and decreased the crystallinity.

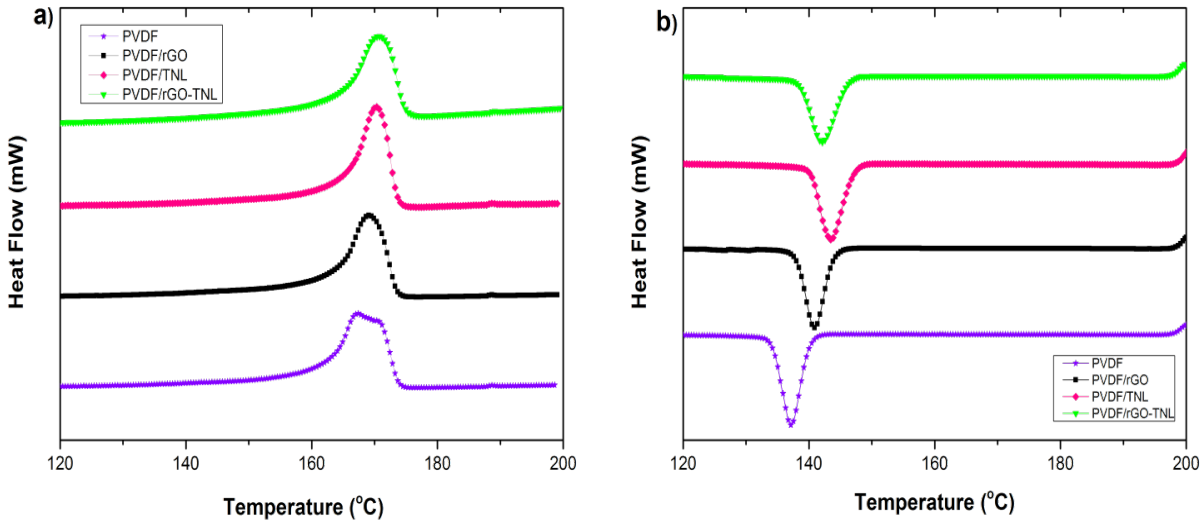


Figure 4. 9. DSC analysis for PVDF and its nanocomposites (a) Melting curve (b) Crystallization curve.

### 4.1.4. Dielectric Properties

Figure 4.10 shows the frequency ($f$) dependence on the dielectric permittivity ($\varepsilon'$) and loss ($\varepsilon''$) of different nanocomposites. The dielectric permittivity storage ($\varepsilon'$) is slightly unchanged for the PVDF and one type of additive but it decreases as $f$ increases for the PVDF/rGO-TNL sample. Decrease in $\varepsilon'$ with increasing $f$ is due to reduction in the ability of the dynamics of polarization to be apprehended within shorter signal time scales, that is, decreasing $1/2f$ [128]. Also, one would expect higher contribution from the sample/electrode interfacial polarization at low $f$, which is not a bulk material phenomenon but caused by blocking electrodes at the sample surfaces [129]. Drop in $\varepsilon'$ at high $f$ is due to the β-relaxation dispersion, which is active within this temperature range [92]. The β-relaxation is ascribed to the long-range motions of chain segments within the crystalline–amorphous interphase [92], [130]. Also, some researchers link this relaxation to the micro-Brownian motions of chain segments within the amorphous phase [131].

PVDF/rGO and PVDF/TNL samples have lower $\varepsilon'$ values when compared to the unfilled PVDF. This trend is perhaps due to the agglomeration of the relatively more conductive fillers (rGO and TNL) which was confirmed by the TEM in Figure 4.2. Agglomeration of the nanoparticles would cause trapping of charges at their interfaces due to the Maxwell–Wagner–Sillars (MWS) interfacial polarization effect [132]. Whereas the hybrid PVDF/rGO-TNL exhibits higher $\varepsilon'$ due to the good dispersion of rGO and TNL within the PVDF matrix. Well dispersed material reduces the traps of charges within interfaces and form a good conductive composite [g]. The hybrid PVDF/rGO-TNL composite has the highest polarizable components, which means higher ability to store electrical charges and could be useful as a supercapacitor material [133], [134]. For example, the dielectric constant of the hybrid composite at 100 Hz is 3.6 times higher than that of the unfilled PVDF.

These new tailored nanocomposites can be used as good candidates for energy storage

systems can be observed in Figure 4.10b, which illustrates the high $\varepsilon'$ relative to $\varepsilon''$ values for all samples, in the BDS spectra at 25 $^{o}$C. This indication is further supported by the samples conductivity vs. $f$ behavior shown in Figure 4.11. Both PVDF/rGO-TNL and PVDF/rGO composites have higher conductivity compared to other samples as indicated by the vertical upshifts and the presence of plateau regions at low $f$. The maximum electrical energy ($U_{max}$) which can be stored in a linear dielectric material is given by:

$$U_{max} = \varepsilon' {E_b}^2/2 \tag{4.4}$$

where $E_b$ is the dielectric breakdown strength (DBS). For efficient electric energy storage, high DBS and $\varepsilon'$ are required [133].

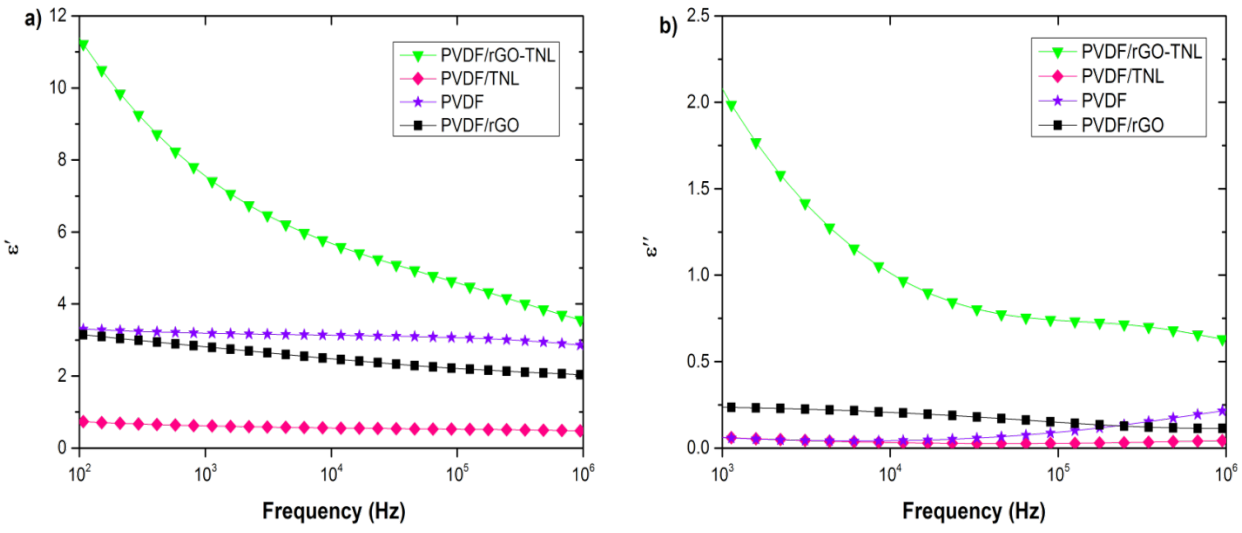


Figure 4. 10. Dielectric permittivity storage (a), and loss (b) of PVDF control and its composite samples with variable nanoparticle fillers.

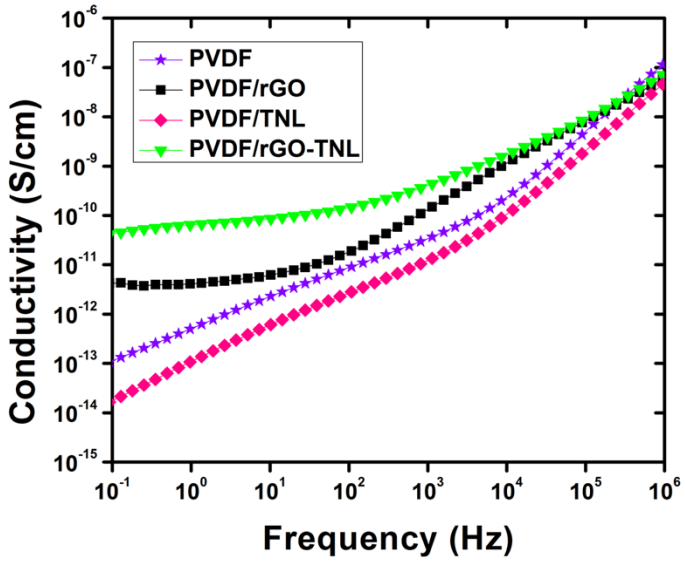


Figure 4. 11. Conductivity vs. $f$ at 20 $^{o}$C for the PVDF/rGO-TNL composite samples with variable nanoparticle fillers.

### 4.1.5. Pressure Sensing Behavior

The relative resistance variation of flexible PVDF/rGO-TNL, PVDF/TNL, and PVDF/rGO composites, for the first four cycles are illustrated in Figure 4.12. PVDF/rGO-TNL has the highest relative resistance compared to other composites for all the three applied pressures. For each composite, upon pressure, the relative resistance decreased immediately. Tunneling is the common mechanism by which the electric current move between the electrodes in pressure sensing [78]. The compression of the sample reduces the tunneling barriers and a tunneling path can be formed which leads to reduction in the resistivity of the composite. TNL effect is lower than rGO in improving the tunneling (for example the relative resistance reduced by 334.7 % and 70.27 % respectively at pressure of 5 kPa). The agglomeration of nanoparticles in the matrix (while using one type of additive) does not allow formation of conducting paths. When pressure is applied to the sample, the agglomerated additives follow

the movement of the polymer chains and cause forming conducting networks of the sample [h]. The largest improvement in the hybrid composite can be attributed to the less agglomeration in the matrix and better dispersion. The sensitivity of hybrid composite increased by 333.46% at 5 kPa, by 200.7% at 10.7 kPa and 246.7% at 17.6 kPa compared to the PVDF/TNL.

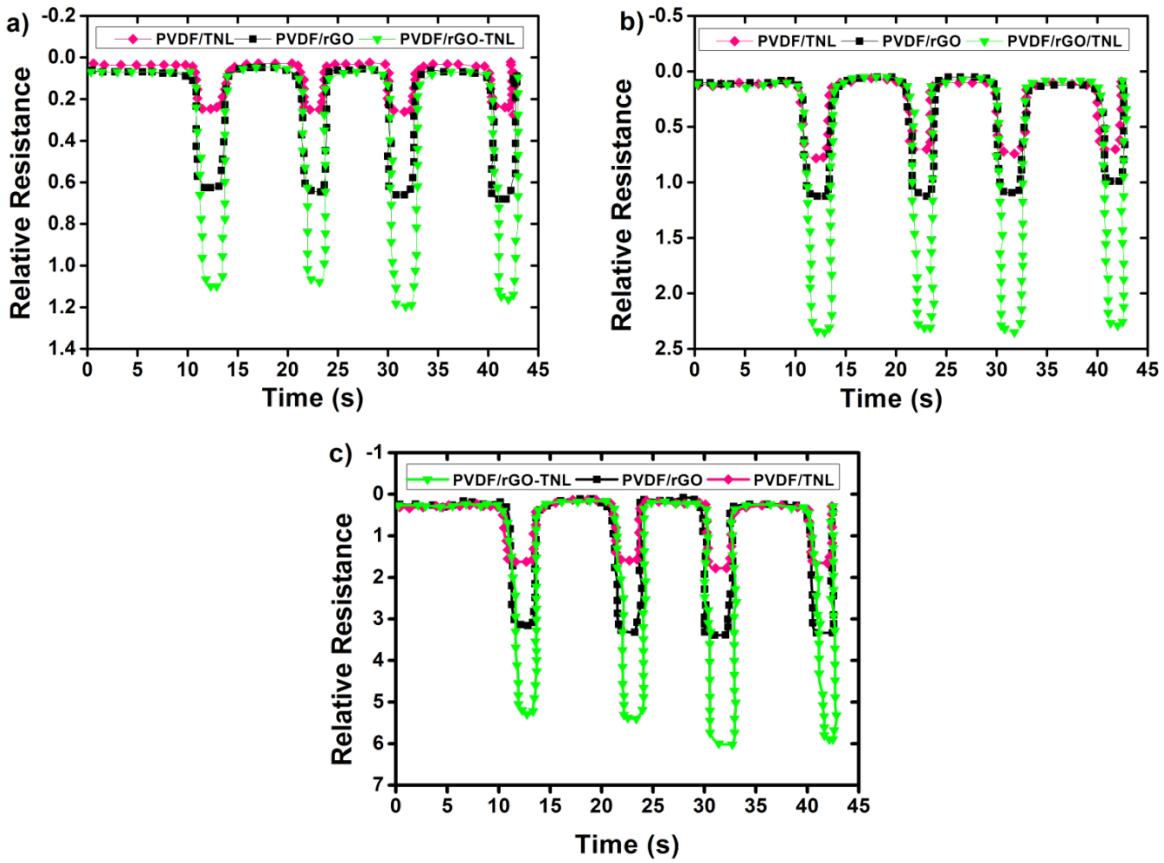


Figure 4. 12. Sensing responses of PVDF/rGO, PVDF/TNL and PVDF/rGO-TNL composites to (a) 5 kPa (b) 10.7 kPa (c) 17.6 kPa.

For one type of additives: The morphology of the additives plays a major role in improving the tunneling effect. The influence of pressure on the conducting networks present within the

composite is schematically represented by Figure 4.13a. With the application of pressure, the distributed nanolayers come closer (more agglomeration) and thereby decreasing the resistance of the sample. These conducting networks can be formed among the different conducting particles like rGO and TNL.

For PVDF/rGO-TNL: This aspect is schematically demonstrated in Figure 4.13b. The presence of sharp and nanostructured tips can also improve the tunneling [135] as shown in the same figure. Thus the interaction between the TNL and rGO with "sharper" morphology can increase the tunneling effect, thereby enhancing the magnitude of relative resistance change and offers better pressure detection.

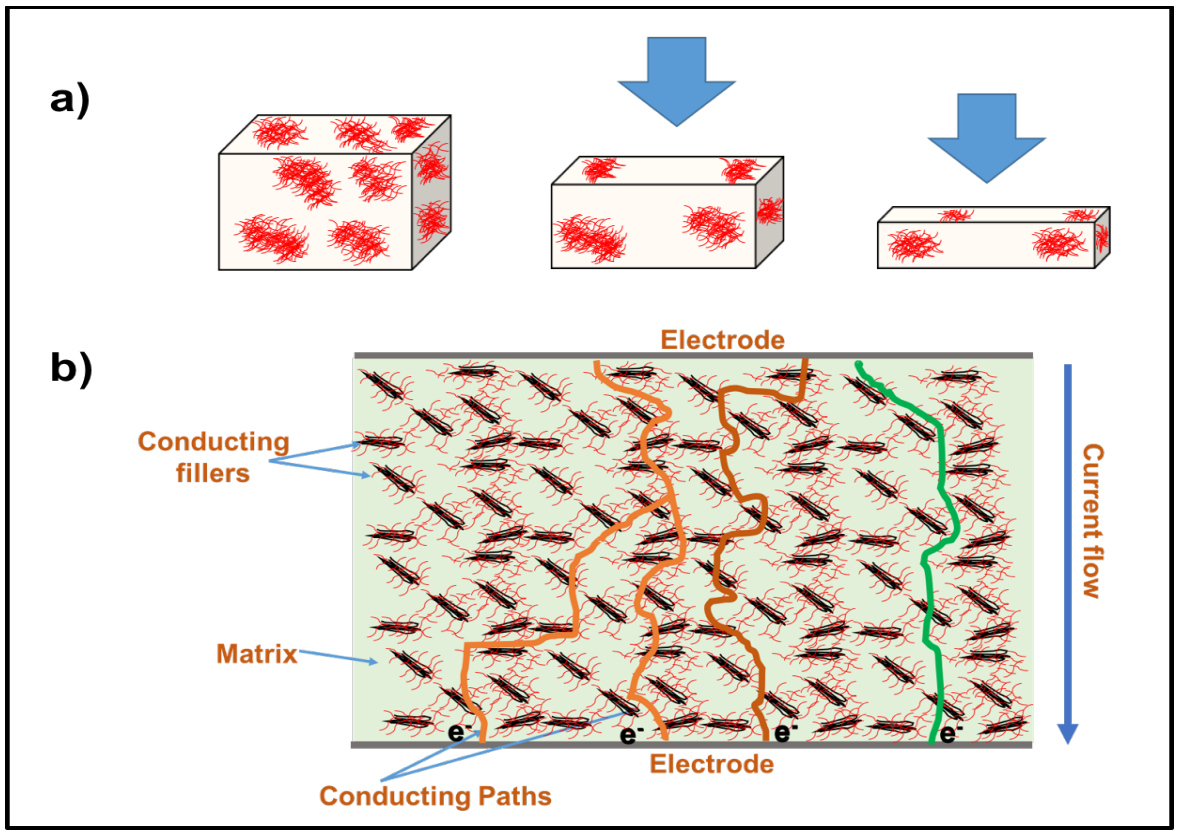


Figure 4. 13. Schematic of (a) mechanical behavior of TNL under applied compress force agglomeration additives that have higher distance after compression (b) conducting network formation between TNL, rGO and TNL-rGO particles.

### 4.1.6. Vapor Sensing Behavior

Volatile organic compounds (VOCs) are non-polar and polar that can cause health effects contribute to sick building syndrome and mostly can cause cancer. Indoor air quality measurements control the effects of emission vapor to human. non-polar compounds are most dangerous type of VOCs. Sensors are used to monitor air quality and to provide safe area for humans, specially in labs, and industries. Some of metal-oxide sensors were fabricated for gas pollutant detection: CNT film was used to detect $NO_X$, and Tungsten trioxide ($WO_3$) sensor synthesized to detect level of ozone gas [136].

The sample responses to three different vapors of organic volatile liquids: Acetone, THF, and DMF were recorded by means of their relative resistance change and represented in Figure 4.14. The composites were less detecting to non-polar solvent vapors, Toluene, xylene and benzene, though tests are conducted using such vapors as well. Thus the samples can be used as electronic nose (e-nose) to distinguish between polar and non-polar solvent vapors. This can be due to the presence of benzene ring in the case of non-polar liquids which makes the penetration of solvent molecules through the polymer chains difficult [137].

In the case of Acetone, the relative resistance of the hybrid composite is higher by 282 % than TNL alone. In the case of THF, the relative resistance of the hybrid composite is higher by 136 % than TNL alone. And in the case of DMF, the relative resistance of the hybrid composite is higher by 94 % than the TNL individual composite. The relative resistance chart as shown in figure 4.15 indicates that PVDF/rGO-TNL hybrid composite has higher relative resistance 0.97, 0.84 and 0.69 for THF, DMF and Acetone respectively. Whereas the low relative resistance for Benzene, Toluene and Xylene were 0.55, 0.2 and 0.1 respectively.

The mechanism of vapor sensing is different from that of the pressure sensing. In pressure sensing, when the pressure was applied, new conducting networks were formed

between particles and thus relative resistance decreases. But in vapor sensing, when the vapors come in contact with the material, the polymer chain swells allowing the solvent molecules to get inside the polymer network, thereby reducing the inter particle distance and resulting in an increase in the relative resistance. Hazra et al. discussed the mechanism of gas sensing devices, it was mentioned that rGO and GO have ability to trap gas molecule and that can changes the conducting properties [138].

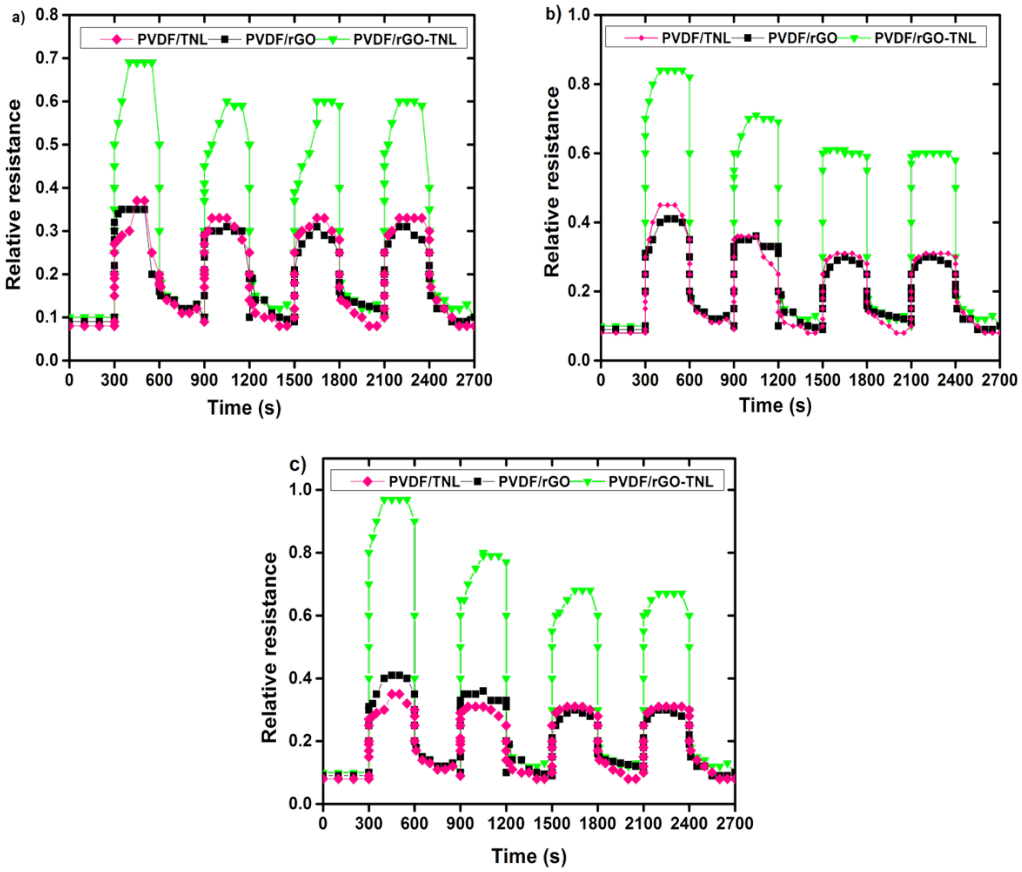


Figure 4. 14. Vapor sensing responses of PVDF/rGO-TNL nanocomposite with different solvent (a) Acetone (b) THF and (c) DMF

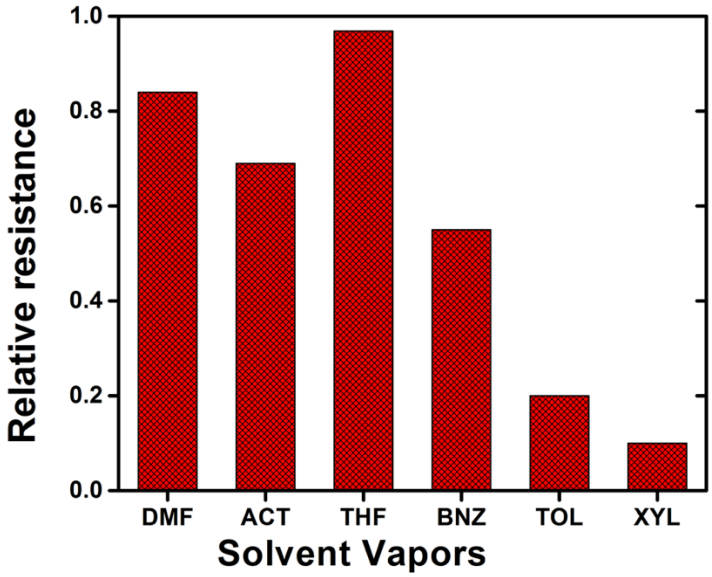


Figure 4. 15. Comparison of different solvents on PVDF/rGO-TNL nanocomposite

## 4.2. Results and Discussion for PVDF/rGO-FeO Composite System

### 4.2.1. Structure & Morphology

#### 4.2.1.1. Scanning Electron Microscopy

Figure 4.16 shows the morphology of PVDF, PVDF/rGO, PVDF/FeO and the hybrid PVDF/rGO-FeO composite. All images show the cross-sectional area of cryocut samples. Figure 4.16a and 4.16b show the morphology of PVDF and of PVDF/rGO respectively. Figure 4.16c shows the FeO nanoparticles presented inside the PVDF matrix. Figure 4.16d shows the uniform dispersion of rGO and FeO fillers within the PVDF matrix.

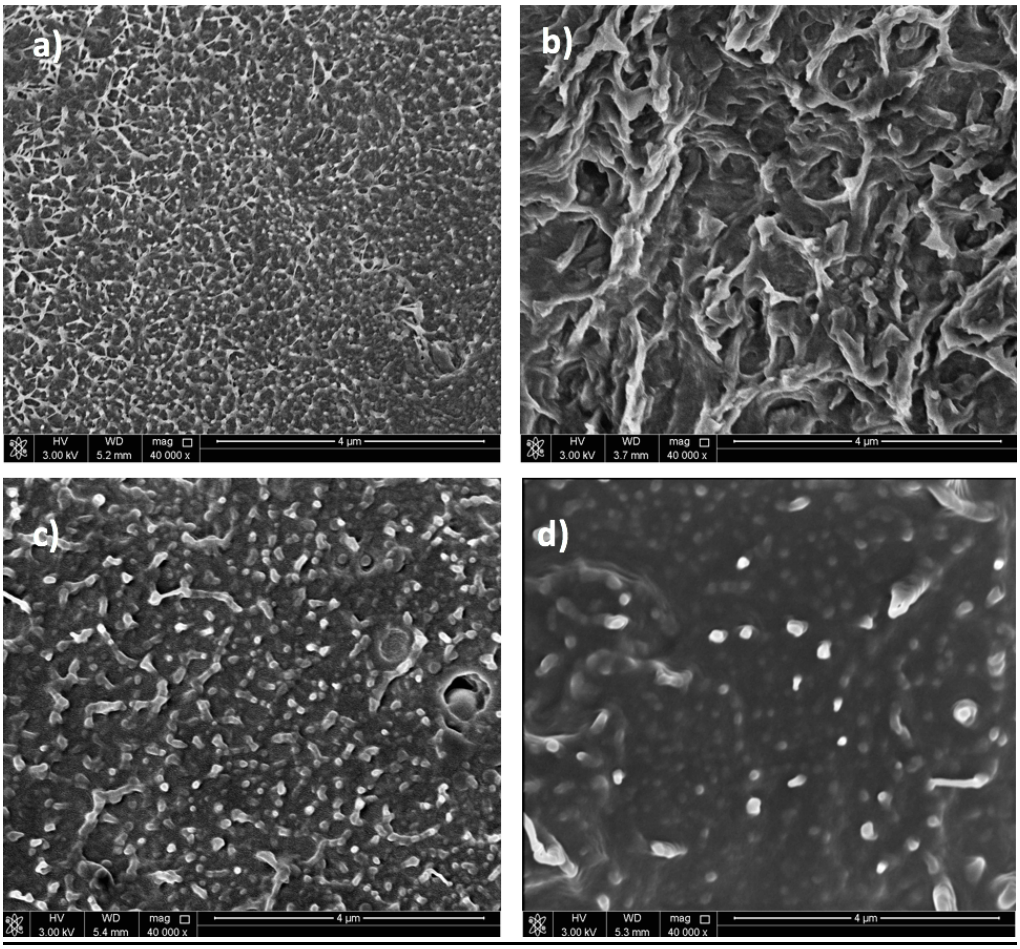


Figure 4. 16. SEM images of a) PVDF b) PVDF/rGO c) PVDF/FeO and d) PVDF/rGO-FeO

#### 4.2.1.2. Transmission Electron Microscopy

Figure 4.17 display the TEM micrographs of PVDF, PVDF/rGO, PVDF/FeO, and PVDF/rGO-FeO. As discussed in section 4.1.1.2., these images give detailed structural information of the composites. The sheet like morphology of rGO and spherical nature of FeO are clear from the images. The average particle size of FeO is 30 nm. In the hybrid composite PVDF/rGO-FeO, the rGO nanolayers and FeO nanoparticles, mutually allow well distribution of the fillers as observed in Figure 4.17d.

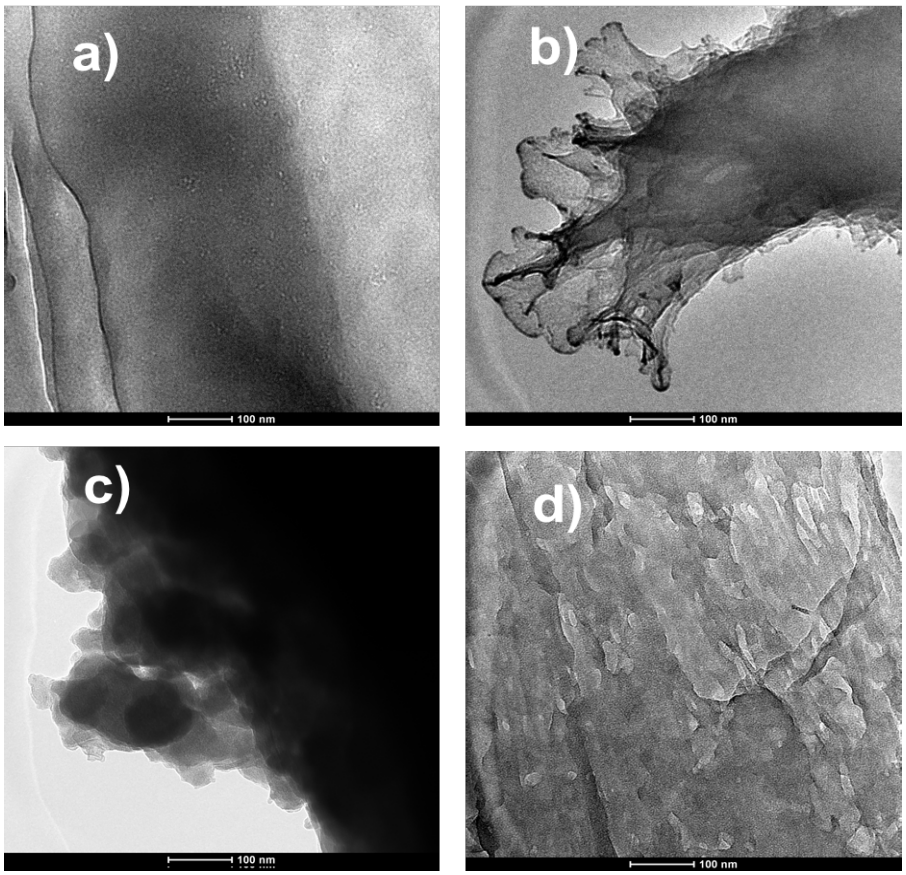


Figure 4. 17. TEM micrographs of PVDF, PVDF/rGO, PVDF/FeO, and PVDF/rGO-FeO.

#### 4.2.1.3. Atomic Force Microscopy

AFM results are shown in Figure 4.18. The PVDF and PVDF/rGO films represented in Figure 4.19a and b respectively gives a roughness of 5.773 nm for PVDF and of 6.185 nm for PVDF/rGO. Whereas the addition of FeO particles to PVDF increase the roughness to 9 nm (Figure 4.18c). This can be due to the agglomeration at a higher filler concentration of 5 wt.% for the FeO composite. In the hybrid composite, PVDF/rGO-FeO, (Figure 4.18d) the roughness is 1.7 nm. This can be attributed to the good dispersion of both one dimensional and two dimensional fillers in PVDF matrix as confirmed by TEM and SEM studies.

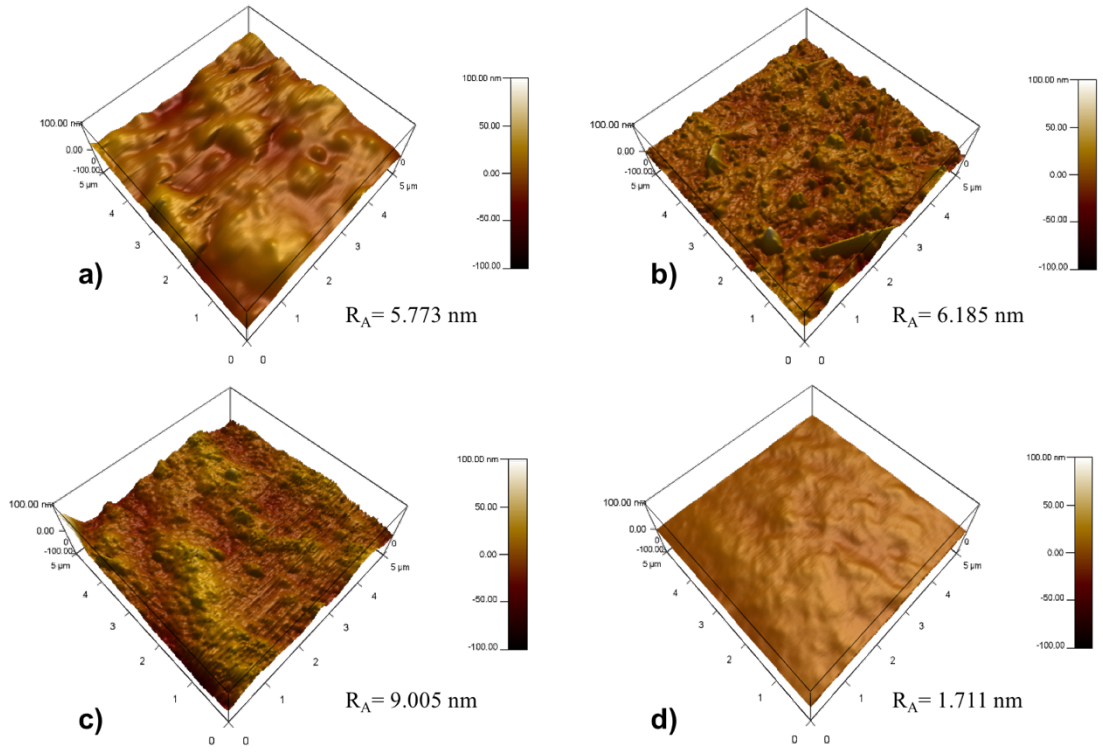


Figure 4. 18. AFM images of surface of a) PVDF b) PVDF/rGO c) PVDF/FeO and d) PVDF/rGO-FeO

#### 4.2.1.4. Fourier Transformation Infrared Spectroscopy

Figure 4.19 shows the FTIR spectra for the neat PVDF, PVDF/rGO, PVDF/FeO, and PVDF/rGO-FeO composites. All the peaks observed for PVDF and PVDF/rGO samples in Figure 4.20 were explained in part 4.1.1.4. In PVDF/rGO-FeO, the peaks corresponding to –OH, -CO- and –COOH vibrations were not observed due to the well interaction between the rGO and FeO with the PVDF polymer. Equation (4.1) was used to calculate the β crystalline phases in all samples. As a result, the relative fraction for β phase were respectively found as 70.37%, 72.73%, 90.9% and 93.7% for PVDF, PVDF/rGO, PVDF/FeO, and PVDF/rGO-FeO. The results indicate that β phase increased for hybrid PVDF/rGO-FeO additives compared to the neat PVDF. The reason for the increase in the β phase fraction for PVDF/FeO, and PVDF/rGO-FeO is the presence of FeO particles that has spherical shape.

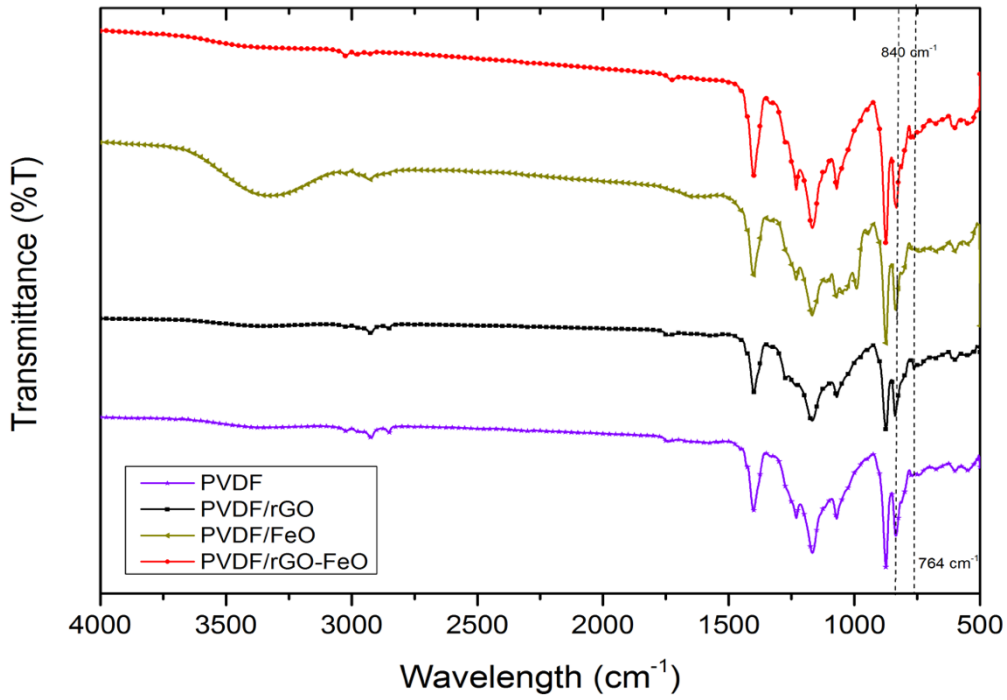


Figure 4. 19. FTIR spectra of PVDF, PVDF/rGO, PVDF/FeO, and PVDF/rGO-FeO.

#### 4.2.1.5. X-Ray Diffraction Studies

The XRD spectra of pure PVDF, PVDF/rGO, PVDF/FeO and PVDF/rGO-FeO composites are shown in Figure 4.20. Positions of α and β phases were observed similar to section (4.1.1.5). The figure indicates that the sharp α phases present in the neat PVDF and individual filler composite is changed to broader peaks in hybrid polymer nanocomposite. This indicate that the α phase is started to be erased.

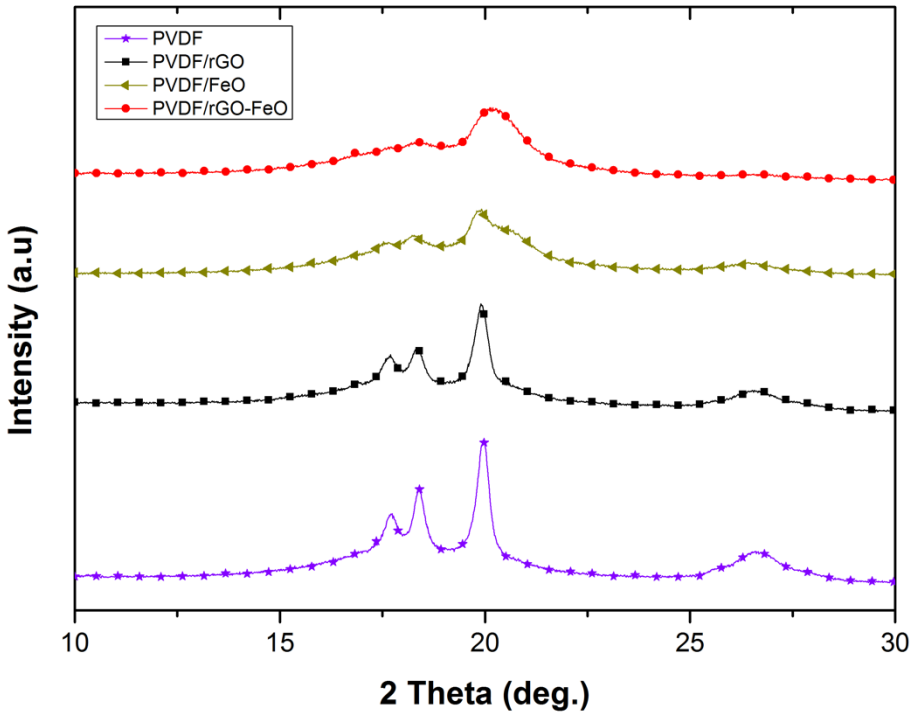


Figure 4. 20. X-ray diffraction pattern of PVDF, PVDF/rGO, PVDF/FeO, and PVDF/rGO-FeO.

#### 4.2.1.6. Contact Angle Measurements

Table 4.5 shows the measurements of water contact angle on the sample surfaces. The hydrophilicity increases with addition of rGO to PVDF as reported before. With addition of FeO particles the hydrophilicity of PVDF surface again increases to 92.62°. However, the surface contact angle for PVDF/rGO-FeO is 106.98°. The increase in the hydrophobicity can be attributed to the interaction of FeO particles with the rGO layers. This further substantiates good inter particle interaction and well distribution and synergy between the hybrid nano additives.

Table 4. 5. Contact Angle Measurements of PVDF/rGO-FeO

| Samples | Concentration of rGO (wt. %) | Concentration of FeO (wt. %) | Water Contact Angles (°) |
|---|---|---|---|
| PVDF | - | - | 99.7±4.2 |
| PVDF/rGO | 5 | - | 95.5±3.2 |
| PVDF/FeO | - | 5 | 92.62±1.25 |
| PVDF/rGO-FeO | 2.5 | 2.5 | 106.98±4.82 |

### 4.2.2. Mechanical and Dynamic Mechanical Properties

#### 4.2.2.1. Tensile Test

The mechanical properties obtained from the tensile tests are represented in Table 4.6. The tensile strength for PVDF/rGO-FeO is 27 % higher than neat PVDF. The value for Young's modulus increased from 1365 MPa for neat PVDF to 18852 MPa for the PVDF/rGO-FeO composite. The percentage of elongation was reduced from 16 % of neat PVDF to 2.18% of PVDF/rGO-FeO composite. Compared to the PVDF/rGO and PVDF/FeO composite, the enhancement in tensile properties for the hybrid PVDF/rGO-FeO is attributed to its filler distribution and the synergistic structural combination. Both fillers made a good networking within the PVDF, allowing effective stress transfer between the polymer and the additives. Thus that the hybrid composite material became stronger and with reduced ductility.

Table 4. 6. Tensile test results of PVDF, PVDF/rGO, PVDF/FeO, PVDF/rGO-FeO

| **Samples** | **Tensile strength (MPa)** | **Young's Modulus (MPa)** | **Elongation at Break (%)** |
|---|---|---|---|
| PVDF | 21.825±1.93 | 1365.50±101.23 | 16.22±1.45 |
| PVDF/rGO | 22.927±1.197 | 2969±380.6 | 7.352±0.66 |
| PVDF/FeO | 25.738± 5.3 | 2567.5±170.5 | 5.577± 0.627 |
| PVDF/rGO-FeO | 27.81±7 | 18852±199.3 | 2.1861±0.428 |

Figure 4.21 shows the images of the fractured surfaces after mechanical deformation by tensile test. These SEM images confirm the ductile nature of PVDF and its composites. The fracture of PVDF is shown in Figure 4.21a, and the ductility reduced in the case of PVDF/rGO and PVDF/FeO composites (Figure 4.21b and Figure 4.21c) due to the presence of nano fillers. It is clearly shown in Figure 4.21d that the hybrid PVDF/rGO-FeO composite has more flat brittle fracture. These results are also in correlation with the tensile test values in Table 4.6.

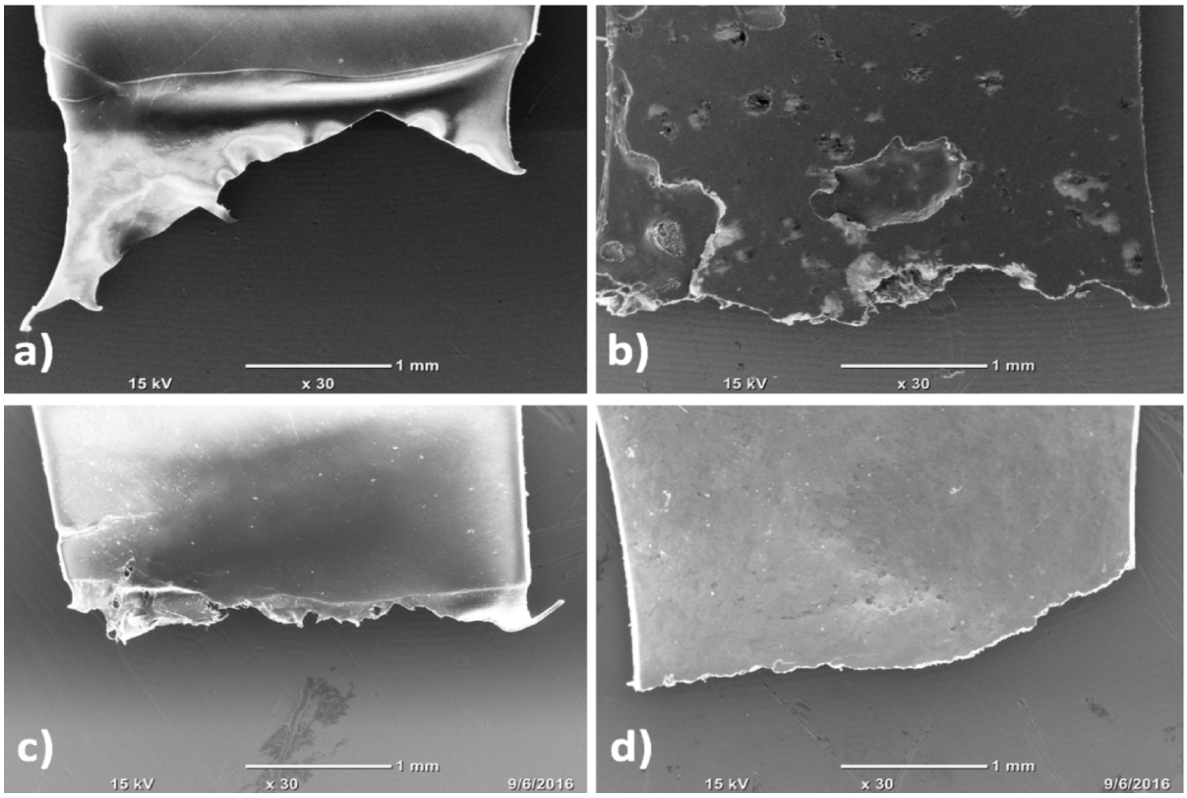


Figure 4. 21. SEM images of surface of tensile test specimen cut a) PVDF b) PVDF/rGO c) PVDF/FeO and d) PVDF/rGO-FeO.

#### 4.2.2.2. Dynamic Mechanical Analysis

Figure 4.22 shows the DMA results for PVDF and its composites containing rGO and FeO. The frequency sweep experiments reveal some unusual behavior for the FeO and rGO containing sample. This decrease in storage modulus with respect to frequency for the PVDF/rGO and PVDF/FeO at 5 wt.% concentration can be attributed to the hindrance of flow behavior by the agglomerated filler clusters. However, for the hybrid PVDF/rGO-FeO composite, the modulus is higher than the others, which means its ability to store energy is higher than the rest. The storage modulus of the hybrid composite increases with the increase

in the frequency as well. At 100 Hz, the storage modulus for the hybrid composite is 1.18 x $10^9$ Pa.

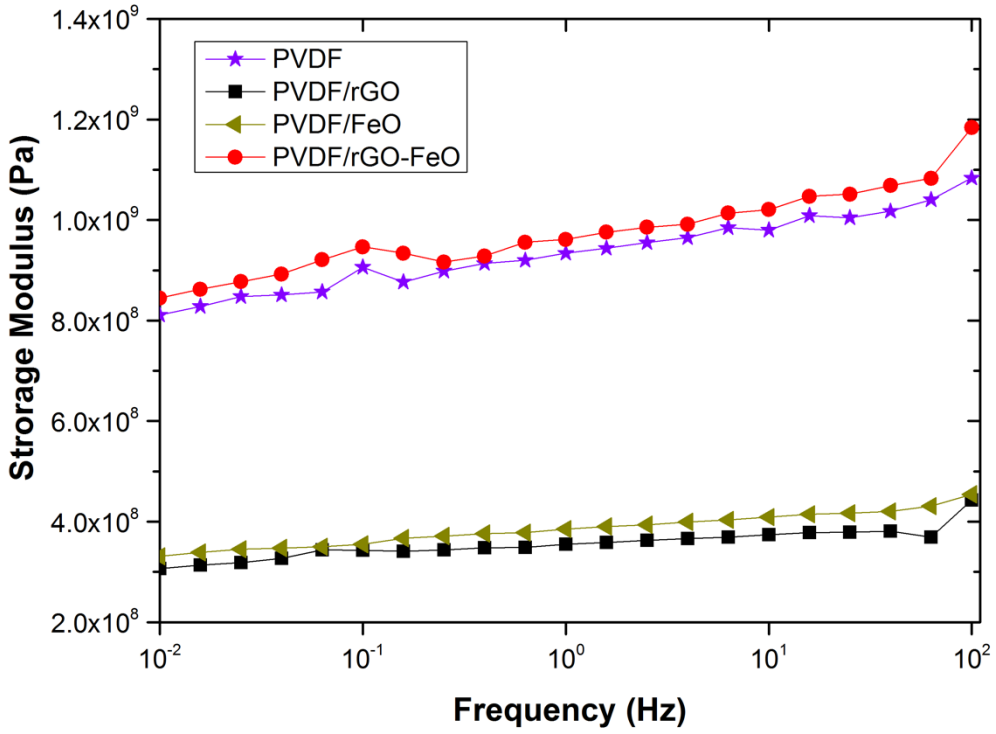


Figure 4. 22. Variation in storage modulus with frequency for PVDF, PVDF/rGO, PVDF/FeO, PVDF/rGO-FeO.

### 4.2.3. Thermal Properties

#### 4.2.3.1. Differential Scanning Calorimetry

The DSC analysis of the samples were done by measuring the melting and crystallization behavior of the samples. The first cooling and second heating were recorded and the results

are illustrated in Figure 4.23 and Table 4.7. The degree of crystallinity ($X_C$ ) of the polymer was calculated using Equation (4.2).

Table 4. 7. DSC data of PVDF/rGO-FeO, PVDF/rGO, PVDF/FeO, and PVDF.

| **Sample** | **Crystallization Temperature (°C)** | **Melting Temperature (°C)** | **$\Delta H_m$ (J/g)** | **Degree of Crystallinity ($X_c$)** |
|---|---|---|---|---|
| PVDF | 137.16 | 167.42 | 42.76 | 40.72 |
| PVDF/rGO | 140.91 | 169.19 | 43.66 | 41.58 |
| PVDF/FeO | 141 | 169.37 | 42.14 | 40.13 |
| PVDF/rGO-FeO | 140 | 168.75 | 41.35 | 39.38 |

Figure 4.23a indicates the melting curves of PVDF and its composites. The two shoulders observed in the PVDF curve indicates the presence of two types of crystallites [124] with two different lamellae thicknesses [125]. with the addition of the fillers, the melting point is approximately constant which indicates that the lamellae thicknesses was not affected by the fillers. The same is seen for the degree of crystallinity.

The cooling curves of composites in Figure 4.23b shows a shift towards higher temperature. With the addition of nanofillers, the crystallization temperature increased by 4 °C for both PVDF/rGO and PVDF/FeO. Whereas the hybrid additives increased the crystallization temperature by 3 °C.

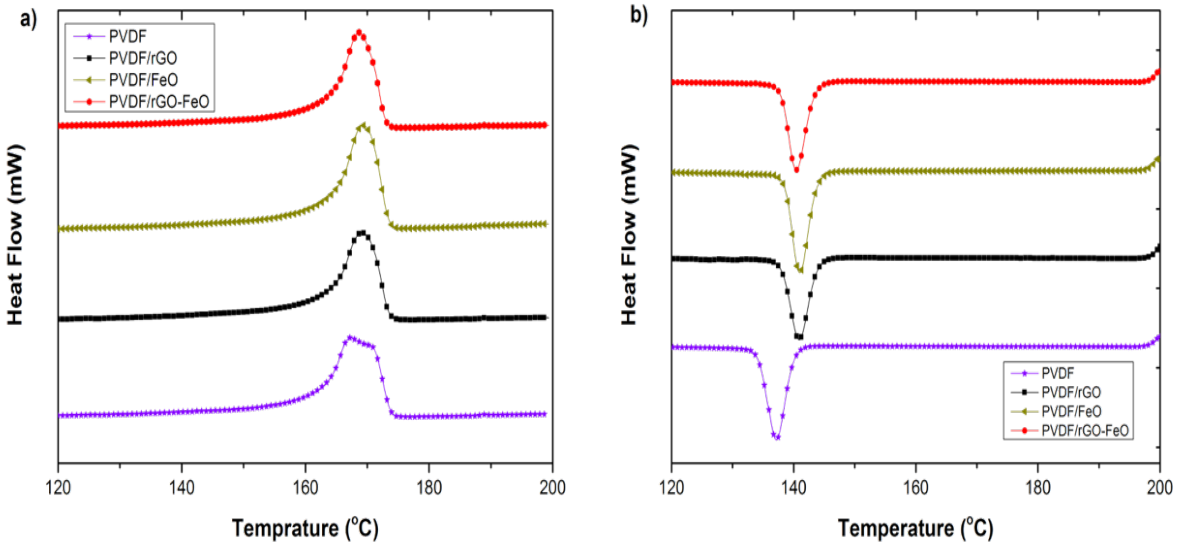


Figure 4. 23. DSC analysis for PVDF/rGO-FeO nanocomposite (a) Melting curve (b) Crystallization curve.

### 4.2.4. Dielectric Properties

Figure 4.24 shows the frequency ($f$) dependence of the dielectric permittivity ($\varepsilon'$) and dielectric loss ($\varepsilon''$) of PVDF, PVDF-rGO, PVDF/FeO and PVDF/rGO-FeO composites. Results show that PVDF/rGO and PVDF/FeO composites have lower $\varepsilon'$ values compared to neat PVDF. This can be explained due to the agglomeration of individual fillers as confirmed by TEM. This agglomeration caused trapping charges at the interfaces due to the Maxwell–Wagner–Sillars (MWS) interfacial polarization effect, as explained in part 4.1.4. PVDF/rGO-FeO hybrid exhibits higher $\varepsilon'$ due to good dispersion of rGO and FeO within the PVDF matrix. The dielectric constant of the hybrid composite at 100 Hz is 2 times higher than that of the unfilled PVDF. Figure 4.24b shows variation of the dielectric loss with frequency of PVDF, PVDF-rGO, PVDF/FeO and PVDF/rGO-FeO composites. $\varepsilon''$ values for all samples

are much lower than their $\varepsilon'$. This result emphasizes the potential of the PVDF/rGO-FeO composites to be used as supercapacitors, as discussed in section 4.1.4.

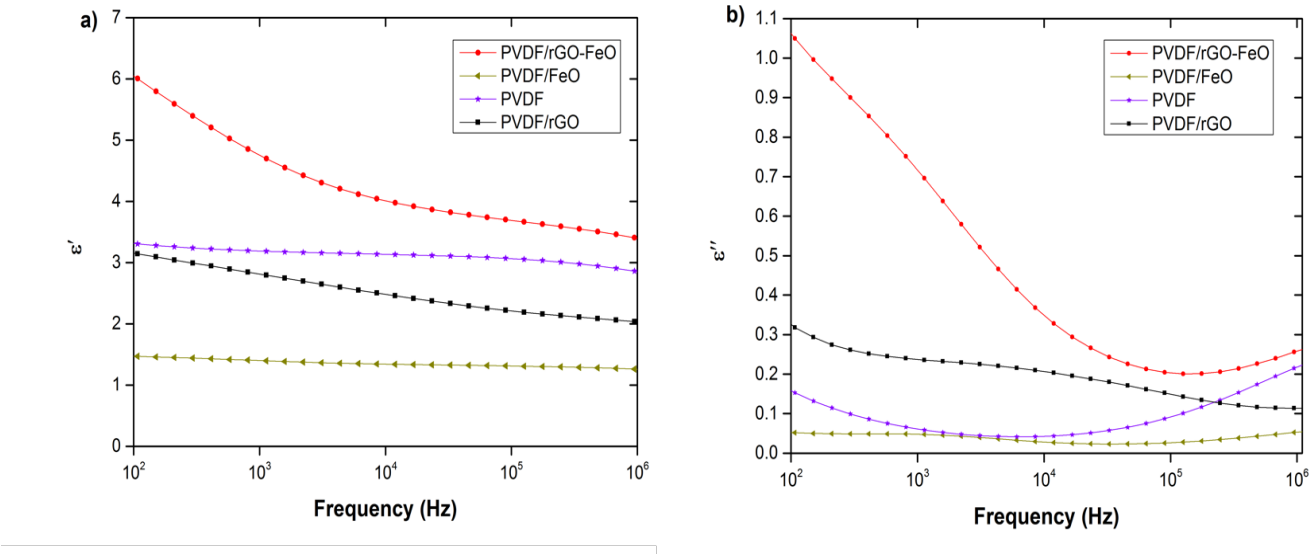


Figure 4. 24. Dielectric permittivity storage (a), and loss (b) of PVDF and its rGO/FeO filled composite samples.

### 4.2.5. Pressure Sensing Behavior

The relative resistance variation of flexible PVDF/rGO, PVDF/FeO and PVDF/rGO-FeO composites for the first four cycles of testing are illustrated in figure 4.25. PVDF/rGO-FeO has the highest relative resistance compared to other composites for all the three applied pressures (5 kPa, 10.7 kPa and 17.6 kPa). The behavior was similar for all the samples and all the applied pressures. The reason is the formation of more conducting filler networks upon compressive forces as discussed in the section 4.2.5.

The largest improvement in the relative resistance variation for the hybrid composite can be

attributed to the less agglomeration in the matrix and better dispersion. Under 5 kPa pressure (Figure 4.25a), the sensitivity of PVDF/rGO-FeO hybrid composite increased by 36.4% compared to PVDF/FeO and 82.8% compared to PVDF/rGO. Whereas at 10.7 kPa pressure, the sensitivity of the hybrid composite increased by 25.5% compared to PVDF/FeO and 84% compared to PVDF/rGO as shown in Figure 4.27b. With a pressure of 17.6 kPa, the sensitivity of the hybrid composite increased by 31% compared to PVDF/FeO and 137.5% compared to PVDF/rGO as shown in Figure 4.25c.

The resistance variation for the PVDF/FeO and PVDF/rGO have a little enhancement. This can be due to the high concentration of the filler networks and the percolation threshold (5 wt.%). In the hybrid case, the fillers are in lower concentration (2.5 wt.% each) ensuring the good filler-filler interaction, well distribution in the polymer medium and good conducting networks. This is the reason for its enhanced pressure sensing behavior.

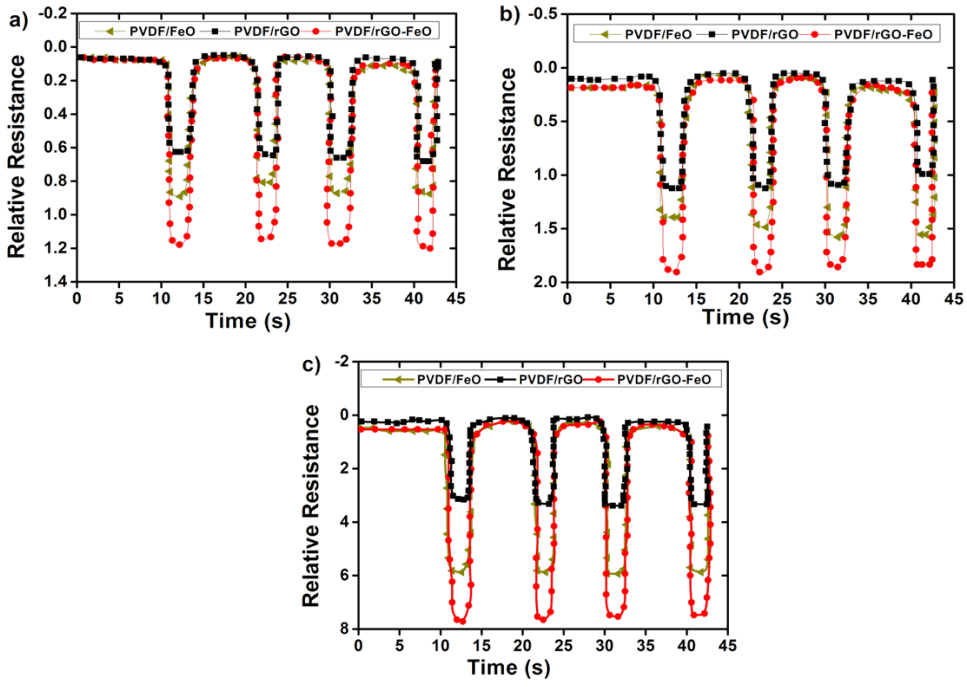


Figure 4. 25. Pressure sensing responses of PVDF/rGO-FeO nanocomposite with different pressures (a) 5 kPa (b) 10.7 kPa (c) 17.6 kPa

### 4.2.6. Vapor Sensing Behavior

Gas sensors are widely used in different places such as transportation, chemical industries, and energy sources [139]. These electro conductive composite sensors can be prepared by adding a conductive additive into matrix. Luo et al. fabricated a vapor detector by addition of CNT into PVDF polymer and it showed good response to acetone [140]. They found that the vapor reacts and interact with non-crystalline regions and do not interact with crystalline region in the film. The change in the structure and aggregation in non-crystalline region altered the interaction between polymer and solvent leading to change in polymer swelling and affected vapor response.

The relative resistance changes for the PVDF/rGO, PVDF/FeO and PVDF/rGO-FeO towards different vapors of organic volatile liquids, acetone, THF and DMF are shown in Figure 4.26. It has less detecting sensitivity towards the non-polar solvent vapors: toluene, xylene and benzene. This propose towards the applicability of metal oxide-graphene hybrid polymer composite in manufacturing electronic noses (e-nose) as already mentioned in section 4.1.6. For acetone, the relative resistance of the hybrid composite is higher by 100 % than PVDF/rGO, and higher by 18.3 % than PVDF/FeO. For THF, the relative resistance of the hybrid composite is higher by 187.8 % than PVDF/rGO, and higher by 23.3 % than PVDF/FeO. For DMF, the relative resistance of the hybrid composite is higher by 168.7% than the PVDF/rGO individual composite, and higher by 32.3% than PVDF/FeO. This shows the effectiveness of the synergistic PVDF-metal oxide-graphene composite in regulating the resistance variation when exposed to solvent vapors. On exposure, the solvent vapors penetrate the polymer medium, allowing it to swell and this can induce the separation of conducting particles, by increasing the distance between them. This loose conducting network is the reason for the increase in relative resistance.

The relative resistance chart provided in Figure 4.27 indicates that PVDF/rGO-FeO hybrid composite has higher relative resistance of 1.2, 1 and 0.82 for THF, DMF and acetone respectively. Whereas the values of relative resistance for Benzene, Toluene and Xylene were 0.3, 0.25 and 0.1 respectively. This can be due to the difference in penetration efficiency for the various solvents since the polar oxygenated solvents contain an oxygen atom that interact and provide easy penetration.

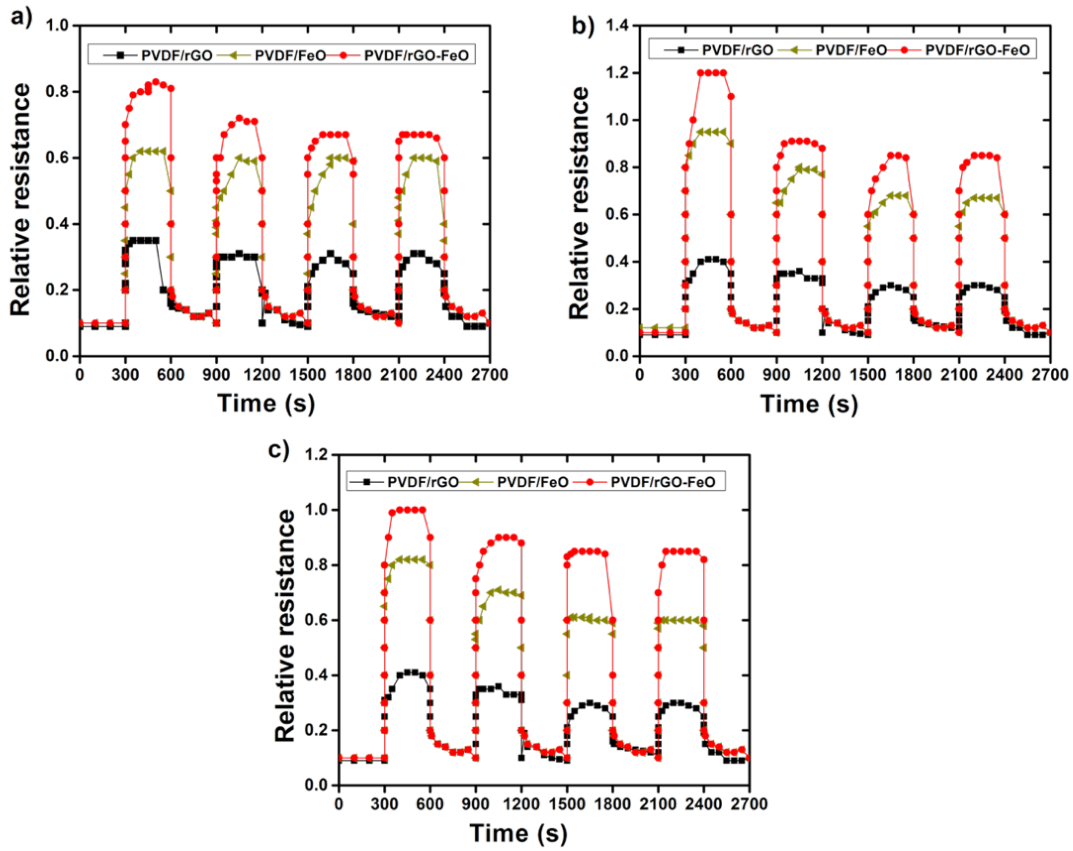


Figure 4. 26. Vapor sensing responses of PVDF/rGO-FeO nanocomposite with different solvent (a) Acetone (b) THF and (c) DMF

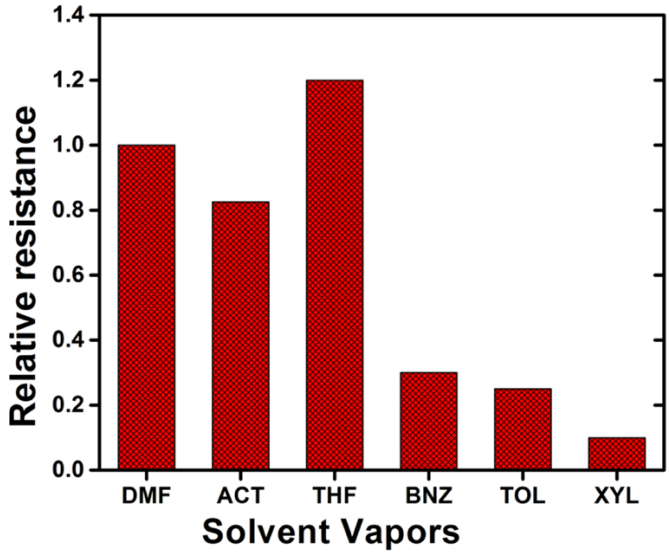


Figure 4. 27. Comparison of different solvents on PVDF/rGO-FeO nanocomposite

## 4.3. Results and Discussion for PVDF/rGO-ZnO Composite System

### 4.3.1. Structure & Morphology

#### 4.3.1.1. Scanning Electron Microscopy

Figure 4.28 shows the SEM cross-sectional images of cryocut samples for the ZnO based PVDF composite system. Figure 4.28a and 4.28b shows PVDF and PVDF/rGO images as discussed in the previous sections. Figure 4.28c represents the PVDF/ZnO, fracture surface with ZnO particles visible in the cross sectional area. Figure 4.30d shows PVDF/rGO-ZnO containing rGO nanolayers and ZnO nanoparticles dispersed within the PVDF matrix.

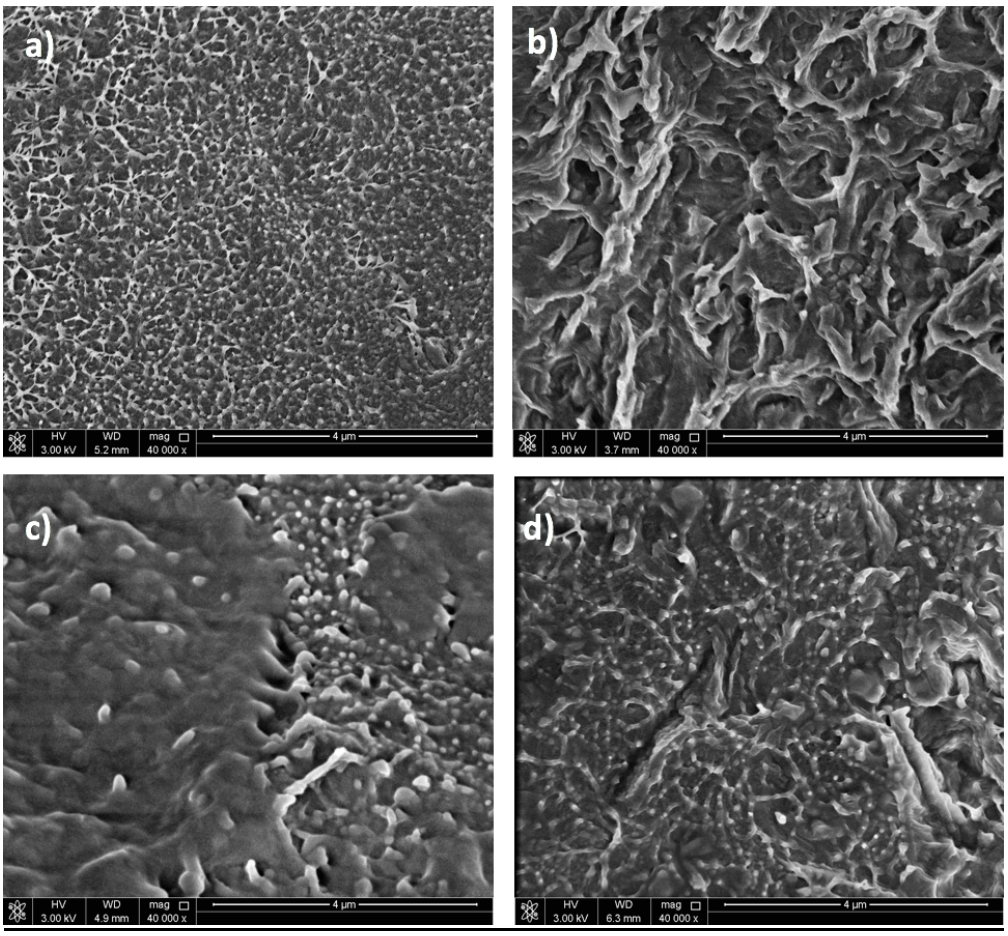


Figure 4. 28. SEM images of a) PVDF b) PVDF/rGO c) PVDF/ZnO and d) PVDF/rGO-ZnO

#### 4.3.1.2. Transmission Electron Microscopy

The TEM images provided in 4.29 confirm the results obtained by the SEM. Neat PVDF shows a plain morphology in the absence of fillers. The nanolayers of rGO and the nanoparticles of ZnO (about 100 nm size) were clearly seen in the images of PVDF/ZnO and PVDF/rGO respectively given in Figure 4.29b and Figure 4.29c. The agglomerated particles are also seen in these two images since the individual filler concentration is 5 wt.%. However, the PVDF/rGO-ZnO shows a well distributed morphology with both nanofillers well separated and well connected uniformly throughout the matrix.

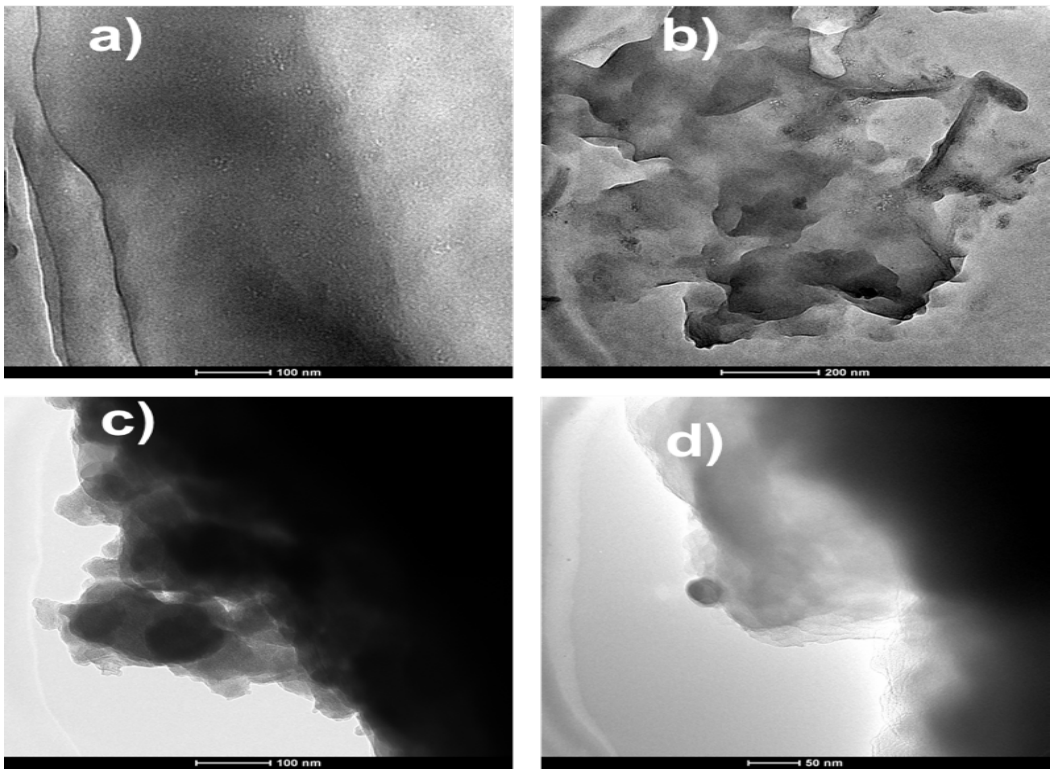


Figure 4. 29.TEM images of surface of a) PVDF b) PVDF/ZnO c) PVDF/rGO and d) PVDF/rGO-ZnO

#### 4.2.1.3. Atomic Force Microscopy

Figure 4.30 shows the surface roughness by means of the 3D AFM images. The average roughness for PVDF was 5.773 nm and became 6.185 nm with the addition of rGO in PVDF/rGO as discussed in the previous sections. It was observed that the roughness value of PVDF/ZnO was 1.944 nm as show in Figure 4.30c. Radwan et al. [141] synthesized PVDF/ZnO composites by electrospinning method and the surface roughness was 40 nm which is higher than the value reported here. But the lower value observed here might be due to the hot pressing method adopted for fabricating the sample film. The roughness for the PVDF/rGO-ZnO hybrid composite was 4.3 nm. This shows a little enhancement in roughness with the addition of rGO layers. Moreover the roughness for the hybrid was lower than the individual PVDF/rGO composite and the neat PVDF, which is a clear indication of well distributed filler particles within the polymer matrix.

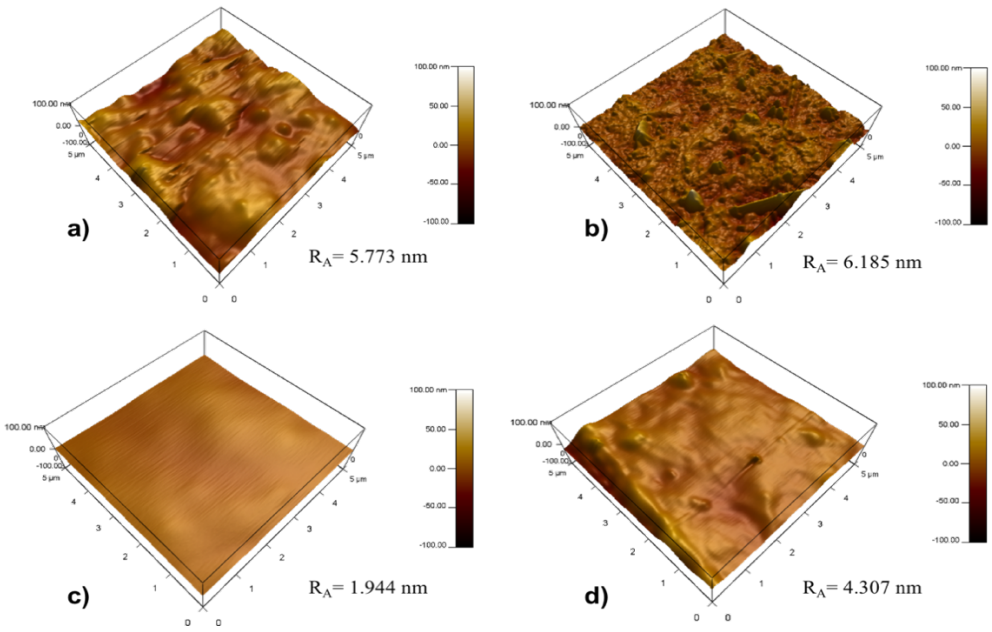


Figure 4. 30. AFM images of surface of a) PVDF b) PVDF/rGO c) PVDF/ZnO and d) PVDF/rGO-ZnO.

#### 4.3.1.4. Fourier Transformation Infrared Spectroscopy

Figure 4.31 shows the FTIR spectra for the neat PVDF, PVDF/rGO, PVDF/ZnO, and PVDF/rGO-ZnO composites. All the peaks observed in Figure 4.31 were explained in section 4.1.1.4. and Equation (4.1) was used to calculate the β crystalline phases within the polymer composite system.

The relative fraction for β phase are 70.37%, 72.73%, 88% and 89% for PVDF, PVDF/rGO, PVDF/ZnO, and PVDF/rGO-ZnO samples respectively. The results indicate that, compared to neat PVDF, the β phase increased with increasing filler particles. For the hybrid PVDF/rGO-ZnO composite, the highest β value is obtained. The improvement in the β phase, is due to the good interaction of the hybrid additives with the fluorine atoms in the polymer backbone. This also point towards the good interaction between the rGO layers and ZnO particles contributing to the synergistic effect of fillers observed in PVDF/rGO-FeO.

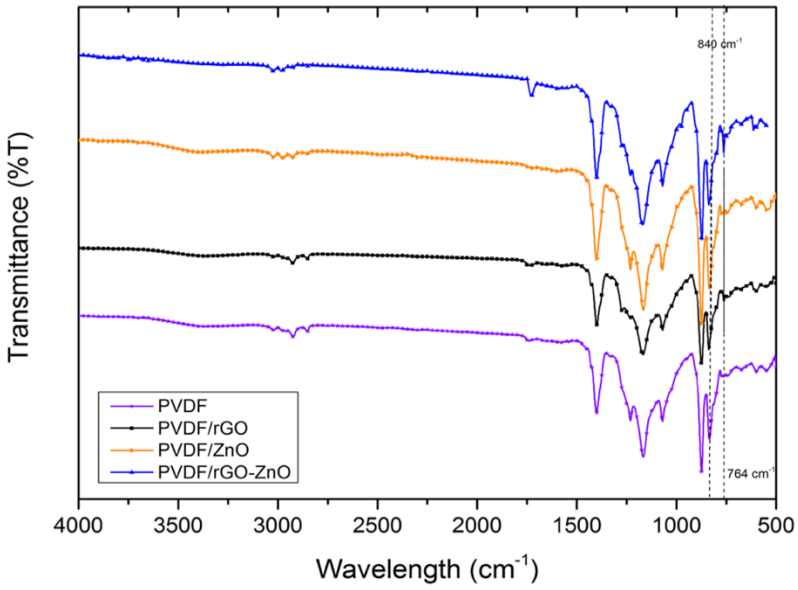


Figure 4. 31. FTIR spectra of PVDF, PVDF/rGO, PVDF/ZnO, and PVDF/rGO-ZnO.

#### 4.3.1.5. X-Ray Diffraction Studies

The XRD spectrum of pure PVDF and its composites PVDF/rGO, PVDF/FeO and PVDF/rGO-FeO are depicted in Figure 4.32. The peaks associated with α phase and β phase are investigated according to the studies done by Eggedi et al. [117]. The area of the α peaks were reduced in the PVDF/rGO-FeO hybrid composite indicating increase of β phase. This substantiates the presence of filler particles causing disturbances in the stacked PVDF layers and thus affecting the crystallinity of the composites.

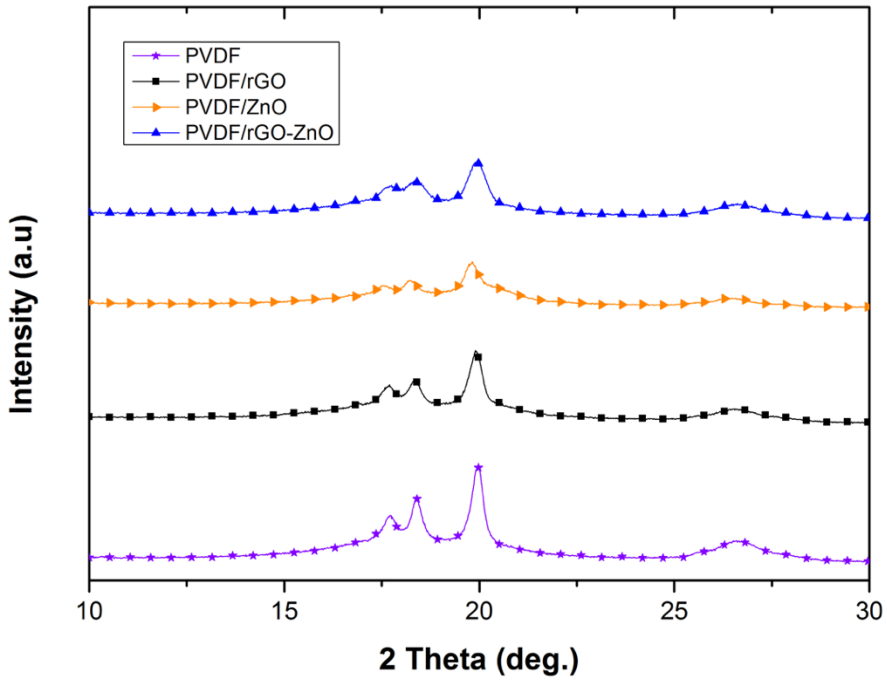


Figure 4. 32. X-ray diffraction pattern of PVDF, PVDF/rGO, PVDF/ZnO, and PVDF/rGO-ZnO

#### 4.3.1.6. Contact Angle Measurements

The surface wettability of PVDF composite was assessed by measuring the water contact angle on various composite surfaces. Table 4.8 shows the angles of water droplet in contact with PVDF, PVDF/rGO, PVDF/ZnO, and PVDF/rGO-ZnO samples. It was observed that the contact angle of PVDF decreased to 95.5° with the addition of rGO and increased to 103° with the addition of ZnO. For the PVDF/ZnO, the contact angle was 155° which was also reported elsewhere [141]. In that case, the method of electrospinning was practiced to fabricate super hydrophobic fibers for coating applications. It was mentioned that the prepared PVDF/ZnO by spray coating shows a contact angle of 122° and this indicated that contact angle changes with the change in the preparation technique. Here, the contact angle observed for PVDF/rGO-ZnO is 110°. This indicate that PVDF/rGO-ZnO is a hydrophobic material that can be used to prevent wettability and it can act as a self-cleaning material as well. The reason behind the hydrophobicity imparted by the hybrid filler combination can be due to the improved filler interaction and thus enhanced filler polymer interfacial stability.

Table 4. 8. Contact Angle Measurements of PVDF/rGO-ZnO

| Samples | Concentration of rGO (wt.%) | Concentration of FeO (wt.%) | Water Contact Angles (°) |
|---|---|---|---|
| PVDF | - | - | 99.7±4.2 |
| PVDF/rGO | 5 | - | 95.5±3.2 |
| PVDF/ZnO | - | 5 | 103±9.8 |
| PVDF/rGO-ZnO | 2.5 | 2.5 | 110±1.37 |

### 4.3.2. Mechanical and Dynamic Mechanical Properties

#### 4.3.2.1. Tensile Test

The obtained values for tensile strength, Young's modulus and elongation at break are shown in Table 4.9.

Table 4. 9. Tensile test results of PVDF, PVDF/rGO, PVDF/ZnO, PVDF/rGO-ZnO

| Samples | Tensile strength (MPa) | Young's Modulus (MPa) | Elongation at Break |
|---|---|---|---|
| PVDF | 21.825±1.93 | 1365.50±101.23 | 16.22±1.45 |
| PVDF-GO | 22.927±1.197 | 2969±380.6 | 7.352±0.66 |
| PVDF-ZnO | 36.546±0.331 | 2778.8±82.2 | 5.5899±0.023 |
| PVDF-GO-ZnO | 43.238±6.36 | 19243±306 | 2.26605±0.075 |

The addition of nanofillers effectively improves the Young's modulus and tensile strength. Tensile strength and Young's modulus for the hybrid PVDF/rGO-ZnO composite was 2 and 14 times respectively higher than the neat PVDF. The reduction of the percentage of elongation at break from 16% for the neat PVDF to 2% for the hybrid composite indicate the brittle behavior of the hybrid composite. The improvement of mechanical properties can be linked with the increase in crystallinity (β phase) as confirmed by FTIR.

Figure 4.33 compares the fractured surfaces after mechanical deformation of the PVDF/rGO, PVDF/ZnO, PVDF/rGO-ZnO composites along with neat PVDF. The neat PVDF has a ductile fracture (Figure 4.33a). Then the ductility decreases with the addition of rGO nanofillers (Figure 4.33b) and ZnO (Figure 4.33c) with less cavities. The flat fracture for the hybrid PVDF/rGO-ZnO indicates decrease in ductility as shown in Figure 4.33d. This can

also be correlated with the well distribution of the filler particles within the matrix and effective stress transfer between the hybrid fillers and PVDF.

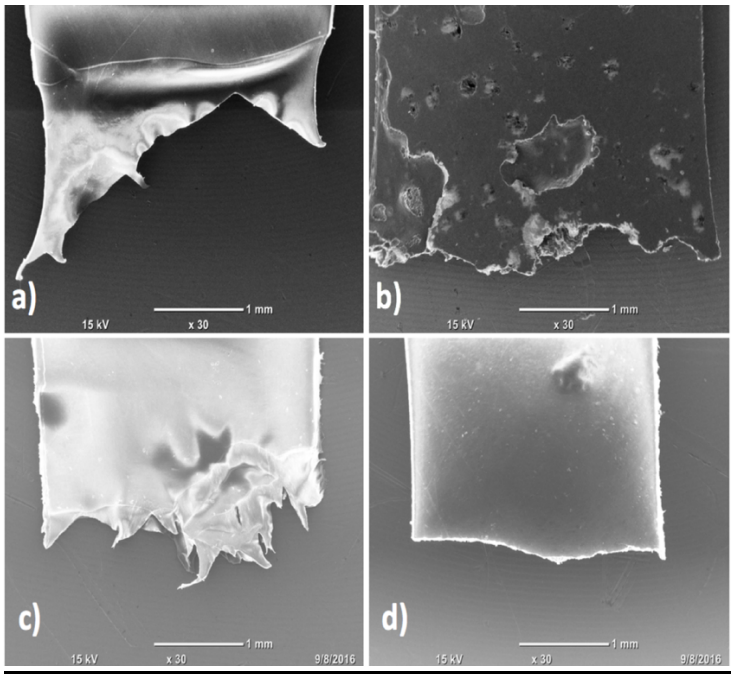


Figure 4. 33. SEM images of surface of tensile test specimen cut a) PVDF b) PVDF/rGO c) PVDF/ZnO and d) PVDF/rGO-ZnO.

#### 4.3.2.2. Dynamic Mechanical Analysis

Figure 4.34 shows the variation in the storage modulus with frequency. The hybrid PVDF/rGO-ZnO composite has higher storage modulus compared to PVDF, and PVDF/rGO, and PVDF/ZnO. The storage modulus of PVDF/rGO-ZnO is 3.2 Pa at 100 Hz. PVDF/rGO have a low storage modulus trend when compared to PVDF, while the other two composites that contain ZnO have higher values. The nature of the filler, as well as its dimensions have a great influence on the flow behavior as well as the storage modulus.

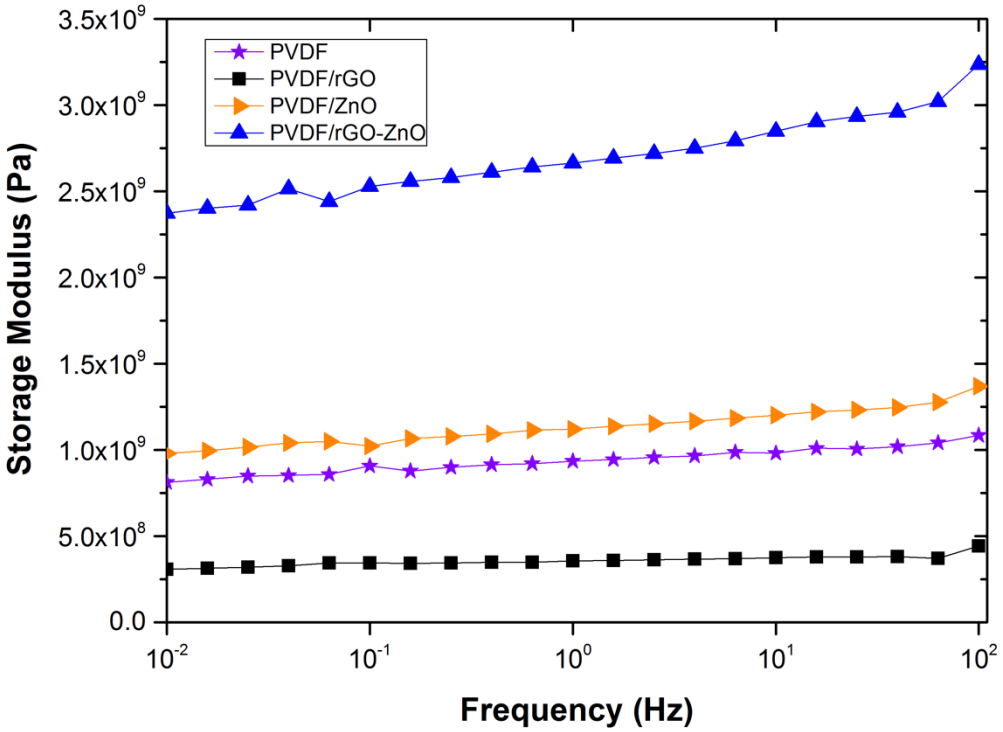


Figure 4. 34. Variation of storage modulus with frequency for PVDF, PVDF/rGO, PVDF/ZnO, PVDF/rGO-ZnO.

### 4.3.3. Thermal Properties

#### 4.3.3.1. Differential Scanning Calorimetry

Table 4. 10 shows the DSC data for the PVDF and its composites, PVDF/rGO, PVDF/ZnO and PVDF/rGO-ZnO composites. The degree of crystallinity ($X_c$) of the polymer was calculated using the mentioned equation (4.2). The crystallinity was found to decrease as we move from the PVDF/rGO to PVDF/rGO-ZnO composites. This is attributed to the well distribution of filler particles in the hybrid composite capable of disturbing the polymer

crystallites, and the effect being higher compared to the individual composites of PVDF/rGO and PVDF/ZnO containing filler agglomerates and clusters.

Table 4. 10. DSC data of PVDF/rGO-ZnO, PVDF/rGO, PVDF/ZnO, and PVDF.

| **Sample** | **Crystallization Temperature ($^{o}$C)** | **Melting Temperature ($^{o}$C)** | **$\Delta H_m$ (J/g)** | **Degree of Crystallinity ($X_c$)** |
|---|---|---|---|---|
| PVDF | 137.16 | 167.42 | 42.76 | 40.72 |
| PVDF/rGO | 140.91 | 169.19 | 43.66 | 41.58 |
| PVDF/ZnO | 139.38 | 168.97 | 41.77 | 39.78 |
| PVDF/rGO-ZnO | 140.11 | 168.25 | 39.04 | 37.18 |

Figure 4.35a shows the melting curves of PVDF and its composites. With the addition of the fillers, the melting point increased and the peaks shifted from 167.4 °C for PVDF to higher temperatures- 169.19 °C for PVDF/rGO, 168.97 °C PVDF/ZnO, and 168.25 °C for PVDF/rGO-ZnO-. The cooling curves of composites in Figure 4.35b also show a shift in the crystallization curve to higher temperature. With the addition of nanofillers, the crystallization temperature increased by 4 °C for PVDF/rGO and by 2 °C with PVDF/ZnO. The hybrid additives increased the crystallization temperature by 3 °C in PVDF/rGO-ZnO.

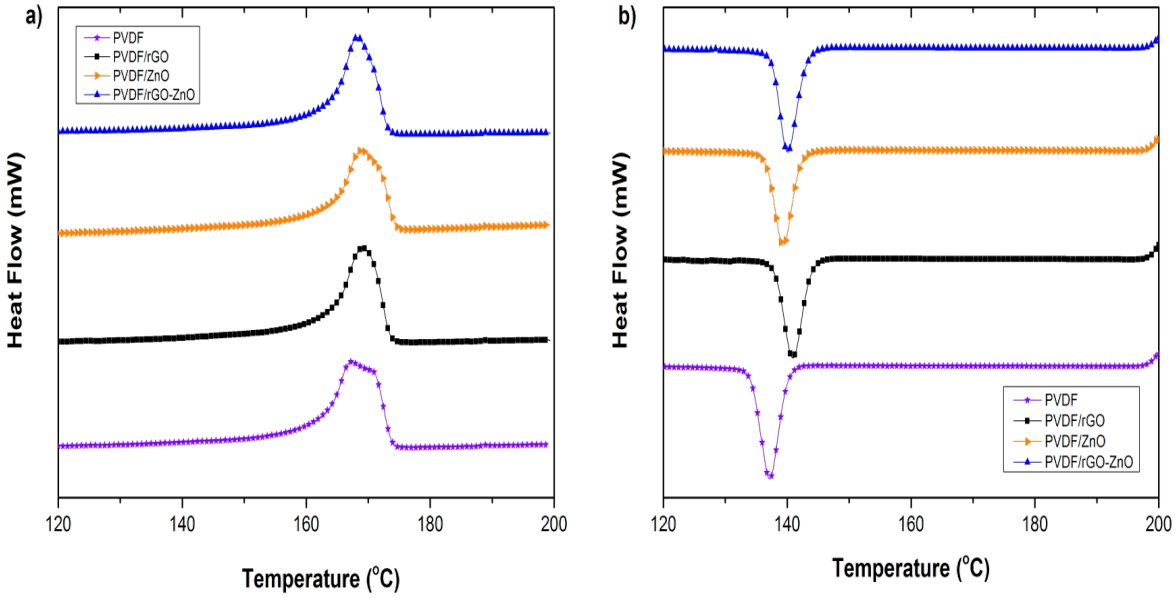


Figure 4. 35. DSC analysis for PVDF/rGO-ZnO nanocomposite (a) Melting curve (b) Crystallization curve.

### 4.3.4. Dielectric Properties

The frequency ($f$) dependence of the dielectric permittivity ($\varepsilon'$) and dielectric loss ($\varepsilon''$) of PVDF, PVDF-rGO, PVDF/ZnO and PVDF/rGO-ZnO are shown in Figure 4.36. Figure 4.36a shows that PVDF/rGO and PVDF/ZnO composites have lower $\varepsilon'$ values compared to neat PVDF. This result again confirms the agglomeration of filler particles as supported by the TEM images. The agglomeration is thought to cause trapped charges at the polymer/filler interfaces due to the MWS interfacial polarization phenomena. Hybrid, PVDF/rGO-ZnO exhibit higher $\varepsilon'$ due to the good dispersion of rGO and ZnO within the PVDF matrix. At 100 Hz the $\varepsilon'$ value reached 6 which is 1.6 times higher than that of the unfilled PVDF. Figure 4.36b shows the variation of dielectric loss with frequency of PVDF, PVDF-rGO,

PVDF/ZnO and PVDF/rGO-ZnO. The range of $\varepsilon''$ values is much lower than $\varepsilon'$, as indicated for other types of fillers used in the previous sections.

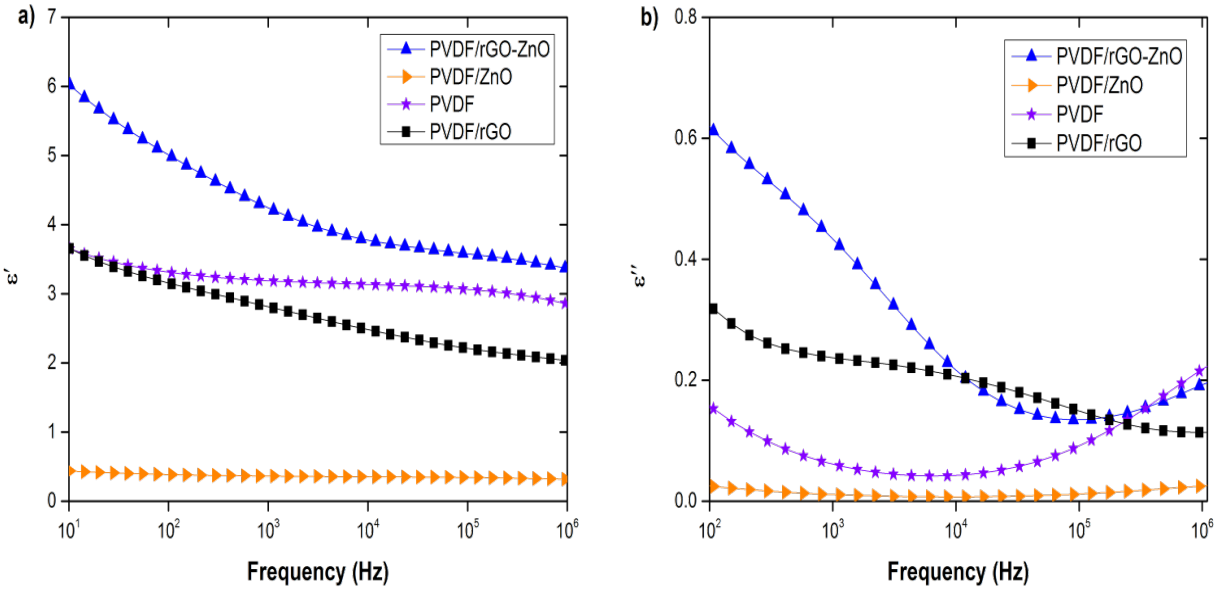


Figure 4. 36. Dielectric permittivity storage (a), and loss (b) of PVDF and its rGO/ZnO filled composite samples.

### 4.3.5. Pressure Sensing Behavior

The relative resistance variation of flexible PVDF/rGO, PVDF/ZnO and PVDF/rGO-ZnO composites, for the first four testing cycles are illustrated in figure 4.37. The hybrid PVDF/rGO-ZnO has the highest relative resistance compared to other composites for all the three applied pressures. For each composite, upon pressure, a decrease in the relative resistance is noticed. This is due to the formation of more filler conducting networks within a particular composite upon a compressive force. The largest improvement observed for the

hybrid composite can be attributed to the less agglomeration in the matrix and better dispersion.

Under a pressure of 5 kPa, the sensitivity of hybrid PVDF/rGO-ZnO composite increased by 172% compared to PVDF/ZnO and 40.6% compared to PVDF/rGO as shown in Figure 4.37a. With pressure 10.7 kPa, the sensitivity of hybrid composite increased by 634.7% compared to PVDF/ZnO and 429% compared to PVDF/rGO as shown in Figure 4.37b. At 17.6 kPa pressure, the sensitivity of hybrid composite increased by 1066% compared to PVDF/ZnO and 228% compared to PVDF/rGO as shown in Figure 4.37c. The relative resistance variation was the highest for the ZnO-graphene hybrid combination with the highest performance. Among the three different metal oxides, ZnO showed the best conductance and stability and this can be the reason for its highest pressure detecting ability.

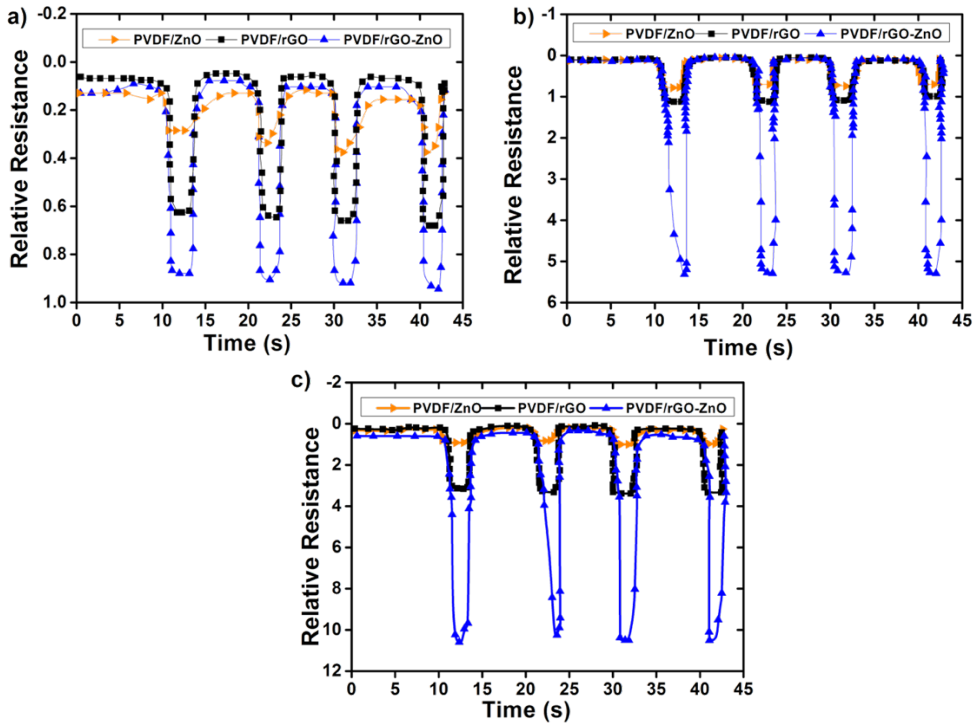


Figure 4. 37. Pressure sensing responses of PVDF/rGO-ZnO nanocomposite with different pressures (a) 5 kPa (b) 10.7 kPa (c) 17.6 kPa.

### 4.3.6. Vapor Sensing Behavior

The relative resistance changes for the various composite samples, PVDF/rGO, PVDF/ZnO and PVDF/rGO-ZnO towards different vapors of organic volatile liquids acetone, THF, and DMF are represented in Figure 4.39. These composites were also checked for their ability to detect polar solvent vapors -Toluene, Xylene and Benzene; however it is found to be less sensitive towards them. This property can be applied in fabricating electronic noses (e-nose) based on these composites to distinguish between polar and non-polar solvent vapors (discussed in section 4.1.6).

In the case of acetone, the relative resistance of the hybrid composite was higher by 116% than PVDF/rGO, and higher by 76% than PVDF/ZnO composites. In the case of THF, the relative resistance of the hybrid composite was higher by 264 % than PVDF/rGO, and higher by 166.6% than PVDF/ZnO. And in the case of DMF, the relative resistance of the hybrid composite was higher by 170% than the PVDF/rGO and higher by 89% than PVDF/ZnO composites.

The relative resistance variation is compared in Figure 4.40 which indicates that PVDF/rGO-ZnO hybrid composite has higher relative resistance of 1.5, 1 and 0.78 towards the vapors of THF, DMF and Acetone respectively. Whereas low values for relative resistance, 0.15, 0.1 and 0.05 were respectively observed for benzene, toluene and xylene vapors. It is also worthy to note that the highest response for the solvent vapors are shown by the ZnO hybrid composite when compared to the TNL and FeO hybrid composites.

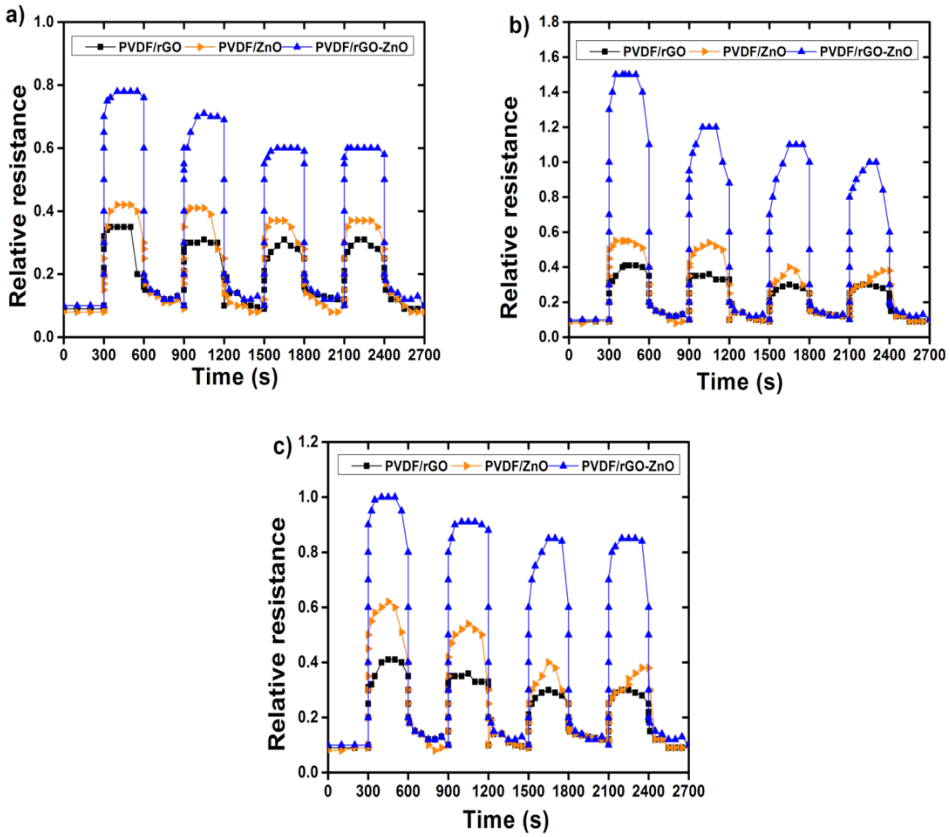


Figure 4. 38. Vapor sensing responses of PVDF/rGO-ZnO nanocomposite with different solvent (a) Acetone (b) THF and (c) DMF

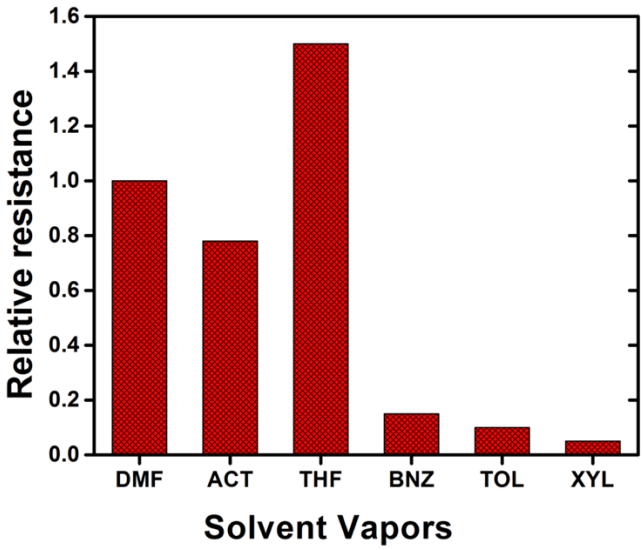


Figure 4. 39. Comparison of different solvents on PVDF/rGO-ZnO nanocomposite

## CONCLUSION

Three different sets of hybrid nanocomposite materials (PVDF/rGO-TNL, PVDF/rGO-FeO and PVDF/rGO-ZnO) were fabricated by solution mixing process. The combination of rGO and metal oxides enhanced the various properties of the composites in addition to reducing the metal oxide content in the final composite. The flexible materials showed excellent sensing performances towards various pressures and solvent vapors with high response in short time. This performance was attributed to the metal oxide conducting network while applying the pressure. Morphology and structural information confirmed the presence of filler aggregates in composites containing individual filler materials at concentration of 5 wt.%. Whereas the hybrid combinations with the same concentration provided better filler distribution and enhanced properties of the materials.

For the first case of hybrid combination of rGO(2.5 wt.%)-TNL(2.5 wt.%), (sample PVDF/rGO-TNL) the enhancement in tensile strength was 115 % whereas for the rGO(2.5 wt.%)-FeO(2.5 wt.%) (sample PVDF/rGO-FeO) and rGO(2.5 wt.%)-ZnO(2.5 wt.%), (sample PVDF/rGO-ZnO) the enhancement was 27.4 and 98 % respectively. When the dielectric properties were compared, PVDF/rGO-TNL showed the maximum dielectric constant of 3.8 at $10^4$ Hz. This was 41% higher than PVDF/rGO-FeO and 52.4% higher than PVDF/rGO-ZnO at $10^4$ Hz. Good mechanical strength and storage modulus values were observed for all hybrid composites which is linked to the presence of β crystalline phase and reduction in α phase. In pressure sensing PVDF/rGO-ZnO showed the best performance with relative resistance change of 38 % higher than that for PVDF/rGO-FeO and 87.5 % higher than PVDF/rGO-TNL at 17.6 kPa.

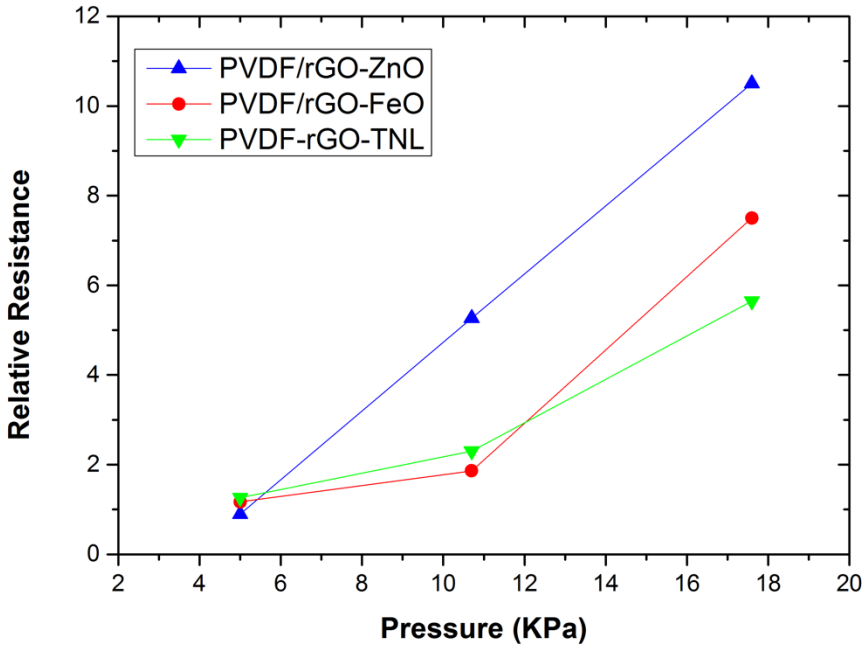


Figure 4. 40. Linear curves of PVDF/rGO-ZnO, PVDF/rGO-FeO and PVDF/rGO-TNL.

Figure 4.38 shows the linear curves of PVDF/rGO-ZnO, PVDF/rGO-FeO and PVDF/rGO-TNL hybrid composite pressure sensors. PVDF/rGO-ZnO shows an ideal sensor behavior compared to other composites. Table 4.11 is used to link between the nanostructure of the composites and their sensing behavior. PVDF/rGO-ZnO has smaller dielectric constant that can lead to more sensitivity. The presence of gas reduces the surface concentration of charges and this lowers the potential barrier and increases the flow of current. Table 4.11 shows that the higher sensitivity is achieved at lower crystallinity percentage. It is well known that the additives can be distributed easily in amorphous region and cannot be accommodated in crystalline region [142]. So the

dispersion will be more homogenous in composite with less crystallinity percentage [143].

Table 4. 11. Summary of relation between sensitivity, degree of crystallinity and dielectric constant of three hybrid composite sensors.

| **PVDF/rGO-ZnO** | | **PVDF/rGO-FeO** | | **PVDF-rGO-TNL** | |
|---|---|---|---|---|---|
| **Pressure (Kpa)** | **Relative Resistance** | **Pressure (Kpa)** | **Relative Resistance** | **Pressure (Kpa)** | **Relative Resistance** |
| 5 | 0.9 | 5 | 1.17 | 5 | 1.26 |
| 10.7 | 5.27 | 10.7 | 1.86 | 10.7 | 2.3 |
| 17.6 | 10.5 | 17.6 | 7.5 | 17.6 | 5.65 |
| **Degree of Crystallinity** | | **Degree of Crystallinity** | | **Degree of Crystallinity** | |
| 37.18 | | 39.38 | | 41.66 | |
| **Dielectric constant(at $10^4$ Hz)** | | **Dielectric constant (at $10^4$ Hz)** | | **Dielectric constant (at $10^4$ Hz)** | |
| 3.7 | | 3.9 | | 5.6 | |

Excellent vapor sensing and ability to distinguish different solvent vapors with different rate of relative resistance change, suggest the application of these hybrid combinations in fabricating electronic noses to detect polar oxygenated solvent vapors. PVDF/rGO-FeO showed the best performance to detect acetone which was 6 % higher than PVDF/rGO-ZnO and higher 14.5 % than PVDF/rGO-TNL. PVDF/rGO-ZnO and PVDF/rGO-FeO showed the same performance to detect (DMF), which was 32 % higher than PVDF/rGO-TNL. The PVDF/rGO-ZnO showed the best performance to detect THF since its relative resistance was 25 % and 70 % higher than that for PVDF/rGO-FeO and PVDF/rGO-TNL respectively. In all the cases, the individual PVDF/rGO and PVDF/metal oxide showed

least improvement in properties. This is because of the agglomeration at the higher filler concentration of 5 wt.%. The good dispersion in the case of synergistic composites, improved the dielectric properties and increased the smoothness and wettability which can reduce the bio-fouling which is highly needed in many sensing applications.

## REFRENCES


[1] M. Tyagi and D. Tyagi, “Polymer Nanocomposites and their Applications in Electronics Industry,” *Int. J. Electron. Electr. Eng.*, vol. 7, no. 6, pp. 603–608, 2014.

[2] Y. Zare and I. Shabani, “Polymer / metal nanocomposites for biomedical applications,” *Mater. Sci. Eng. C*, vol. 60, no. 28, pp. 195–203, 2016.

[3] J. Rhim, H. Park, and C. Ha, “Progress in Polymer Science Bio-nanocomposites for food packaging applications,” *Prog. Polym. Sci.*, vol. 38, no. 10–11, pp. 1629–1652, 2013.

[4] M. Alexandre and P. Dubois, “Polymer-layered silicate nanocomposites : preparation , properties and uses of a new class of materials,” *Mater. Sci. Eng. R Reports*, vol. 28, no. 1–2, pp. 1–63, 2000.

[5] A. Pratheep, D. Depan, N. Singh, and R. Pal, “Nanoscale particles for polymer degradation and stabilization — Trends and future perspectives,” *Prog. Polym. Sci.*, vol. 34, pp. 479–515, 2009.

[6] Y. Y. N. Bonggotgetsakul, R. W. Cattrall, and S. D. Kolev, “Recovery of gold from aqua regia digested electronic scrap using a poly ( vinylidene fl uoride- co - hexa fl uoropropene ) ( PVDF-HFP ) based polymer inclusion membrane ( PIM ) containing Cyphos s IL 104,” *J. Memb. Sci.*, vol. 514, pp. 274–281, 2016.

[7] H. He, Y. Fu, W. Zang, Q. Wang, L. Xing, Y. Zhang, and X. Xue, “A flexible self-powered T-ZnO/PVDF/fabric electronic-skin with multi- functions of tactile-perception, atmosphere-detection and self-clean,” *Nano Energy*, vol. 31, no.

October 2016, pp. 37–48, 2017.

[8] Y. Ting, A. Nugraha, C. Chiu, and H. Gunawan, “Sensors and Actuators A : Physical Design and characterization of one-layer PVDF thin film for a 3D force sensor,” *Sensors Actuators A. Phys.*, vol. 250, pp. 129–137, 2016.

[9] S. Kumar, A. Biswas, S. Sen, C. Das, and K. Henkel, “facile strategy of highly e ffi cient mechanical energy harvester fabrication,” *Nano Energy*, vol. 30, no. August, pp. 621–629, 2016.

[10] L. Huang, C. Lu, F. Wang, and L. Wang, “RSC Advances Preparation of PVDF / graphene ferroelectric composite fi lms by in situ reduction with hydrobromic acids and their properties,” *RSC Adv.*, vol. 4, pp. 45220–45229, 2014.

[11] J. Liang, Y. Xu, D. Sui, L. Zhang, Y. Huang, Y. Ma, F. Li, and Y. Chen, “Flexible , Magnetic , and Electrically Conductive Graphene / Fe3O4 Paper and Its Application for Magnetic-Controlled Switches,” *J. Phys. Chem. C*, pp. 17465–17471, 2010.

[12] Z. Wang, H. Yu, J. Xia, F. Zhang, F. Li, Y. Xia, and Y. Li, “Novel GO-blended PVDF ultra fi ltration membranes,” *Desalination*, vol. 299, pp. 50–54, 2012.

[13] H. M. Ren, Y. H. Ding, F. H. Chang, X. He, J. Q. Feng, C. F. Wang, Y. Jiang, and P. Zhang, “Applied Surface Science Flexible free-standing TiO 2 / graphene / PVdF films as anode materials for lithium-ion batteries,” *Appl. Surf. Sci.*, vol. 263, pp. 54–57, 2012.

[14] D. Emadzadeh, W. J. Lau, T. Matsuura, M. Rahbari-sisakht, and A. F. Ismail, “A novel thin film composite forward osmosis membrane prepared from PSf – TiO 2

nanocomposite substrate for water desalination," *Chem. Eng. J.*, vol. 237, pp. 70–80, 2014.

[15] B. Y. Hu, L. Kienle, Y. Guo, and J. Maier, "High Lithium Electroactivity of Nanometer-Sized Rutile TiO2**," *Adv. Mater.*, pp. 1421–1426, 2006.

[16] J. Yan, H. Song, S. Yang, J. Yan, and X. Chen, "Electrochimica Acta Preparation and electrochemical properties of composites of carbon nanotubes loaded with Ag and TiO 2 nanoparticle for use as anode material in lithium-ion batteries," *Electrochimica*, vol. 53, pp. 6351–6355, 2008.

[17] Y. Duan, L. Pirolli, and A. V Teplyakov, "Sensors and Actuators B : Chemical Investigation of the H 2 S poisoning process for sensing composite material based on carbon nanotubes and metal oxides," *Sensors Actuators B. Chem.*, vol. 235, pp. 213–221, 2016.

[18] B. Wei, M. Hsu, P. Su, H. Lin, R. Wu, and H. Lai, "A novel SnO 2 gas sensor doped with carbon nanotubes operating at room temperature," *Sensors Actuators B Chem.*, vol. 101, no. 2, pp. 81–89, 2004.

[19] F. Mendoza, D. M. Hernández, V. Makarov, E. Febus, B. R. Weiner, and G. Morell, "Sensors and Actuators B : Chemical Room temperature gas sensor based on tin dioxide-carbon nanotubes composite films," *Sensors Actuators B. Chem.*, vol. 190, pp. 227–233, 2014.

[20] M. Castro, B. Kumar, J. F. Feller, Z. Haddi, A. Amari, and B. Bouchikhi, "Sensors and Actuators B : Chemical Novel e-nose for the discrimination of volatile organic biomarkers with an array of carbon nanotubes ( CNT ) conductive polymer

nanocomposites ( CPC ) sensors," *Sensors Actuators B. Chem.*, vol. 159, no. 1, pp. 213–219, 2011.

[21] Y. Luo, X. Wei, D. Cao, R. Bai, F. Xu, and Y. Chen, "ternary conducting polymer nanocomposites based on compatibilizers : Preparation , characterization and vapor sensing applications," *JMADE*, vol. 87, pp. 149–156, 2015.

[22] D. Ponnamma, K. Sadasivuni, M. Strankowski, Q. Guo, and S. Thomas, "Soft Matter reduced graphene oxides in natural rubber for sensing application," pp. 10343–10353, 2013.

[23] A. Ammar, A. M. Al-enizi, M. Alali, and A. Karim, "Influence of graphene oxide on mechanical , morphological , barrier , and electrical properties of polymer membranes," *Arab. J. Chem.*, vol. 9, no. 2, pp. 274–286, 2016.

[24] R. Justin and B. Chen, "Characterisation and drug release performance of biodegradable chitosan – graphene oxide nanocomposites," *Carbohydr. Polym.*, vol. 103, pp. 70–80, 2014.

[25] I. Jeon and J. Baek, "Nanocomposites Derived from Polymers and Inorganic Nanoparticles," *Materials (Basel).*, vol. 3, pp. 3654–3674, 2010.

[26] J. Jordan, K. I. Jacob, R. Tannenbaum, M. A. Sharaf, and I. Jasiuk, "Experimental trends in polymer nanocomposites — a review," *Mater. Sci. Eng. A*, vol. 393, pp. 1–11, 2005.

[27] M. Bahrami and S. Ranjbarian, "Production of micro- and nano-composite particles by supercritical carbon dioxide," *Supercrit. Fluids*, vol. 40, pp. 263–283, 2007.

[28] C. Lei, M. Qiu, M. Zhi, and K. Friedrich, “Tensile performance improvement of low nanoparticles filled-polypropylene composites,” *Compos. Sci. Technol.*, vol. 62, pp. 1327–1340, 2002.

[29] J. Lin, Y. Chan, and Y. Lan, “Hydrophobic Modification of Layered Clays and Compatibility for Epoxy Nanocomposites,” *Materials (Basel).*, vol. 3, pp. 2588–2605, 2010.

[30] H. D. Rozman, A. R. Rozyanty, L. Musa, G. S. Tay, A. R. Rozyanty, L. Musa, and G. S. T. Ultra-violet, “Ultra-Violet Radiation-Cured Biofiber Composites from Kenaf : The Effect of Montmorillonite on the Flexural and Impact Properties from Kenaf : The Effect of Montmorillonite on the Flexural and Impact Properties,” *J. Wood Chem. Technol. ISSN*, vol. 30, no. 2, pp. 152–163, 2010.

[31] A. B. Inceoglu and U. Yilmazew, “Synthesis and Mechanical Properties of Unsaturated Polyester Based Nanocomposites,” *Polym. Eng. Sci.*, vol. 43, no. 3, 2003.

[32] S. Pavlidou and C. D. Papaspyrides, “review on polymer – layered silicate nanocomposites,” *Prog. Polym. Sci.*, vol. 33, pp. 1119–1198, 2008.

[33] R. J. Sharmila, S. Premkumar, and M. Alagar, “Toughened Polyester Matrices for Advanced Composites,” *J. Appl. Polym. Sci.*, vol. 103, pp. 167–177, 2006.

[34] H. Fischer, “Polymer nanocomposites : from fundamental research to specific applications,” *Mater. Sci. Eng. C*, vol. 23, pp. 763–772, 2003.

[35] S. R. Athreya, “PROCESSING AND CHARACTERIZATION OF CARBON BLACK- FILLED ELECTRICALLY CONDUCTIVE NYLON-12

NANOCOMPOSITES PRODUCED BY SELECTIVE LASER SINTERING," 2010.

[36] S. Kashyap, S. K. Pratihar, and S. K. Behera, "Strong and ductile graphene oxide reinforced PVA nanocomposites," *J. Alloys Compd.*, vol. 684, pp. 254–260, 2016.

[37] P. Pascariu, A. Airinei, M. Grigoras, L. Vacareanu, and F. Iacomi, "Applied Surface Science Metal – polymer nanocomposites based on Ni nanoparticles and polythiophene obtained by electrochemical method," *Appl. Surf. Sci.*, vol. 352, pp. 95–102, 2015.

[38] K. K. Sadasivuni, D. Ponnamma, S. Thomas, and Y. Grohens, "Evolution from graphite to graphene elastomer composites," *Prog. Polym. Sci.*, vol. 39, pp. 749–780, 2014.

[39] Y. Grohens and S. Thomas, "Carbon Nanotubes based Elastomer Composites- An Approach towards Multifunctional Materials approach towards multifunctional materials," *J. Mater. Chem. C*, vol. 2, no. 40, pp. 8446–8485, 2014.

[40] K. K. Sadasivuni, A. Kafy, L. Zhai, and H. Ko, "Transparent and Flexible Cellulose Nanocrystal / Reduced Graphene Oxide Film for Proximity Sensing," *Sensors*, vol. 11, no. 8, pp. 994–1002, 2015.

[41] S. K. Kumar, M. Castro, I. Pillin, J. F. Feller, S. Thomas, and Y. Grohens, "Simple technique for the simultaneous determination of solvent diffusion coefficient in polymer by Quantum Resistive Sensors and FT-IR spectroscopy," *Polym. Adv. Technol.*, no. February 2013, 2013.

[42] C. Hou, T. Huang, H. Wang, H. Yu, Q. Zhang, and Y. Li, "A strong and

stretchable self-healing film with self-activated pressure sensitivity for potential artificial skin applications," *Nature*, vol. 3, no. 3138, pp. 21–25, 2013.

[43] M. S. Wahab, K. W. Dalgarno, and R. F. Cochrane, "Selective laser sintering of polymer nanocomposites," *Solid Free. Fabr. Symp.*, vol. 6, pp. 358–366, 2007.

[44] M. Kung, P. Lin, S. Peng, D. Wu, and W. Wu, "Biomimetic polymer-based Ag nanocomposites as a antimicrobial platform," *Appl. Mater. Today*, vol. 4, pp. 31–39, 2016.

[45] A. Raju, V. Lakshmi, R. K. V. Prataap, V. G. Resmi, T. P. D. Rajan, C. Pavithran, V. S. Prasad, and S. Mohan, "Applied Clay Science Adduct modi fi ed nano-clay mineral dispersed polystyrene nanocomposites as advanced corrosion resistance coatings for aluminum alloys," *Appl. Clay Sci.*, vol. 126, pp. 81–88, 2016.

[46] P. Klonos, A. Kyritsis, L. Bokobza, V. M. Gun, and P. Pissis, "Interfacial effects in PDMS/titania nanocomposites studied by thermal and dielectric techniques," *Colloids Surfaces A Physicochem. Eng. Asp.*, 2016.

[47] K. J. Shah, A. D. Shukla, D. O. Shah, and T. Imae, "Effect of organic modi fi ers on dispersion of organoclay in polymer nanocomposites to improve mechanical properties," *Polymer (Guildf).*, vol. 97, pp. 525–532, 2016.

[48] N. B. of C. & Engineer, *The Complete Technology Book on Industrial Polymers, Additives, Colourants and Fillers*. Asia Pacific Business Press Inc, 2006.

[49] O. Hiroji, "Electromechanical properties of polarized polyvinylidene fluoride films as studied by the piezoelectric resonance method," *J. Appl. Phys.*, vol. 47, no. 3, pp. 949–955, 1976.

[50] Y. Wada, “Piezoelectricity and pyroelectricity of polymers,” *Jpn. J. Appl. Phys.*, vol. 15, pp. 2041–2057, 1976.

[51] J. Zhang, Z. Wang, M. Liu, F. Zhao, and Z. Wu, “In-situ modi fi cation of PVDF membrane during phase-inversion process using carbon nanosphere sol as coagulation bath for enhancing anti-fouling ability,” *J. Memb. Sci.*, vol. 526, pp. 272–280, 2017.

[52] L. Huang, C. Lu, F. Wang, and X. Dong, “Piezoelectric property of PVDF / graphene composite fi lms using 1H , 1H , 2H , 2H-Per fl uorooctyltriethoxysilane as a modifying agent,” *J. Alloys Compd.*, vol. 688, pp. 885–892, 2016.

[53] M. Mahdi, K. Shirvanimoghaddam, and M. Naebe, “PVDF / graphene composite nano fi bers with enhanced piezoelectric performance for development of robust nanogenerators,” *Compos. Sci. Technol.*, vol. 138, pp. 49–56, 2017.

[54] J. Ho, T. Ryu, Y. Lansac, Y. Hee, and B. Hun, “Shear stress-induced enhancement of the piezoelectric properties of PVDF-TrFE thin fi lms,” *Org. Electron.*, vol. 28, pp. 67–72, 2016.

[55] E. Zampetti, A. Bearzotti, and A. Macagnano, “Flexible piezoelectric transducer based on electrospun PVDF nanofibers for sensing applications,” *Procedia Eng.*, vol. 87, pp. 1509–1512, 2014.

[56] Z. H. Liu, C. T. Pan, C. Y. Su, L. W. Lin, Y. J. Chen, and J. S. Tsai, “A flexible sensing device based on a PVDF / MWCNT composite nanofiber array with an interdigital electrode,” *Sensors Actuators A Phys.*, vol. 211, pp. 78–88, 2014.

[57] A. Lund, C. Gustafsson, H. Bertilsson, and R. W. Rychwalski, “Enhancement of b

phase crystals formation with the use of nanofillers in PVDF films and fibres," *Compos. Sci. Technol.*, vol. 71, no. 2, pp. 222–229, 2011.

[58] N. Jaitanong, R. Yimnirun, H. R. Zeng, G. R. Li, Q. R. Yin, and A. Chaipanich, "Piezoelectric properties of cement based / PVDF / PZT composites," *Mater. Lett.*, vol. 130, pp. 146–149, 2014.

[59] Z. Pi, J. Zhang, C. Wen, and Z. Zhang, "Flexible piezoelectric nanogenerator made of poly (vinylidene fluoride-co-tri fl uoroethylene) (PVDF-TrFE) thin film," *Nano Energy*, vol. 7, pp. 33–41, 2014.

[60] X. H. Duan, H. Q. Wang, Z. B. Li, L. K. Zhu, R. Chen, D. Y. Kong, and Z. Zhao, "Sound absorption of a flexible micro-perforated panel absorber based on PVDF piezoelectric film," *Appl. Acoust.*, vol. 88, pp. 84–89, 2015.

[61] L. Huang, C. Lu, F. Wang, and X. Dong, "Piezoelectric property of PVDF / graphene composite fi lms using 1H , 1H , 2H , 2H-Per fluorooctyltriethoxysilane as a modifying agent," *J. Alloys Compd.*, vol. 688, pp. 885–892, 2016.

[62] Y. Kim, Y. Xie, X. Wen, S. Wang, S. Jae, H. Song, and Z. Lin, "Highly porous piezoelectric PVDF membrane as effective lithium ion transfer channels for enhanced self-charging power cell," *Nano Energy*, vol. 14, pp. 77–86, 2015.

[63] L. Kupferberg, "Orientation of crystallites in piezoelectric poly(vinylidene fluoride)," *J. Appl. Phys.*, vol. 64, no. 5, pp. 2316–2323, 1988.

[64] A. Lovinger, "Ferroelectric Polymers," *Science (80-. ).*, vol. 220, no. 4602, pp. 1115–1121, 1983.

[65] R. Kepler, "Ferroelectric polymers," *Adv. Phys.*, vol. 41, no. 1, pp. 1–57, 1991.

[66] C. M. Hess, A. R. Rudolph, and P. J. Reid, “Imaging the E ff ects of Annealing on the Polymorphic Phases of Poly(vinylidene fluoride),” *J. Phys. Chem. B*, vol. 119, pp. 4127–4132, 2015.

[67] H. Chen, S. Han, C. Liu, Z. Luo, H. D. Shieh, R. Hsiao, and B. Yang, “Sensors and Actuators A : Physical Investigation of PVDF-TrFE composite with nanofillers for sensitivity improvement,” *Sensors Actuators A. Phys.*, vol. 245, pp. 135–139, 2016.

[68] P. Martins, A. C. Lopes, and S. Lanceros-mendez, “Progress in Polymer Science Electroactive phases of poly ( vinylidene fluoride ): Determination , processing and applications,” *Prog. Polym. Sci.*, vol. 39, no. 4, pp. 683–706, 2014.

[69] M. El Achaby, F. Z. Arrakhiz, S. Vaudreuil, E. M. Essassi, and A. Qaiss, “Applied Surface Science Piezoelectric NL -polymorph formation and properties enhancement in graphene oxide – PVDF nanocomposite films,” *Appl. Surf. Sci.*, vol. 258, no. 19, pp. 7668–7677, 2012.

[70] Y. Seo, “Enhanced Piezoelectric Properties of Electrospun Poly(vinylidene fl uoride)/Multiwalled Carbon Nanotube Composites Due to High β - Phase Formation in Poly(vinylidene fl uoride),” *J Phys Chem*, vol. 117, no. 22, pp. 11791–11799, 2013.

[71] M. Amin, “METHODS FOR PREPARATION OF NANO-COMPOSITES FOR OUTDOOR INSULATION APPLICATIONS,” *Adv. Mater. Sci.*, vol. 34, pp. 173–184, 2013.

[72] A. Deepak and P. Shankar, “Exploring the properties of lead oxide and tungsten

oxide based graphene mixed nanocomposite films," *Nanosyst. PHYSICS, Chem. Math.*, vol. 7, no. 3, pp. 502–505, 2016.

[73] F. Ç. Cebeci, M. L. Öveçog, D. Ürk, E. Demir, O. Bulut, and D. Çakırog, "Understanding the polymer type and CNT orientation effect on the dynamic mechanical properties of high volume fraction CNT polymer nanocomposites," vol. 155, pp. 255–262, 2016.

[74] B. Jogi, M. Kulkarni, P. . Brahmankar, and D. Rantana, "Some Studies on Mechanical Properties of Epoxy/CTBN/Clay Based Polymer Nanocomposites (PNC)," *Procedia Mater. Sci.*, vol. 5, pp. 787–794, 2014.

[75] A. I. R. F. Academy, A. F. Academy, and S. Republic, "EVALUATION OF STRESS-STRAIN PROPERTIES OF SOME NEW POLYMER-CLAY NANOCOMPOSITES FOR AEROSPACE AND DEFENCE APPLICATIONS," in *INTERNATIONAL CONFERENCE of SCIENTIFIC PAPER AFASES 2014*, 2014, p. 9.

[76] M. S. Chowdary and M. S. R. N. Kumar, "Effect of Nanoclay on the Mechanical properties of Polyester and S-Glass Fiber ( Al )," *Int. J. Adv. Sci. Technol.*, vol. 74, pp. 35–42, 2015.

[77] K. K. Sadasivuni, D. Ponnamma, J. Kim, and S. Thomas, *Graphene-Based Polymer Nanocomposites in Electronics*. Springer International Publishing, 2015.

[78] D. Ponnamma, Q. Guo, I. Krupa, M. A. S. A. Al-maadeed, K. T. Varughese, and K. Kumar, "Graphene and graphitic derivative filled polymer composites as potential sensors," *Phys. Chem. Chem. Phys.*, vol. 17, no. 6, pp. 3954–3981, 2015.

[79] A. K. Chilvery, A. K. Batra, and M. Thomas, “Investigation on characteristics of PVDF / ZnO nanocomposite films for high-k capacitors,” *Phys. Sci. Int. J.*, vol. 4, no. 5, pp. 734–741.

[80] G. N. Kumar, Y. V. M. Reddy, and K. H. Reddy, “Synthesis and characterization of iron oxide nanoparticles reinforced polyester / nanocomposites,” *Int. J. Sci. Res. Publ.*, vol. 5, no. 8, pp. 1–13, 2015.

[81] E. A. M. Shalaby, A. Yu, A. N. Solonin, and A. Lotfy, “Materials Science & Engineering A Preparation and characterization of hybrid A359 /( SiC þ Si 3 N 4 ) composites synthesized by stir / squeeze casting techniques,” *Mater. Sci. Eng. A*, vol. 674, pp. 18–24, 2016.

[82] J. Bae, K. Jung, S. Yoo, S. Chang, and M. Kim, “Design and fabrication of a metal-composite hybrid wheel with a friction damping layer for enhancement of ride comfort,” *Compos. Struct.*, vol. 133, pp. 576–584, 2015.

[83] M. Khawaja, “Synthesis and Fabrication of Graphene / Conducting Polymer / Metal Oxide Nanocomposite Materials for Supercapacitor Applications,” 2015.

[84] A. V. Shirinov and W. K. Schomburg, “Pressure sensor from a PVDF film,” *Sensors Actuators A Phys*, vol. 142, no. 1, pp. 48–55, 2008.

[85] M. S. Jayalakshmy and J. Philip, “Sensors and Actuators A : Physical Pyroelectric figures of merit and associated properties of LiTaO 3 / poly vinylidene difluoride nanocomposites for thermal / infrared sensing,” *Sensors Actuators A Phys*, vol. 206, pp. 121–126, 2014.

[86] R. Block, “Mechanical resonance gas sensors with piezoelectric excitation and

detection using PVDF polymer foils," *Sensors Actuators B Chem.*, vol. 7, no. 1–3, pp. 596–601, 1992.

[87] A. Qureshi, A. Altindal, and A. Mergen, "Electrical and gas sensing properties of Li and Ti codoped NiO / PVDF thin film," *Sensors Actuators B Chem.*, vol. 138, pp. 71–75, 2009.

[88] I. Krupa, M. Prostredný, Š. Zdenko, and J. Kraj, "Electrically conductive composites based on an elastomeric matrix fi lled with expanded graphite as a potential oil sensing material," *Smart Mater. Struct.*, vol. 23, no. 12, 2014.

[89] J. Deng, C. V. S. Reddy, and E. H. Walker, "Dielectric behavior of ( PZT / PVDF ) nanocomposites for temperature sensors," *Am. J. Mater. Sci.*, vol. 5, pp. 55–61, 2015.

[90] G. Gao and R. U. I. Gao, "A PVDF Film Sensor for Material Identification," *Sensors Actuators A Phys*, vol. 23, no. 1–3, pp. 886–889, 1990.

[91] H. Bai and G. Shi, "Gas Sensors Based on Conducting Polymers," *Sensors*, vol. 7, no. 3, pp. 267–307, 2007.

[92] A. A. Issa, M. Al-maadeed, A. S. Luyt, M. Mrlik, and M. K. Hassan, "Investigation of the physico-mechanical properties of electrospun PVDF / cellulose ( nano ) fibers," *J. Appl. Polym. Sci.*, vol. 133, no. 26, pp. 2–13, 2016.

[93] G. Buchberger, P. Bartu, R. Schwödiauer, B. Jakoby, and W. Hilber, "A Flexible Polymer Sensor for Light Point Localization," *Procedia Eng.*, vol. 47, pp. 795–800, 2012.

[94] A. Spanu, L. Pinna, F. Viola, L. Seminara, M. Valle, A. Bon, and P. Cosseddu, "A

high-sensitivity tactile sensor based on piezoelectric polymer PVDF coupled to an ultra-low voltage organic transistor," *Org. Electron.*, vol. 36, pp. 57–60, 2016.

[95] P. Saketi, S. K. Latifi, J. Hirvonen, S. Rajala, A. Vehkaoja, T. Salpavaara, J. Lekkala, and P. Kallio, "Sensors and Actuators A : Physical PVDF microforce sensor for the measurement of Z-directional strength in paper fiber bonds," *Sensors Actuators A. Phys.*, vol. 222, pp. 194–203, 2015.

[96] M. Kuna and D. Bäcker, "A PVDF sensor for the in-situ measurement of stress intensity factors during fatigue crack growth," *Procedia Mater. Sci.*, vol. 3, pp. 473–478, 2014.

[97] K. Shin, J. S. Lee, and J. Jang, "Highly sensitive , wearable and wireless pressure sensor using free-standing ZnO nanoneedle / PVDF hybrid thin fi lm for heart rate monitoring," *Nano Energy*, vol. 22, pp. 95–104, 2016.

[98] D. . Marcano, D. . Kosynkin, J. M. Berlin, A. Sinitskii, Z. Z. Sun, A. Slesarev, L. B. Alemany, W. Lu, and J. M. Tour, "Improved Synthesis of Graphene Oxide," *Acs Nano (2010 Am. Chem. Soc.*, vol. 4, no. 8, pp. 4806–4814, 2010.

[99] Y. Q. Wang, G. Q. Hu, X. F. Duan, H. L. Sun, and Q. K. Xue, "Microstructure and formation mechanism of titanium dioxide nanotubes," *Chem. Phys. Lett.*, vol. 365, no. 5, pp. 427–431, 2002.

[100] J. Goldstein, C. E. Lyman, D. E. Newbury, and D. C. Joy, *Scanning Electron Microscopy and X-Ray Microanalysis*, 3rd ed. New York: Kluwer Academic 1Plenum, 2003.

[101] D. B. Williams and C. B. Carter, *Transmission Electron Microscopy: A textbook*

*for material science*. New York: Springer, 2009.

[102] P. De Gennes, "Wetting: statics and dynamics," *Mod. Phys.*, vol. 57, no. 3, pp. 827–863, 1985.

[103] K. Kabza, J. E. Gestwicki, and J. L. Mcgrath, "Contact Angle Goniometry as a Tool for Surface Tension Measurements of Solids , Using Zisman Plot Method A Physical Chemistry Experiment," *J. Chem. Educ.*, vol. 77, no. 1, pp. 63–65, 2000.

[104] H. Assembly, "Contact Angle Measurements Using a Simplified Experimental Setup," *J. Chem. Educ.*, vol. 87, no. 12, pp. 1403–1407, 2010.

[105] T. Young, "An Essay on the Cohesion of Fluids," *Philos. Trans. R. Soc. London*, vol. 95, pp. 65–87, 1805.

[106] "StandardTest Method for Tensile Properties of Thin Plastic Sheeting," *Am. Soc. Test. Mater.*, pp. 194–202, 1991.

[107] S. Brinker and D. Klatt, "Demonstration of concurrent tensile testing and magnetic resonance elastography," *J. Mech. Behav. Biomed. Mater.*, vol. 63, pp. 232–243, 2016.

[108] K. P. Menard and K. Peter, *DYNAMIC MECHANICAL ANALYSIS A Practical Introduction*. Boca Raton: CRC Press, 1999.

[109] K. Friedrich, *Broadband Dielectric Spectroscopy*. Berlin: Springer, 2003.

[110] S. Havriliak and S. Negami, "A Complex Plane Analysis of or-Dispersions in Some Polymer Systems," . *J. Polym. Sci. Part C Polym. Symp.*, vol. 117, no. 14, pp. 99–117, 1966.

[111] H. Xu, L. Xie, D. Wu, and M. Hakkarainen, "Immobilized Graphene Oxide

Nanosheets as Thin but Strong Nanointerfaces in Biocomposites," *ACS Sustain. Chem. Eng.*, vol. 4, no. 4, pp. 2211–2222, 2016.

[112] J. Dai, K. Xiao, H. Dong, W. Liao, X. Tang, Z. Zhang, and S. Cai, "Preparation of Al 2 O 3 / PU / PVDF composite membrane and performance comparison with PVDF membrane , PU / PVDF blending membrane , and Al 2 O 3 / PVDF hybrid membrane," *Desalin. Water Treat.*, vol. 57, no. 2, pp. 487–494, 2016.

[113] E. M. Vrijenhoek, S. Hong, and M. Elimelech, "Influence of membrane surface properties on initial rate of colloidal fouling of reverse osmosis and nanofiltration membranes," *J. Membr. Sci. 188*, vol. 188, pp. 115–128, 2001.

[114] M. Bambo, R. Moutloali, and R. Krause, "Polymer Nanocomposite of PVDF / Organoclay-Copper Nanoparticles hybrid : Synthesis and Characterization," *Mater. Today Proc.*, vol. 2, no. 7, pp. 3921–3931, 2015.

[115] Z. Ouyang, E. Chen, and T. Wu, "Thermal Stability and Magnetic Properties of Polyvinylidene Fluoride/Magnetite Nanocomposites," *Materials (Basel).*, vol. 8, no. 7, pp. 4553–4564, 2015.

[116] P. S. M. Rajesh, S. Bodkhe, S. Kamle, and V. Verma, "Enhancing Beta-Phase in PVDF through Physicochemical Modification of Cellulose," *Electron. Mater. Lett.*, vol. 10, no. 1, pp. 315–319, 2014.

[117] O. Eggedi, U. Valiyaneerilakkal, M. R. Darla, S. Varghese, O. Eggedi, U. Valiyaneerilakkal, and M. R. Darla, "Nanoindentation and thermal characterization of poly ( vinylidenefluoride )/ MWCNT nanocomposites Nanoindentation and thermal characterization of poly ( vinylidenefluoride )/ MWCNT nanocomposites,"

*AIP Adv.*, vol. 4, no. 4, p. 47102, 2016.

[118] X. Cao, J. Ma, X. Shi, and Z. Ren, "Effect of TiO 2 nanoparticle size on the performance of PVDF membrane," *Appl. Surf. Sci.*, vol. 253, no. 2006, pp. 2003–2010, 2010.

[119] F. L. Huang, Q. Q. Wang, Q. F. Wei, W. D. Gao, H. Y. Shou, and S. D. Jiang, "Dynamic wettability and contact angles of poly (vinylidene fluoride) nanofiber membranes grafted with acrylic acid," *Express Polym. Lett.*, vol. 4, no. 9, pp. 551–558, 2010.

[120] R. Chemistry, "FLEXIBLE OIL SENSORS BASED ON MULTIWALLED CARBON NANOTUBE – FILLED ISOPRENE ELASTOMER COMPOSITES," *Rubber Chem. Technol.*, vol. 89, no. 2, pp. 306–315, 2016.

[121] M. A. Almaadeed, R. Kahraman, P. N. Khanam, and N. Madi, "Date palm wood flour / glass fibre reinforced hybrid composites of recycled polypropylene : Mechanical and thermal properties," *J. Mater.*, vol. 42, pp. 289–294, 2012.

[122] T. R. Dargaville, M. C. Celina, J. M. Elliott, P. M. Chaplya, G. D. Jones, D. M. Mowery, R. A. Assink, R. L. Clough, and J. W. Martin, "Characterization , Performance and Optimization of PVDF as a Piezoelectric Film for Advanced Space Mirror Concepts," *Sandia Rep.*, p. 49, 2005.

[123] J. Theerthagiri, R. A. Senthil, M. H. Buraidah, J. Madhavan, and A. K. Arof, "Effect of tetrabutylammonium iodide content on PVDF-PMMA polymer blend electrolytes for dye-sensitized solar cells," *Ionics (Kiel).*, vol. 21, no. 10, pp. 2889–2896, 2015.

[124] F. Z. Arrakhiz, M. El Achaby, M. Malha, M. O. Bensalah, O. Fassi-fehri, R. Bouhfid, K. Benmoussa, and A. Qaiss, "Mechanical and thermal properties of natural fibers reinforced polymer composites : Doum / low density polyethylene," *J. Mater.*, vol. 43, pp. 200–205, 2013.

[125] M. A. S. A. Al-maadeed, "Change in Structure of Ultrahigh Molecular Weight Polyethylene Due to Irradiation in Air and in Nitrogen," *Int. J. Polym. Anal. Charact.*, no. September, pp. 71–84, 2016.

[126] P. N. Khanam, M. Al, A. Almaadeed, P. N. Khanam, M. Al, and A. Almaadeed, "Processing and characterization of polyethylene- based composites," *Adv Manuf Polym Compos Sci*, vol. 1, no. 2, pp. 63–79, 2015.

[127] J. M. Chalmers and R. J. Meier, *Molecular characterization and analysis of polymers*, 1st ed. Elsevier Science, 2008.

[128] H. M. Ahmed, A. D. Windham, M. M. Al-ejji, N. H. Al-qahtani, M. K. Hassan, K. A. Mauritz, R. K. Buchanan, and J. P. Buchanan, "Preparation and Preliminary Dielectric Characterization of Structured C 60 -Thiol-Ene Polymer Nanocomposites Assembled Using the Thiol-Ene Click Reaction," *Materials (Basel).*, vol. 8, no. 11, pp. 7795–7804, 2015.

[129] H. M. Ahmed, M. K. Hassan, K. A. Mauritz, S. L. Bunkley, R. K. Buchanan, and J. P. Buchanan, "Dielectric Properties of C 60 and Sc 3 N @ C 80 Fullerenol Containing Polyurethane Nanocomposites," *Appl. Polym. Sci.*, vol. 131, no. 15, pp. 1–11, 2014.

[130] R. Gregorio, "Effect of Crystalline Phase , Orientation and Temperature on the

Dielectric Properties of Poly ( Vinylidene Fluoride ) ( PVDF ),” *J Mater Sci*, vol. 34, no. 18, pp. 4489–4500, 1999.

[131] K. Nakagawa and Y. Ishida, “Dielectric Relaxations and Molecular Motions in Poly ( vinylidene Fluoride ) with Crystal Form I1,” *Polym. Phys. Ed.*, vol. 11, no. 8, pp. 1503–1533, 1973.

[132] R. J. Klein, S. Zhang, S. Dou, B. H. Jones, R. H. Colby, and J. Runt, “Modeling electrode polarization in dielectric spectroscopy : Ion mobility and mobile ion concentration of single-ion polymer electrolytes,” *J. Chem. Phys.*, vol. 124, no. 14, pp. 144903–144903, 2006.

[133] M. Doi and S. . EDWARDS, *The Theory of Polymer Dynamics*. New York: Oxford University Press, 1986.

[134] J. Y. Li, S. Ducharme, and S. Ducharme, “Electric energy density of dielectric nanocomposites,” *Appl. Phys. Lett.*, vol. 90, no. 13, pp. 28–31, 2007.

[135] S. Stassi, V. Cauda, G. Canavese, and C. F. Pirri, “Flexible Tactile Sensing Based on Piezoresistive Composites :,” *Sensors*, vol. 14, no. 3, pp. 5296–5332, 2014.

[136] S. M. Kanan, O. M. El-kadri, I. A. Abu-yousef, and M. C. Kanan, “Semiconducting Metal Oxide Based Sensors for Selective Gas Pollutant Detection,” *Sensors*, vol. 9, no. 10, pp. 8158–8196, 2009.

[137] I. Sydoryk, A. Lim, W. Jäger, J. Tulip, and M. T. Parsons, “Detection of benzene and toluene gases using a midinfrared continuous-wave external cavity quantum cascade laser at atmospheric pressure,” *Appl. Opt.*, vol. 49, no. 6, pp. 945–949, 2010.

[138] S. K. Hazra and S. Basu, “Graphene-Oxide Nano Composites for Chemical Sensor Applications,” *J. carbon Res.*, vol. 2, no. 12, pp. 1–18, 2016.

[139] S. Qin, D. Qin, W. T. Ford, D. E. Resasco, and J. E. Herrera, “Polymer Brushes on Single-Walled Carbon Nanotubes by Atom Transfer Radical Polymerization of n-Butyl Methacrylate,” *JACS*, no. 6, pp. 170–176, 2003.

[140] Y. Luo, W. Yu, and F. Xu, “Surface Modification and Vapor-Induced Response of Poly ( Vinylidene Fluoride )/ Carbon Black Composite Conductive Thin Films Surface Modification and Vapor-Induced Response of Poly ( Vinylidene Fluoride )/ Carbon Black Composite Conductive Thin Films,” *Polym. Plast. Technol. engneering*, vol. 50, no. 11, 2011.

[141] A. B. Radwan, A. M. A. Mohamed, A. M. Abdullah, and M. A. Al-maadeed, “Surface & Coatings Technology Corrosion protection of electrospun PVDF – ZnO superhydrophobic coating,” *Surf. Coat. Technol.*, vol. 289, pp. 136–143, 2016.

[142] S. Zekriardehani, M. R. Coleman, and S. Jabarin, “THE ROLE OF ADDITIVES AND FREE VOLUME ON THE GAS BARRIER Shahab Zekriardehani , Saleh A . Jabarin , Maria R . Coleman , Polymer Institute , Department of,” *SPE ANTEC™ Indianap.*, pp. 1552–1555, 2016.

[143] S. G. Rathod, R. F. Bhajantri, and V. Ravindrachary, “Pressure sensitive dielectric properties of TiO 2 doped PVA / CN-Li nanocomposite,” *J. Polym. Res.*, vol. 22, no. 2, 2015.